# Processing, Microstructure, and Thermoelectric Properties of Bi$_2$Te$_3$-based Bulk Materials

Wang Zhilei

July 2016

# Contents

## Chapter 1: Introduction

The energy crisis and its attached environmental pollution have become the urgent issues on a global scope. In 2015, the International Energy Agency (IEA) estimated that total world energy consumption was 13,541 Mtoe, or $5.67 \times 10^{20}$ joules, equal to an average power consumption of 18.0 terawatts [1]. In a report of *world energy consumption in 2015* published by BP company [2], in the face of the impending problems of energy shortage and environmental pollution, the use of new energy sources including renewables, hydroelectricity and nuclear energy sources grow at a fast rate in the last decade (Fig. 1.1). However, the traditional energy sources (*e. g.*, coal, oil and natural gas) still have a huge amount of consumption. In addition, the use of coal has the largest growth, as well as considerable growth of oil and natural gas. That is, nowadays, although the new energy sources have been developed fast, the traditional fossil energy is still the main energy source to sustain the human life.
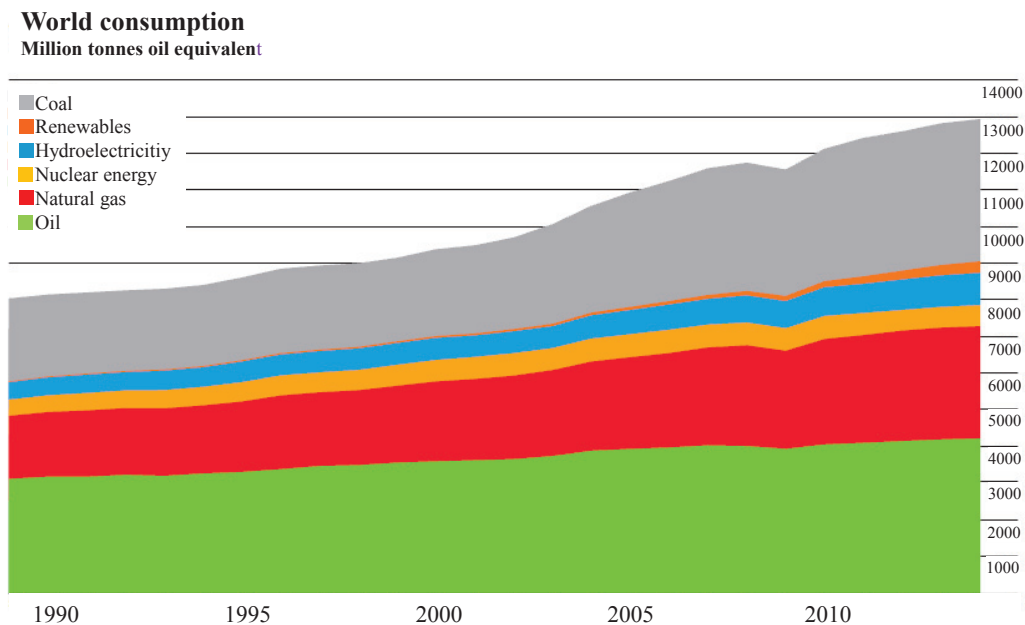


Fig. 1.1 Statistics on world energy consumption in 2015 [2].

From the statistics on utilization of energy for electricity generation by IEA [3], as indicated in Fig. 1.2, coal and natural gas are the major sources occupying more than half of the electricity generation market, even though the current energy efficiency is still in a low level, where most of these energy sources are wasted in the form of heat. As known, these energy sources are non-renewable, and also, the accompanying environmental pollutions cannot be ignored.
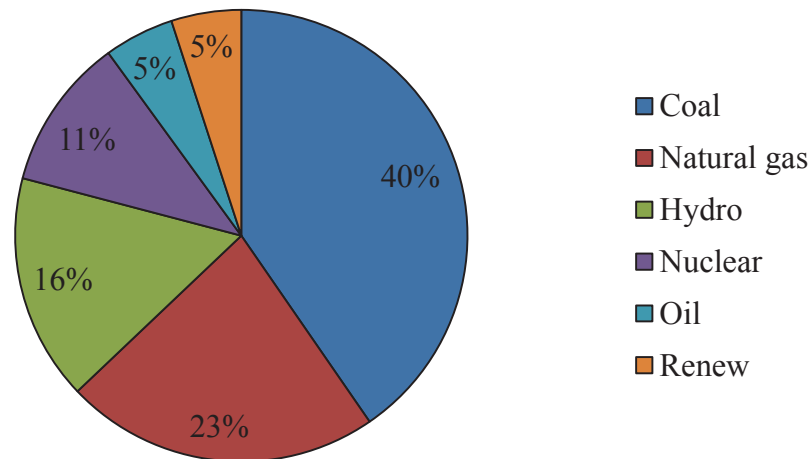


Fig. 1.2 Statistics on utilization of energy for electricity generation by IEA in 2014 [3].

In order to face the energy shortage, meet the increasing energy needs and reduce the attached environmental pollutions, the scientists have made a lot of efforts to find the substitutes of the traditional fossil energy for several decades, such as exploration of new energy, development of renewable energy and cost-efficient technology. Thermoelectric conversion is one of the most promising technologies that can keep in such a task [4-7]. Recently, the Energy Conservation Center, Japan (ECCJ) made an investigation on status of industrial waste heat produced by domestic industries. They found that the waste heat exceeds 1 million TJ in one year. However, 70% of that waste heat is in a low temperature under 200$^{o}$C, as illustrated in Fig. 1.3. Assuming that these low temperature heat sources (≤200$^{o}$C) could be reused, ECCJ makes an energy conversion between heat and electricity using a low efficiency of 6%, where the converted power energy

surprisedly reaches to 1000 MW, which contributes to a reduction of 2.3 million tons $CO_2$ exhaust.
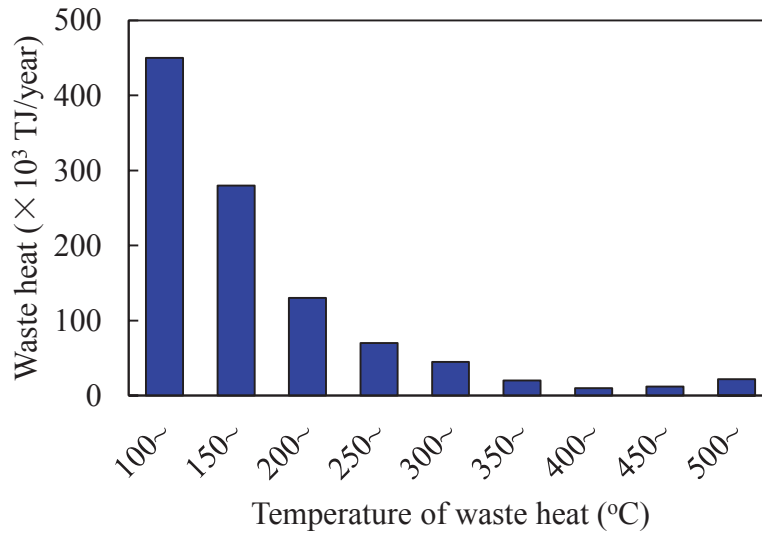


Fig. 1.3 Status of industrial waste heat in Japan reported by ECCJ.

## 1.1 Thermoelectric effects

Thermoelectric effects, as their name suggests, are interactions between heat and electricity. The first report of a thermoelectric effect was in 1821 by Thomas Johann Seebeck. When there is a temperature difference ($\Delta T$) between two ends of a material, a voltage difference develops ($\Delta V$). This effect is called the Seebeck effect, named after the discoverer. The Seebeck effect can be used in a thermoelectric generator, as schematized in Fig. 1.4(a). The voltage difference is proportional to the temperature difference, as shown in the following equation:

$$\Delta V = \alpha \Delta T \tag{1.1}$$

where $\alpha$ is the Seebeck coefficient.

13 years later after the discovery of the Seebeck effect, in 1834, the second thermoelectric effect was noticed by Jean Charles Peltier. When a current is passed through a junction of different conductors, the junction could be cooled. This effect is called Peltier effect, also named after the discoverer. The Peltier effect can be used to create a refrigerator, as schematized in Fig. 1.4(b). The cooling heat flux ($Q$) is proportional to the current ($I$), as shown in the following equation:

3

$$Q = (\Pi_p - \Pi_n)I \tag{1.2}$$

where $\Pi_p$ and $\Pi_n$ are the Peltier coefficients for $p$- and $n$-type thermoelements, respectively, and $I$ is the electric current.

By assuming that the Seebeck and the Peltier effects are reversible thermodynamic processes, in 1851, Lord Kelvin (William Thomson) derived a relationship between these two thermoelectric effects. Then, the third thermoelectric effect, Thomson effect, was discovered, where the current is driven through a temperature gradient causing a reversible heating or cooling. The relationship between the Seebeck and peltier coefficients is described by Eq. 1.3:

$$\Pi = T\alpha \tag{1.3}$$
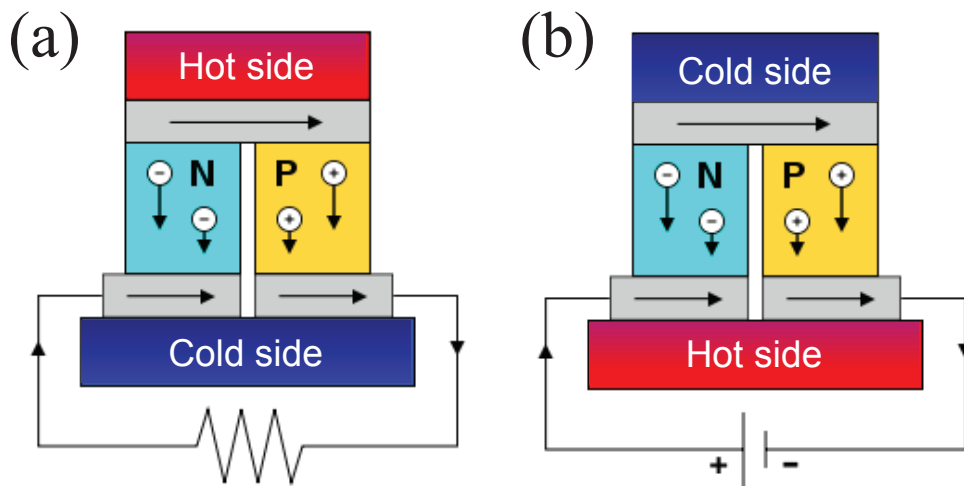


Fig. 1.4 Schematic drawings of (a) a thermoelectric power generation device and (b) a thermoelectric cooling device.

## 1.2 Thermoelectric performance

The comprehensive performance of a thermoelectric device highly depends on a dimensionless thermoelectric figure of merit ($ZT$) of the materials, which can be defined as [8]:

$$ZT = \frac{\alpha^2 T}{\rho \kappa} \tag{1.4}$$

where $\alpha$, $\rho$, $\kappa$, and $T$ are the Seebeck coefficient, electrical resistivity, thermal

conductivity, and absolute temperature, respectively.

In a power generator mode, the maximum efficiency ($\eta_{max}$) of the thermoelectric generator can be calculated as a function of $ZT$ of the thermoelectric materials and the temperatures [9]:

$$\eta_{max} = \frac{T_H - T_C}{T_H} \frac{\sqrt{1 + Z\overline{T}} - 1}{\sqrt{1 + Z\overline{T}} + \frac{T_C}{T_H}} \qquad (1.5)$$

where $T_H$ is the temperature at the hot side, $T_C$ is the temperature at the cold side, and $\overline{T}$ is the average temperature between the hot and cold sides. The first ratio in Eq. 1.5 ($\frac{T_H - T_C}{T_H}$) is the Carnot efficiency [10]. The second ratio is obviously less than 1, hence the higher the $Z\overline{T}$ value of the materials, the closer is the thermoelectric generator efficiency to the Carnot limit.

Similarly, in a thermoelectric refrigerator mode, the maximum efficiency ($\varphi_{max}$) of the thermoelectric refrigerator is calculated by the following function [9]:

$$\varphi_{max} = \frac{T_H}{T_H - T_C} \frac{\sqrt{1 + Z\overline{T}} - \frac{T_C}{T_H}}{\sqrt{1 + Z\overline{T}} + 1} \qquad (1.6)$$

Therefore, the dimensionless figure of merit ($ZT$) is the most useful indicator to evaluate the conversion efficiency of a thermoelectric device. Commercial thermoelectric modules desire materials with a $ZT$ value of $\geq 1$. It should be noted that, commonly, the figure of merit ($ZT$) is assumed to be constant in a limited temperature range in device designs. Actually, the thermoelectric performance of a material highly depends on the temperature. This strong temperature dependence means that it is critical to know the temperature range of the application in order to choose the suitable thermoelectric materials.

## 1.3 Thermoelectric materials

From the time of Seebeck's discovery in 1821 until the beginning of the twentieth century, the thermoelectric applications were not realized extensively due to the extremely low dimensionless figure of merit $ZT$ of the best-known thermoelectric

materials [11]. In the early twentieth century, higher dimensionless figure of merit of some semiconductors was discovered, such as bismuth telluride and zinc antimonide [12]. Since then, many potential thermoelectric materials were discovered sequentially. The current research state of the common thermoelectric materials is shown in Fig. 1.5 [13]. Bismuth telluride and zinc antimonide with $ZT$ values approaching 1 exhibit potentials to use for cooling and power generation in low temperature and middle temperature ranges [13, 14], respectively. Lead telluride as well as silicon-germanium alloys [15, 16] and skutterudites [17, 18] shows good thermoelectric properties in a higher temperature range [19]. There are also many other new high performance thermoelectric materials, such as nanostructured Ag-Pb-Sb-Te (LAST) system materials [20], oxides (*e. g.* $Na_xCoO_2$) [21], and half-Heusler compounds (*e. g.* $Zr_{0.5}Hf_{0.5}NiSn$) [22].
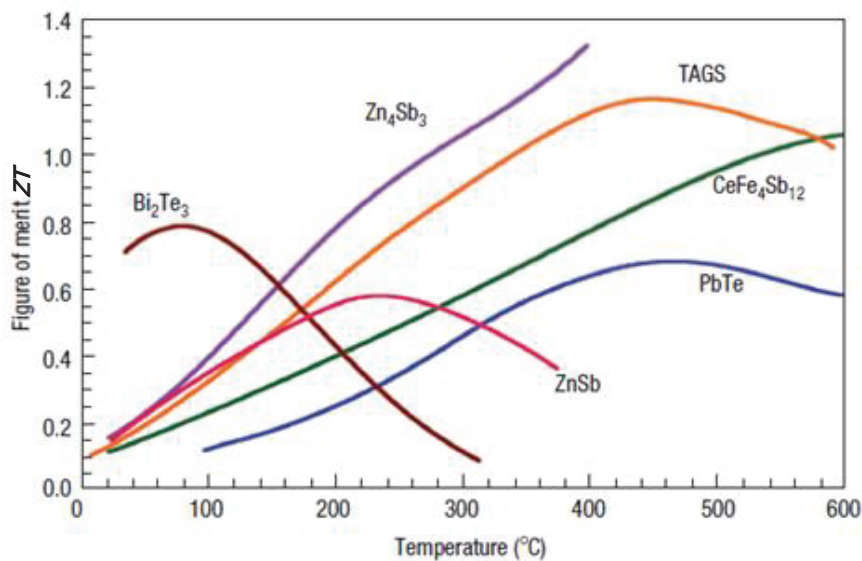


Fig. 1.5 Figure of merit $ZT$ of current thermoelectric materials [13].

As illustrated in Fig. 5, $Bi_2Te_3$ is the most effective thermoelectric materials near room temperature. $Bi_2Te_3$-based compounds have been widely used in various electronic cooling devices such as infrared detectors, microprocessor chips and thermoelectric coolers for laser diodes [23], owing to fast and precise control of temperature and free of noise during the operations. However, the current heat-electricity conversion efficiency of the thermoelectric devices is barely

satisfactory for power generation. Therefore, in the present research, $Bi_2Te_3$-based compounds are the main research objects to aim at promoting their applications for power generation via reusing the huge amount of waste heat.

$Bi_2Te_3$ has a rhombohedral structure with a repeating quintets atom order of -Te(1)-Bi-Te(2)-Bi-Te(1)- along the c-axis, as shown in Fig. 1.6. Due to the existence of van der Waals bond between Te(1)-Te(1) layer [24], this compound has highly anisotropic properties and will cleave easily along the basal planes [25]. Moreover, the thermoelectric properties are better in the directions parallel to the basal plane than to the c-axis [26].
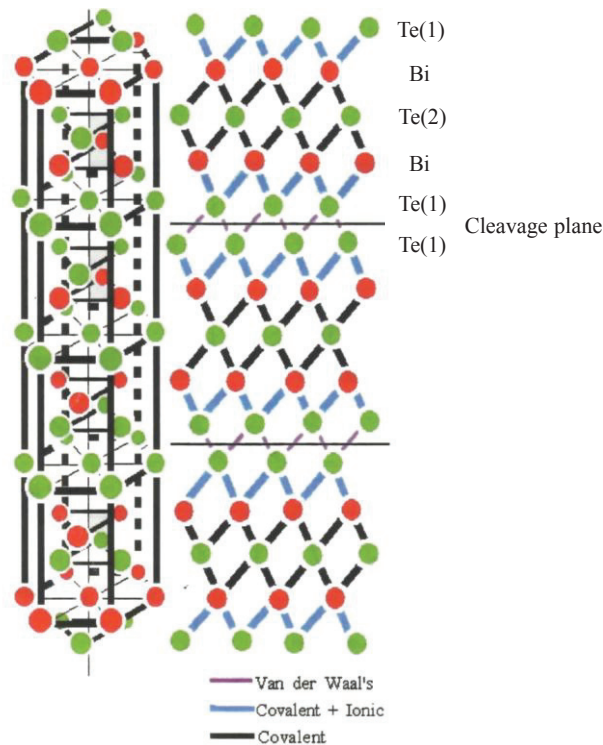


Fig. 1.6 Scheme of $Bi_2Te_3$ compound crystal microstructure.

## 1.4 Current fabrication techniques of $Bi_2Te_3$-based bulk materials

Currently, $Bi_2Te_3$-based alloys are mainly fabricated by unidirectional solidification (e. g., zone melting [27] or the Bridgman method [28]) and powder metallurgy (typically, hot-pressing [29]) techniques. The unidirectionally solidified materials present a high ZT at room temperature, but their mechanical strength is very poor due to large grain sizes and existence of cleavage planes. On the other hand, although hot-pressed materials exhibit high mechanical strength, unfortunately, the

thermoelectric performance is not satisfied. Svechnikova et al. [30] reported $ZT \approx 0.93$ (250-340K) for $n$-type $Bi_2Te_{2.85}Se_{0.15}$ single phase grown by floating-crucible technique, but the ingot was brittle with a bending strength $\sigma_b$ of 43MPa. Fan et al. [31] found $ZT \approx 0.54$ (300K) for $Bi_2Te_{2.85}Se_{0.15}$ sample fabricated by mechanical alloying (MA) and plasma activated sintering (PAS) technique. Yang et al. [29] prepared $Bi_2Te_{2.85}Se_{0.15}$ compound with 0.07wt% $SbI_3$ by bulk mechanical alloying (BMA) and hot-pressing (HP) method, obtaining $ZT \approx 0.48$ at room temperature. In order to improve thermoelectric and mechanical properties simultaneously, a mechanical alloying (MA) and hot-extrusion technique is proposed in this research.

1.4.1 Mechanical alloying

MA is a powder route process, where materials are subjected to severe plastic deformation during collisions between milling medium (milling ball and pot), and thus leading to alloying and reduction in crystallite sizes of powder particles. The processing of intermetallic alloys by mechanical alloying or milling has been studied intensively since the development Ni-based alloys by Benjamin et al [32]. In the same period, thermoelectric alloys were fabricated via ball milling route [33]. So far, MA has been successfully applied to fabricate $Bi_2Te_3$-based single phase. Compared with melting techniques, MA shows lower cost and less processing steps, as well as much more refined crystalline sizes of the MAed powders.

1.4.2 Hot extrusion

Because of the anisotropy of $Bi_2Te_3$-based compounds as mentioned above, hot-extrusion is believed to be a cost-effective and promising way [34-38] to fabricate high performance $Bi_2Te_3$-based bulk materials. Fig. 1.7(a) shows a typical optical micrograph observed on the longitudinal section (parallel to the extrusion direction) of the $Bi_2Te_3$ sample [38]. The microstructure is characterized by fine-equiaxed grains with average grain size <10μm. Fig. 1.7(b) shows the pole figure of (0 0 0 1) basal planes measured on the longitudinal section [38]. Obviously, the basal planes in the extruded sample are preferentially oriented parallel to the extrusion direction.

Therefore, refined microstructure and preferred orientation can be obtained simultaneously for the hot-extruded sample, which is benefit to the improvements in both thermoelectric and mechanical properties.
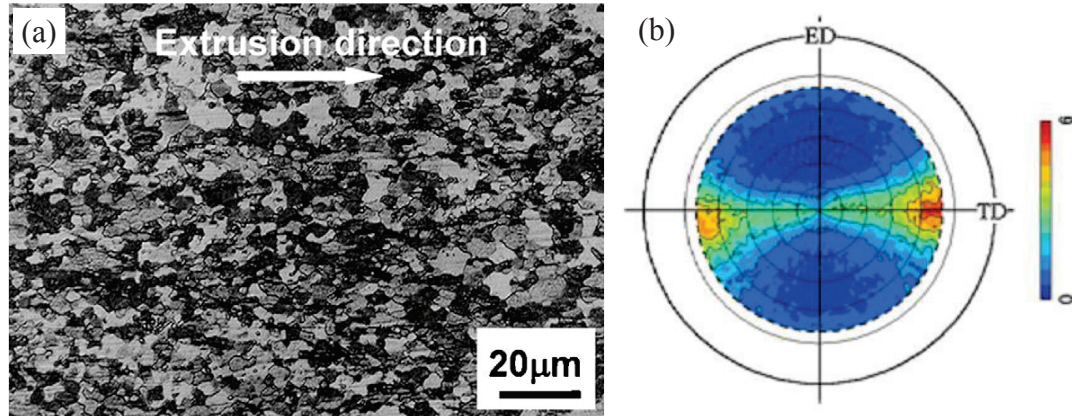


Fig. 1.7 (a) typical optical micrograph and (b) (0 0 0 1) pole figure of the hot-extruded sample on its longitudinal section.

## 1.5 Purpose of present work

From the viewpoints of grain refinement and preferred orientation, the present work is intended to use MA and hot-extrusion technique to fabricate $Bi_2Te_3$-based bulk thermoelectric materials, so as to improve the thermoelectric and mechanical properties simultaneously. The purpose is to understand the relationships among processing conditions, microstructure, texture, thermoelectric and mechanical properties, thus to promote their industrial applications and contribute to improvement of energy shortage and environmental pollution issues.

## 1.6 Outline of this work

This research has focused on the fabrication and performance improvement of $Bi_2Te_3$-based bulk materials. The outline is shown in Fig. 1.8. In Chapter 1, the background of present work was described. Due to the energy crisis and its attached environmental pollution issues, thermoelectric conversion has attracted much attention in the recent decades. In order to enhance the thermoelectric and mechanical properties simultaneously, a combination of MA and hot-extrusion was proposed to

fabricate $Bi_2Te_3$-based bulk materials in this work. The purpose was to understand the relationships among processing conditions, microstructure, texture, thermoelectric and mechanical properties, thus to promote their industrial applications and contribute to improvement of energy shortage and environmental pollution issues. Information of thermoelectric effect, thermoelectric performance, current thermoelectric materials and fabrication methods are also described in Chapter 1.

In Chapters 2 and 3, *p*-type Bi-Te-Sb and *n*-type Bi-Te-Se compounds were successfully fabricated by mechanical alloying (MA) and hot-extrusion technique. The effect of processing conditions on microstructure, texture, thermoelectric and mechanical properties was clarified systematically.

A Te-rich phase was observed in the extruded samples, as described in Chapter 3. Therefore, in Chapter 4, the formation mechanisms of Te-rich phase and its effect on microstructure and thermoelectric properties of hot-extruded $Bi_2Te_3$-based bulk materials were clarified. Effect of excessive Te addition on microstructure and thermoelectric properties was also studied.

In Chapter 5, in order to further improve the thermoelectric performance of $Bi_2Te_{2.85}Se_{0.15}$ hot-extruded samples, doping, as an effective way to enhance thermoelectric properties, was conducted. The effect of Cu-doping on microstructure, thermoelectric and mechanical properties was studied systematically.

In Chapter 6, in order to control the mechanical-deformation defects formed during MA and hot-extrusion processes, and thus to improve thermoelectric properties, heat treatment was carried out for $Bi_{0.4}Sb_{1.6}Te_3$ extruded samples. The effect of annealing on microstructure, thermoelectric and mechanical properties was investigated in detail.

In Chapter 7, a new fabrication method that combined a potential powder preparation method of rapid solidification (RS) and consolidation method of spark plasma sintering (SPS) or hot-extrusion was explored to further improve the thermoelectric performance of $Bi_2Te_3$-based compounds and realize industrial mass production. Processing conditions, microstructure, texture, thermoelectric and mechanical properties of the $Bi_{0.4}Sb_{1.6}Te_3$ samples fabricated from RSed powders

were investigated.

In Chapter 8, some general conclusions of this work were made. In addition, a few schedules to motivate the future research on improvement of the thermoelectric performance of $Bi_2Te_3$-based materials were proposed.
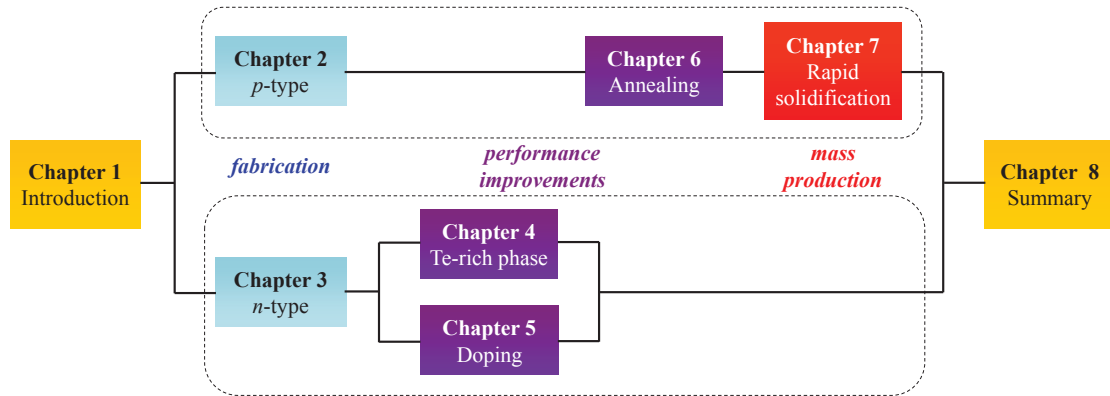
Fig. 1.8 Outline of the present thesis.

**References**

[1] IEA: Key World Energy Statistics 2015. (2015) 837.

[2] BP: Statistical Review of World Energy, Workbook (xlsx), London, 2015

[3] IEA: 2014 Key World Energy Statistics. (2014) 638.

[4] D. M. Rowe, Renew. Energy 16 (1999) 1251.

[5] S. B. Riffat, X. Ma, Appl. Therm. Eng. 23 (2003) 913.

[6] C. J. Vineis, A. Shakouri, A. Majumdar, M. G. Kanatzidis, Adv. Mater. 22 (2010) 3970.

[7] K. Biswas, J. He, I. D. Blum, C. I. Wu, T. P. Hogan, D. N. Seidman, V. P. Dravid, M. G. Kanatzidis, Nature 489 (2012) 414.

[8] Altenkirch, Physikalische Zeitschrift 10 (1909) 560.

[9] H. J. Goldsmid, Applications of Thermoelectricity, Methuen and Co., London, 1960.

[10] Holman, P. Jack, Thermodynamics, New York: McGraw-Hill, (1980) 217.

[11] H. J. Goldsmid, R. W. Douglas, J. Appl. Phys. 5(11) (1954) 386.

[12] M. Telkes, J. Appl. Phys. 18(12) (1947) 1116-1127.

[13] G. J. Snyder, M. Christensen, E. Nishibori, T. Caillat, B. B. Iversen, Nat. Mater. 3(7) (2004) 458-463.

[14] E. S. Toberer, P. Rauwel, S. Gariel, J. Tafto, G. J. Snyder, J. Mater. Chem. 20(44) (2010) 9877-9885.

[15] B. Abeles, D. S. Beers, G. D. Cody, J. P. Dismukes, Phys. Rev. 125(1) (1962) 44-46.

[16] F. D. Rosi, Solid-State Electron. 11(9) (1968) 833-868.

[17] W. Jeitschko, D. Braun, Acta Crystallogr. B33 (1977) 3401.

[18] R. W. Fritts, I. B. Cado, E. Miller, Reinhold Publishing Co., New York, 1960.

[19] B. C. Sales, D. Mandrus, R. K. Williams, Science 272(5266) (1996) 1325-1328.

[20] E. Quarez, K. F. Hsu, R. Pcionek, N. Frangis, E. K. Polychroniadis, M. G. Kanatzidis, J. Am. Ceram. Soc. 127(25) (2005) 9177-9190.

[21] I. Terasaki, Y. Sasago, K. Uchinokura, Phys. Rev. B 56(20) (1997) R12685-R12687.

[22] C. Uher, J. Yang, S. Hu, D. Morelli, G., Phys. Rev. B 59(13) (1999) 8615-8621.

[23] J. T. Im, K. T. Hartwig, J. Sharp, Acta Mater. 52 (2004) 49-55.

[24] J. R. Weise, L. Muller, J. Phys. Chem. Solids 15 (1960) 13.

[25] J. O. Jenkins, J. A. Rayne, R.W. Ure, Phys Rev B 5(1972) 3171.

[26] L. G. Schulz, J. Appl. Phys. 20 (1949) 1030.

[27] P. J. Taylor, J. R. Maddux, W. A. Jesser, F. D. Rosi, J. Appl. Phys. 85 (1999) 7807-7813.

[28] W. M. Yim, F. D. Rosi, Solid-State Electron. 15 (1972) 1121.

[29] J. Y. Yang, T. Aizawa, A. Yamamoto, T. Ohtab, J. Alloys Compd. 312 (2000) 326-330.

[30] T. E. Svechnikova, P. P. Konstantinov, G. T. Alekseeva, Inorg. Mater. 36 (6) (2000) 556-560.

[31] X. A. Fan, J. Y. Yang, W. Zhu, H. S. Yun, R. G. Chen, S. Q. Bao, X. K. Duan, J. Alloys Compd. 420 (2006) 256-259.

[32] J. S. Benjamin, Metall. Trans. 1(1970) 2943.

[33] H. J. Goldsmid, New York, Plenum Press,1964.

[34] J. Seo, K. Park, C. Lee, Mater. Res. Bull. 33 (1998) 553-559.

[35] S. Miura, Y. Sato, K. Fukuda, K. Nishimura, K. Ikeda, Mater. Sci. Eng. A 277 (2000) 244-249.

[36] S. J. Hong, S. H. Lee, B. S. Chun, Mater. Sci. Eng. B 98 (2003) 232-238.

[37] S. J. Hong, B. S. Chun, Mater. Sci. Eng. A 356 (2003) 345-351.

[38] Z. C. Chen, K. Suzuki, S. Miura, K. Nishimura, K. Ikeda, Mater. Sci. Eng., A 500 (2009) 70-78.

# Chapter 2 Fabrication of *p*-type Bi-Sb-Te bulk materials by MA and hot-extrusion technique

## 2.1 Introduction

As mentioned in Chapter 1, the current fabrication methods of $Bi_2Te_3$-based alloys mainly include unidirectional solidification and powder metallurgy techniques. However, it is difficult to obtain high thermoelectric and mechanical performance simultaneously for samples fabricated by the above techniques. In order to improve thermoelectric and mechanical properties simultaneously, MA and hot-extrusion technique is applied to fabricate *p*-type $Bi_{0.4}Sb_{1.6}Te_3$ bulk thermoelectric materials in this chapter.

When the MAed powders are subjected to hot extrusion, it is expected to induce grain refinement and preferred grain orientation and thus to achieve high mechanical and thermoelectric performance because of the anisotropic characteristics of $Bi_2Te_3$-based compounds. Although some research has been conducted on the MA and hot-extrusion process [1–3], it is still necessary to further understand how the processing conditions affect the microstructure and the mechanical and thermoelectric properties of extruded materials. The purpose of this chapter is to fabricate *p*-type $Bi_{0.4}Sb_{1.6}Te_3$ bulk thermoelectric materials by MA and hot-extrusion technique and understand the relationships among processing conditions, extrusion behavior, microstructure, texture, thermoelectric and mechanical properties.

## 2.2 Experimental procedure

### 2.2.1 Starting materials

High purity Bi (99.99%, 63~106 μm), Sb (99.9%, 10 μm), and Te (99.99%, 45μm) powders were used as the starting materials. From the SEM images of the starting powders, as shown in Fig. 2.1, the Bi particle (Fig. 2.1(a)) has irregular shape and larger size. Although the particle sizes of Sb and Te are much smaller than that of Bi, the morphologies of these particles are not homogeneous, where large particles can be observed in the starting powders (Figs. 2.1(b) and (c)).
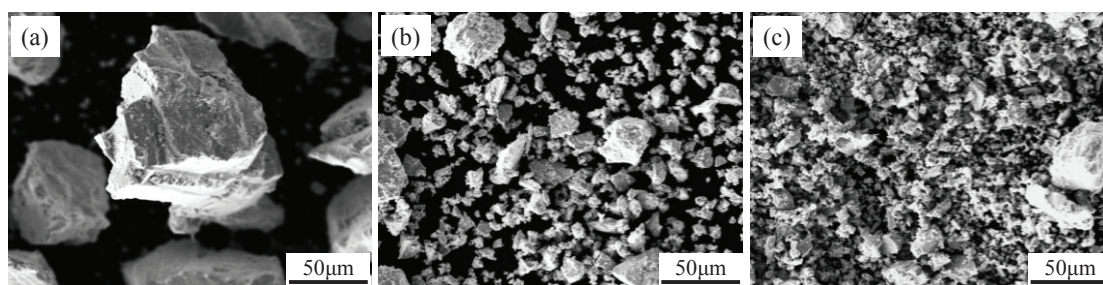
Fig. 2.1 SEM images of (a) Bi, (b) Sb, and (c) Te powders.

## 2.2.2 Preparation of alloy powder by MA

The starting powders with a nominal composition of $Bi_{0.4}Sb_{1.6}Te_3$ were pre-mixed in a mortar and pestle, and then subjected to MA in a planetary ball milling system using an argon-filled $Al_2O_3$ pot and $ZrO_2$ balls ($\Phi$10mm). The MA conditions are listed in Table 2.1.

Table 2.1 MA conditions

| | |
|---|---|
| Ball: powder (weight) | 15:1or 30:1 |
| Rotation speed | 200 rpm |
| Milling time | 0~24 h |
| Atmosphere | Ar |

## 2.2.3 Consolidation by hot extrusion

Firstly, the MAed powders were pressed into a cylindrical green compact at room temperature by uniaxial pressing to obtain a billet used for hot extrusion. The conditions of uniaxial pressing are listed in Table 2.2.

Table 2.2 Conditions of uniaxial pressing

| | |
|---|---|
| Atmosphere | Air |
| Lubricant | Stearic acid |
| Temperature | Room temperature |
| Pressure | 200 MPa |
| Sizes of green compact | $\Phi$30mm×25mm |

Then, the obtained billet was subjected to hot extrusion. The extrusion conditions are listed in Table 2.3, and the schematic drawing of hot-extrusion setup is showed in Fig. 2.2.

Table 2.3 Conditions of hot extrusion

| Extrusion billet | Cold-pressed compact |
| --- | --- |
| Atmosphere | Air |
| Extrusion temperature | 360~450℃ |
| Extrusion ratio | 25 |
| Extrusion speed | 1mm/min |



Fig. 2.2 Schematic drawing of hot extrusion.

2.2.4 Characterization

The density of the extruded samples was determined by the Archimedes method. The density and relative density were calculated by the following equations; respectively.

$$d = \frac{m}{m - m_w} \times d_w \qquad (2.1)$$

$$d_R = \frac{d}{d_T} \times 100 \tag{2.2}$$

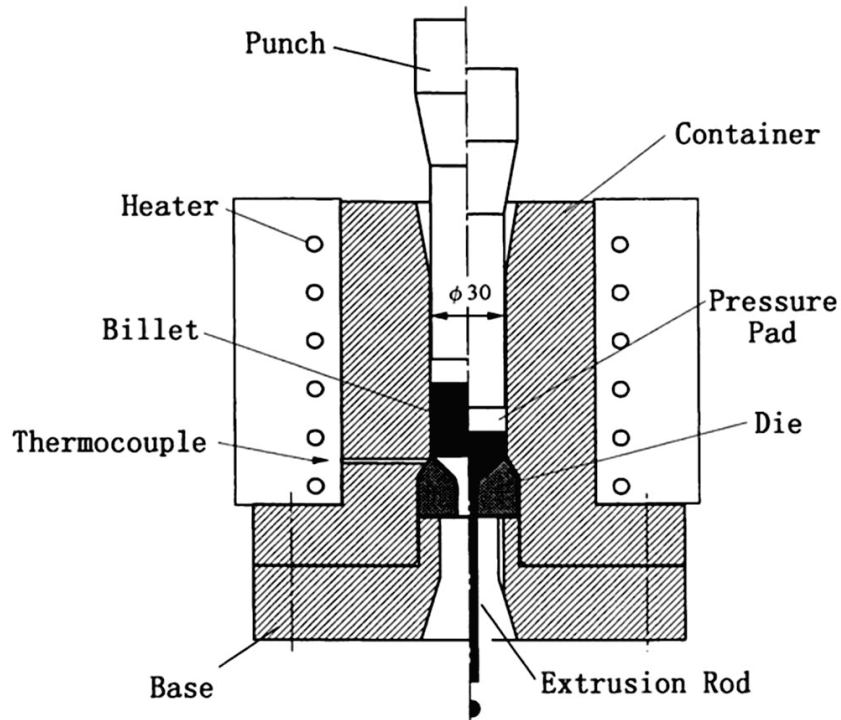where $d$ and $d_w$ are the density of the sample and water, respectively; $m$ and $m_w$ are the weight of sample in air and water, respectively; $d_R$ and $d_T$ are the relative density and theoretical density of the sample, respectively.

Phase identification was performed by X-ray diffraction (XRD) with Cu Kα radiation. The orientation degree was determined using the Lotgering method by the following equations [4]:

$$f = \frac{P - P_0}{1 - P_0} \tag{2.3}$$

$$P_0 = \frac{\sum I_0(00l)}{\sum I_0\,(hkl)} \tag{2.4}$$

$$P = \frac{\sum I(00l)}{\sum I\,(hkl)} \tag{2.5}$$

where $f$ is orientation factor; $P_0$ and $P$ are the ratios of the integrated intensities of all (0 0 l) planes to those of all (h k l) planes for randomly and preferentially oriented samples, respectively.

Microstructural observation was conducted by scanning electron microscopy (SEM). Orientation imaging microscopy (OIM) analysis was performed using an SEM equipped with an electron backscattered diffraction (EBSD) system (JEOL, JSM-7001FA). The OIM maps and pole figures were obtained from analysis of the EBSD data by the software TSL-OIM analysis 6.2.

The Seebeck coefficient ($\alpha$) and electrical resistivity ($\rho$) of the samples were simultaneously measured by static DC method and four-probe method, respectively, using a thermoelectric property test apparatus (ULVAC-RIKO, ZEM-3). The thermal conductivity ($\kappa$) was measured by laser flash method (NETZSCH, LFA457 Micro Flash). In the thermal conductivity measurements, the direction of the heat flux was set to the extrusion direction. The dimensionless figure of merit $ZT$ of the samples was calculated by the equation of $ZT=\alpha^2 T/(\rho\kappa)$.

The mechanical properties at room temperature were evaluated by the Vickers hardness tests at a load of 1.96 N (Shimadzu, HMV-2000).

## 2.3 Results and discussion

2.3.1 Preparation of alloy powders

Fig. 2.3 shows the XRD patterns of the powders prepared by MA with different milling times up to 24 h under a ball-powder weight ratio of 15:1. With increasing milling time, the peaks attributed to the raw powders disappeared and the broadened peaks from $Bi_{0.4}Sb_{1.6}Te_3$ phase grew instead. These broadened peaks are believed to result from small crystallite sizes, lattice strain, crystal lattice imperfections, and chemical inhomogeneity, which are introduced during the MA process. The powder prepared by MA for 24 h can be regarded as a single-phase $Bi_{0.4}Sb_{1.6}Te_3$ solid solution.
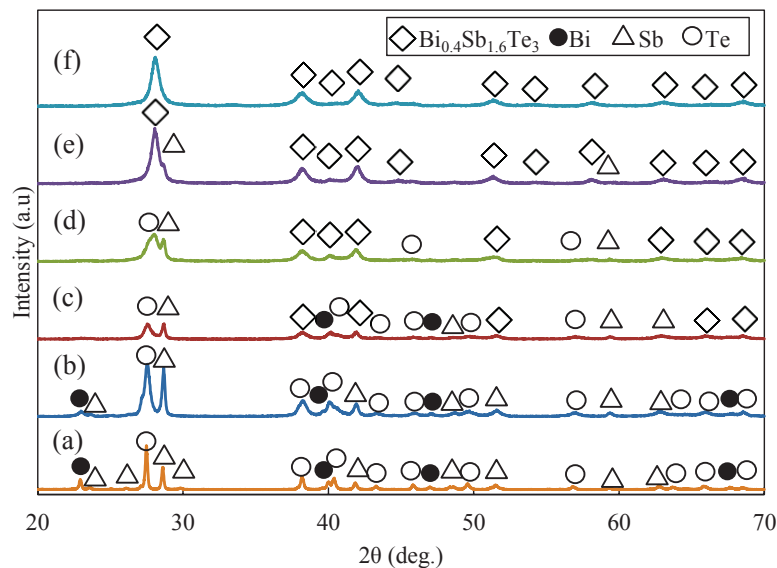


Fig. 2.3 XRD patterns of powders prepared by MA with different milling times of (a) 0 h, (b) 2 h, (c) 4 h, (d) 8 h, (e) 12 h, and (f) 24 h.

Fig. 2.4 shows the SEM images of the MAed powders (24 h) under different weight ratios. There is no obvious difference between the particle morphologies of these two MAed powders. However, compared with the starting powders as shown in Fig 2.1, the MAed powders exhibit much more homogeneous and smaller particles.
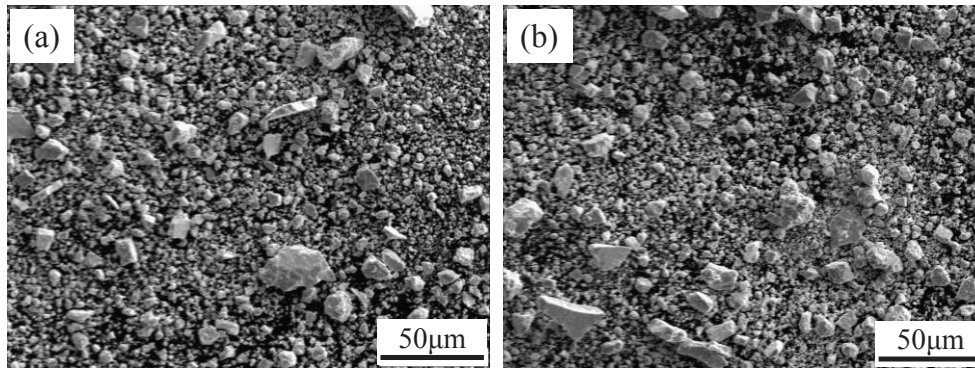
Fig. 2.4 SEM images of the MA powders with different ball-powder weight ratios of (a) 15:1 and (b) 30:1.

Fig. 2.5 shows the XRD patterns of the powders prepared by MA (24 h) with different ball-powder weight ratios. The results indicate that both of these two patterns are attributed to $Bi_{0.4}Sb_{1.6}Te_3$ single-phase. However, the average crystallite sizes calculated by the Scherrer equation [5] are 61.62 and 48.14 nm for the powders milled under ratios of 15:1 and 30:1, respectively. Although smaller crystallite size under a weight ratio of 30:1 is beneficial to grain refinement, the higher strain energy remained in the powder particles easily results in mechanical lattice defects [6, 7], which significantly affect the thermoelectric properties of $Bi_2Te_3$-based compounds [8-10]. Moreover, a large weight ratio easily results in incorporation of impurities from the milling media (balls and pot). Hereafter, in order to avoid much more defects and contamination from the milling media, all extruded samples were fabricated by using the powder prepared by MA for 24 h with a ball-powder ratio of 15:1.
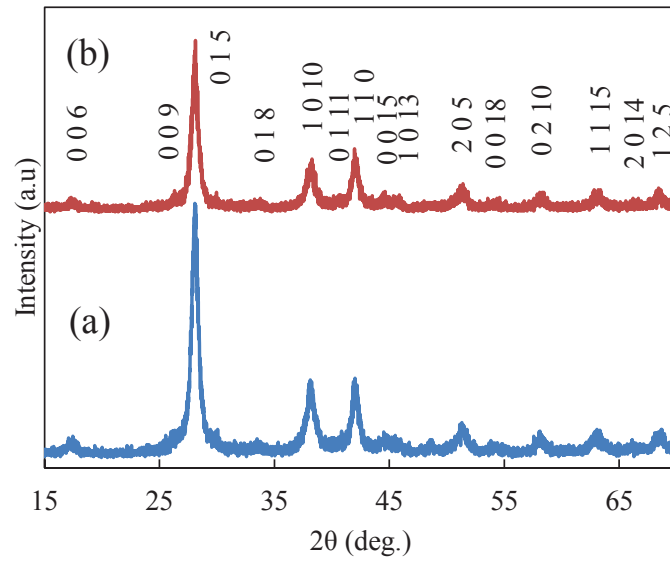
Fig. 2.5 XRD patterns of powders prepared by MA with different ball-powder weight ratios of (a) 15:1 and (b) 30:1.

## 2.3.2 Extrusion behavior

The extrusion pressure–stroke curves at different temperatures are shown in Fig. 2.6. The extrusion behavior was similar to each other at different temperatures. In the initial period, the billet is compacted in the container, resulting in a gradual increase in pressure. As the billet is further compacted and flows into the die, the pressure abruptly increases. Extrusion begins at the point where the pressure gradient starts to relax, followed by a steady increase of the pressure. As extrusion temperature decreases, the overall extrusion pressure tends to rise. This is attributed to the increase in the deformation resistance of the billet at lower temperatures.
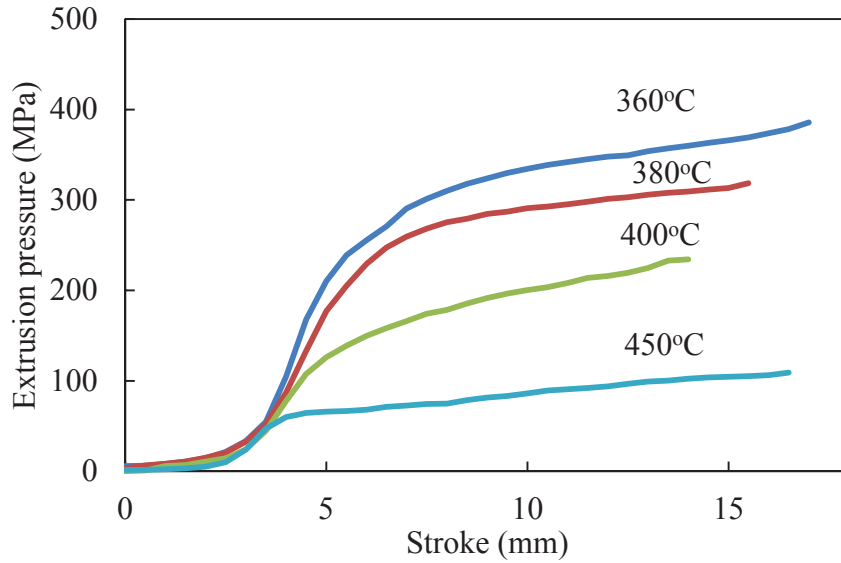
Fig. 2.6 Extrusion pressure versus stroke curves at different temperatures.

Fig. 2.7 shows the appearances of samples extruded at different temperatures. The extrudates were sound, and no evident cracks and other defects were found. All the samples extruded at temperatures ranging from 360$^{o}$C to 450$^{o}$C had high relative density of more than 97%, as shown in Fig. 2.8. These results indicate that dense and crack-free bulk extrudates can be obtained under the conditions used in this work.
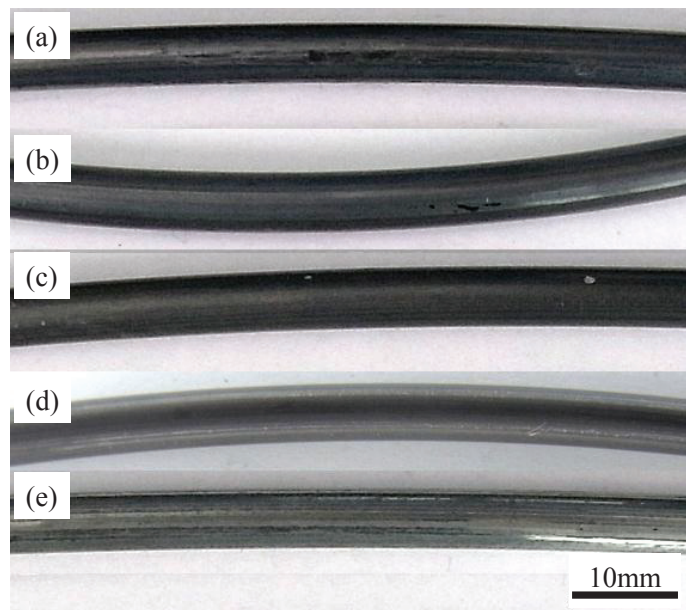


Fig. 2.7 Appearances of samples extruded at (a) 360$^{o}$C, (b) 380$^{o}$C, (c) 400$^{o}$C, (d) 420$^{o}$C, and (e) 450$^{o}$C.
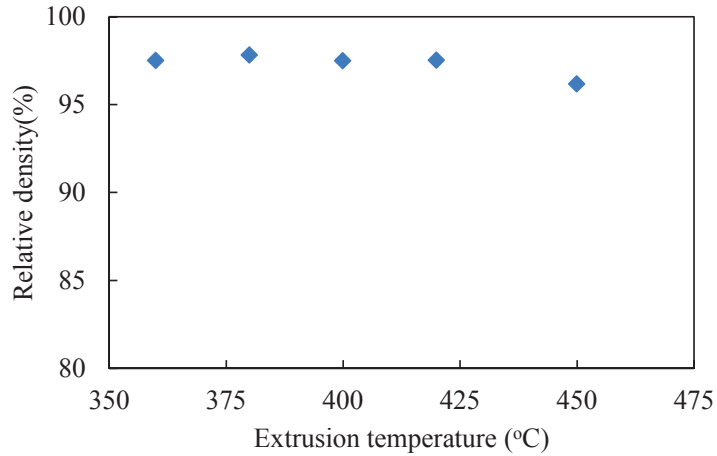
Fig. 2.8 Relative density of the extruded samples.

## 2.3.3 Microstructure and texture

Fig. 2.9 illustrates the XRD patterns measured on the longitudinal and transverse sections of the sample extruded at 400°C. As a reference, the pattern of as-MAed powder is also included. The longitudinal section whose normal direction is perpendicular to the extrusion direction exhibited much stronger diffraction intensities on (0 0 $l$) basal planes such as (0 0 6), (0 0 9), (0 0 15) and (0 0 18). This result indicates that the basal planes are preferentially oriented parallel to the extrusion direction after the hot extrusion. Similar results have been confirmed in other samples extruded at different temperatures.
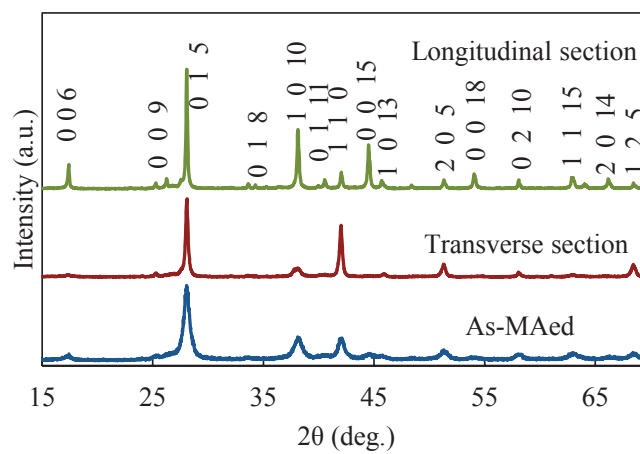


Fig. 2.9 XRD patterns on the longitudinal and transverse sections of the sample extruded at 400°C.

Fig. 2.10 shows XRD patterns of the extruded samples obtained from longitudinal sections. The results indicated that the XRD patterns of the extruded samples were similar to each other. All the samples were attributed to $Bi_{0.4}Sb_{1.6}Te_3$ single phase. No impurity phase was found in the samples within the whole extrusion temperature range. The orientation degree of the extruded samples was calculated based on XRD data using Lotgering method [4]. Fig. 2.11 shows the dependence of orientation factor $f_{(00l)}$ on extrusion temperature. The orientation factor gradually increased with increasing the extrusion temperature below 400$^o$C due to the grain growth, as demonstrated below, where highly oriented textures are easy to form in large grains [11, 12], but it was sharply reduced after the peak at 400$^o$C. The reason for the decrease in orientation degree at >400$^o$C is related to a second phase of Te-rich phase, which will be discussed in detail in Chapter 4.
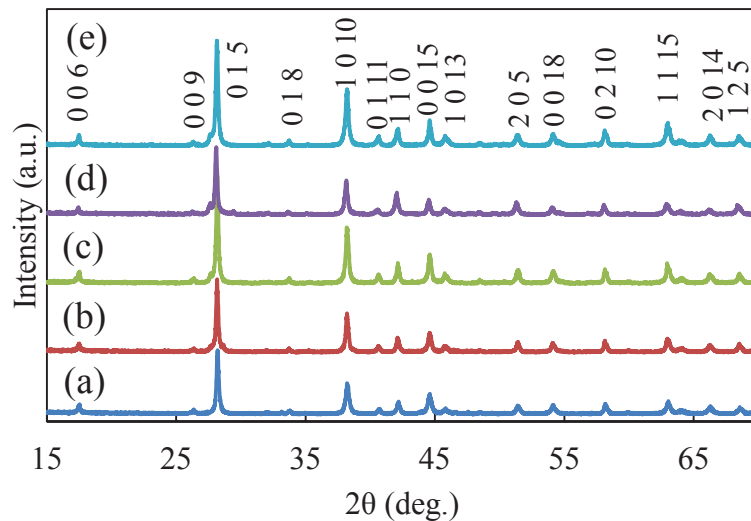


Fig. 2.10 XRD patterns of the samples extruded at (a) 360$^o$C, (b) 380$^o$C, (c) 400$^o$C, (d) 420$^o$C, and (e) 450$^o$C.
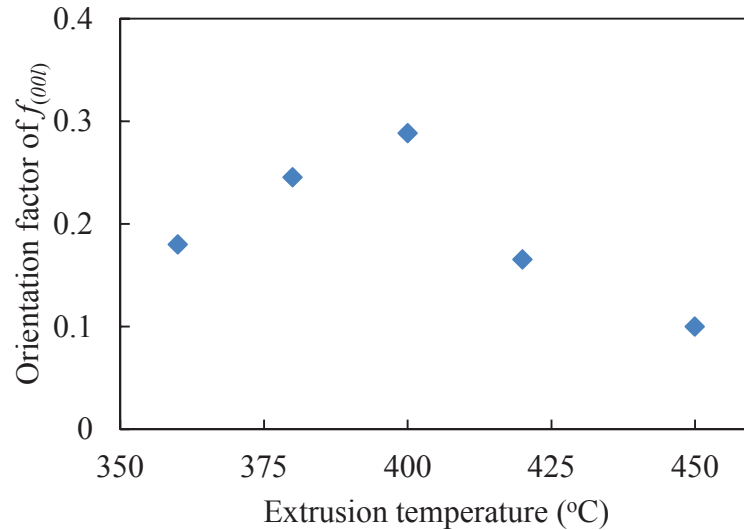
Fig. 2.11 Dependence of orientation factor $f_{(00l)}$ on extrusion temperature.

The OIM maps on the longitudinal sections of the extruded samples are shown in Fig. 2.12. As for the sample extruded at 360$^{\circ}$C, the microstructure is characterized by equiaxed grains with approximately submicron dimensions and elongated grains along the extrusion direction. This suggests that dynamic recrystallization has started to occur during the extrusion process even at such a low temperature. With increasing extrusion temperature, the grain size gradually increases. The average grain sizes were measured as 0.68 μm, 0.82 μm, 1.04 μm, 1.60 μm, and 3.9 μm at 360$^{\circ}$C, 380$^{\circ}$C, 400$^{\circ}$C, 420$^{\circ}$C, and 450$^{\circ}$C, respectively. Fig. 2.13 shows the corresponding (0 0 0 1) pole figures of the extruded samples. It is clearly shown that the (0 0 0 1) basal plane is predominantly oriented in the extrusion direction even at the higher temperature of 450$^{\circ}$C, which agrees well with the XRD result (Fig. 2.9).

The above results indicate that $Bi_{0.4}Sb_{1.6}Te_3$ bulk materials with oriented fine-grained microstructures are effectively obtained by use of a combination of MA and hot extrusion.
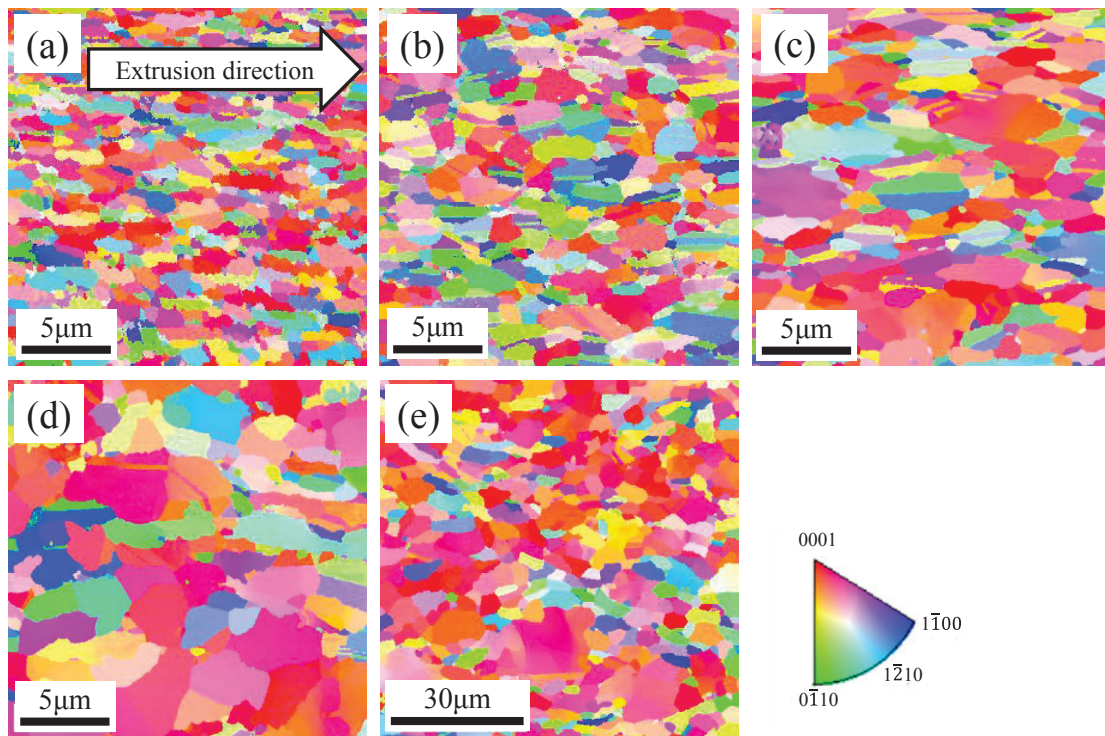
Fig. 2.12 OIM maps on longitudinal sections of the samples extruded at (a) 360$^{o}$C, (b) 380$^{o}$C, (c) 400$^{o}$C, (d) 420$^{o}$C, and (e) 450$^{o}$C.
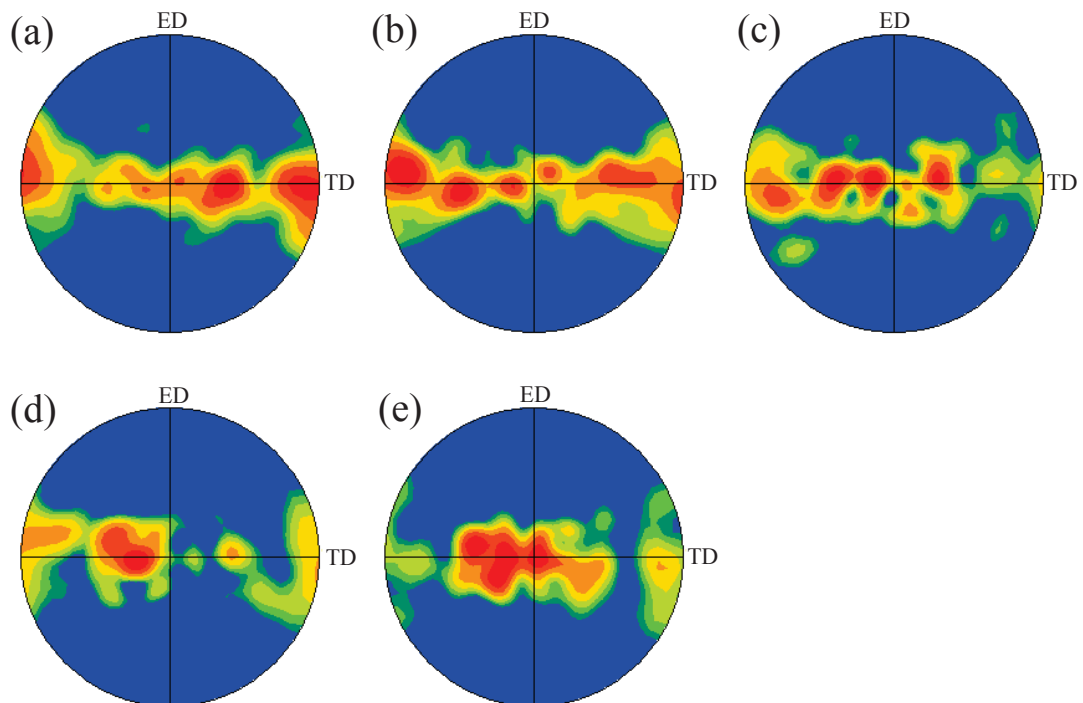


Fig. 2.13 (0001) pole figures of the samples extruded at (a) 360$^{o}$C, (b) 380$^{o}$C, (c) 400$^{o}$C, (d) 420$^{o}$C, and (e) 450$^{o}$C.

2.3.4 Thermoelectric properties

The dependence of the Seebeck coefficient on measuring temperature is shown in Fig. 2.14. The Seebeck coefficient exhibited a higher level at room temperature for all the extruded samples. In the whole extrusion temperature range, the sample extruded at $360^oC$ has the lowest values. Furthermore, at room temperature, the Seebeck coefficients of the samples extruded in the temperature range of $380\sim400^oC$ are higher than those for samples extruded at $360^oC$ and $450^oC$. The lower value of the Seebeck coefficient in the sample extruded at $360^oC$ might be related to more remained lattice defects at a lower extrusion temperature. On the other hand, the lower value for the sample extruded at $450^oC$ is related to the Te-rich phase (Chapter 4). As the measuring temperature increased, the Seebeck coefficient slight increased and showed the highest level at measuring temperature range of $100\sim200^oC$.
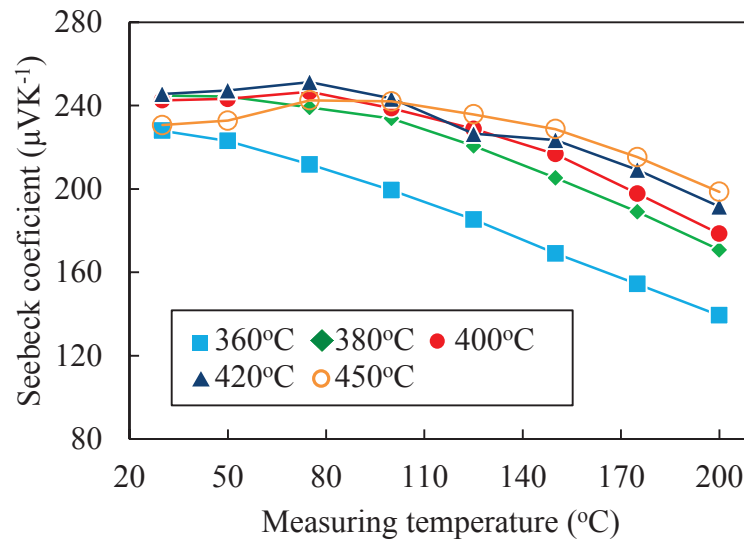


Fig. 2.14 Dependence of the Seebeck coefficient on measuring temperature.

Fig. 2.15 shows the dependence of the electrical resistivity on measuring temperature. A lower extrusion temperature results in greater electrical resistivity, with an exception at $420^oC$. This is because lower extrusion temperature leads to formation of a fine-grained microstructure, hence resulting in increases in scattering of carriers and thus electrical resistivity. This suggests that grain boundary scattering is most likely to be a dominant factor contributing to the electrical resistivity of this

26

material.
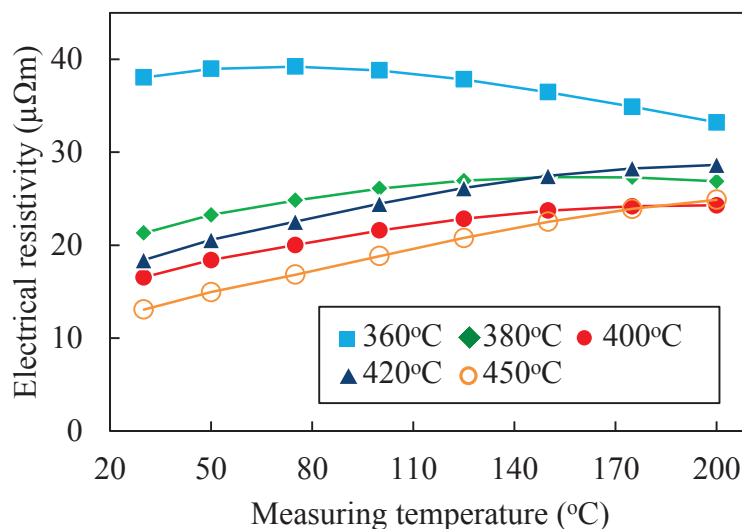


Fig. 2.15 Dependence of the electrical resistivity on measuring temperature.

Fig. 2.16 shows the dependence of thermal conductivity measured at room temperature on extrusion temperature. In the extrusion temperature range of $360\sim450^{\circ}C$, the thermal conductivity is approximately 1 W/mK, which is similar to the reported value [13]. This indicates that the extrusion temperature has a small effect on the thermal conductivity of the extruded $Bi_{0.4}Sb_{1.6}Te_3$ samples. The thermal conductivity, $\kappa$, is determined by lattice thermal conductivity ($\kappa_{ph}$) and electron thermal conductivity ($\kappa_{el}$), and it is described as $\kappa=\kappa_{ph}+\kappa_{el}$ [14], where the lattice ($\kappa_{ph}$) and electron ($\kappa_{el}$) thermal conductivities are strongly related to the scattering of phonons at grain boundaries and carrier concentration, respectively. Note that, large grains at high extrusion temperature as demonstrated in Fig. 2.12 should decrease the scattering of phonons at grain boundaries and thus increase $\kappa_{ph}$. However, the higher the extrusion temperature is, the less the remained lattice defects are, which results in a reduction of carrier concentration [15] and thus $\kappa_{el}$. Therefore, the small variation of thermal conductivity possibly results from the counteraction of $\kappa_{ph}$ and $\kappa_{el}$.
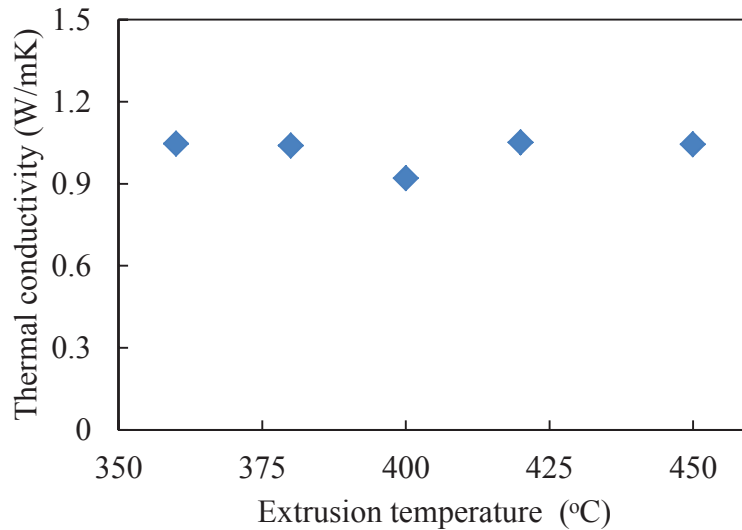
Fig. 2.16 Dependence of thermal conductivity measured at room temperature on extrusion temperature.

The dependence of the calculated dimensionless figure of merit $ZT$ on extrusion temperature is drawn in Fig. 2.17. As a result, the sample extruded at $400^{\circ}C$ has a maximum value of $ZT = 1.2$ at room temperature in this study.
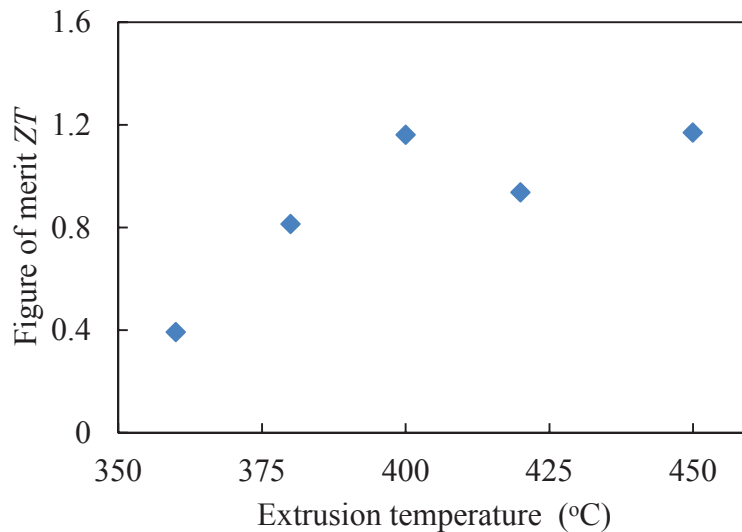


Fig. 2.17 Dependence of figure of merit $ZT$ on extrusion temperature.

2.3.5 Mechanical properties

Fig. 2.18 illustrates the dependence of Vickers hardness on extrusion temperature. The hardness decreases with increasing extrusion temperature due to the increased

grain size. Although the Vickers hardness exhibits a decreased tendency with increase in extrusion temperature, the minimum hardness value of the extruded samples is still almost 2 times larger than that of zone-melted sample [16].
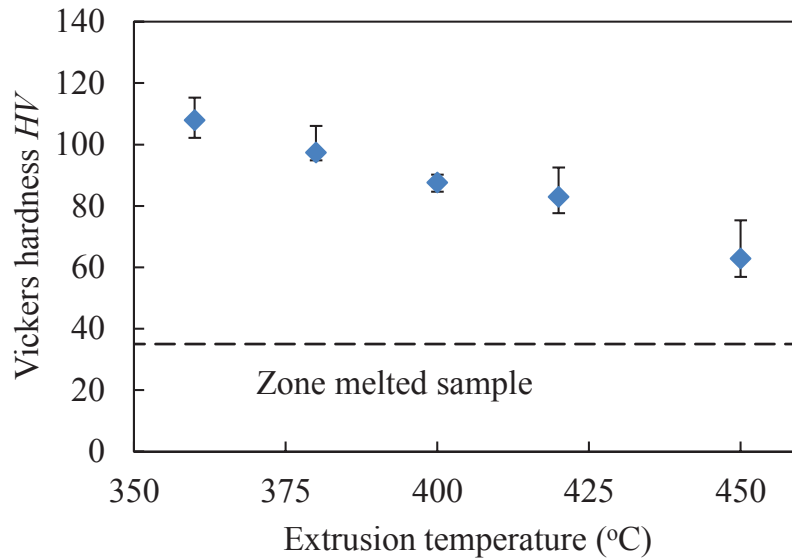


Fig. 2.18 Dependence of Vickers hardness on extrusion temperature.

## 2.4 Conclusions

In this chapter, the effect of MA conditions and extrusion temperature on microstructure, texture, and thermoelectric and mechanical properties was investigated. Some main findings of this chapter are summarized as follows.

(1) Highly dense p-type $Bi_{0.4}Sb_{1.6}Te_3$ bulk materials were successfully fabricated by MA and hot-extrusion technique.

(2) Fine-grained microstructure with preferred orientation was obtained for all the extruded samples.

(3) The basal planes in the extrudates were preferentially oriented parallel to the extrusion direction.

(4) A largest $ZT$ of 1.2 was obtained for the sample extruded at $400^{\circ}C$ at room temperature. The extruded samples showed high Vickers hardness, although there was a reduction with increasing extrusion temperature.

# References

[1] D. Vasilevskiy, J. M. Simard, F. Be´langer, F. Bernier, S. Turenne, J. L'Ecuyer, Proc. 21$^{st}$ Inter. Conf. on on Thermoelec., California, (2002) 24.

[2] S. Miura, Y. Sato, K. Fukuda, K. Nishimura, and K. Ikeda, Mater. Sci. Eng. A 277 (2000) 244.

[3] J. M. Simard, D. Vasilevskiy, F. Belanger, J. L'Ecuyer, and S. Turenne, Proc. 20$^{th}$ Inter. Conf. on on Thermoelec., Beijing, (2001) 132.

[4] F. K. Lotgering, J. Inorg. Chem. 9 (1959) 113-123.

[5] P. Scherrer, Math-Phys Klasse 2 (1918) 98-100.

[6] J. Navrátil, Z. Starý, T. Plecháček, Mater. Res. Bull. 31 (1996) 1559-1566.

[7] L. D. Zhao, B. P. Zhang, W. S. Liu, H. L. Zhang, J. F. Li, J. Alloys Compd. 467 (2009) 91-97.

[8] T. S. Oh, D. B. Hyum, N.V. Kolomoets, Scripta Mater. 42 (2000) 849-854.

[9] D. M. Lee, C. H. Lim, D. C. Cho, Y. S. Lee, C. H. Lee, J. Electron. Mater. 35 (2006) 360-365.

[10] J. M. Schultz, J. P. Mchugh, W. A. Tiller, J. Appl. Phys. 33 (1962) 2443-2450.

[11] K. Fukuda, H. Imaizumi, T. Ishii, F. Toyoda, M. Yamanashi, Y. Kibayashi, Proc. 15$^{th}$ Inter. Conf. on Thermoelec. (1996) 37.

[12] J. Jiang, L.D. Chen, S.Q. Bai, Q. Yao, Q. Wang, Mater. Sci. Eng., B 117 (2005) 334-338.

[13] X. A. Fan, J. Y. Yang, R. G. Chen, W. Zhu, S. Q. Bao, Mater. Sci. Eng. A 190 (2006) 438-440.

[14] T.S. Kim, I.S. Kim, T.K. Kim, S.J. Hong, B.S. Chun, Mater. Sci. Eng. B 90 (2002) 42–46.

[15] W. S. Liu, Q. Zhang, Y. Lan, S. Chen, X. Yan, Q. Zhang, H. Wang, D. Z. Wang, G. Chen, Z. F. Ren, Adv. Energy Mater. 1(4) (2011) 577-587.

[16] Z. J. Xu et al., Acta Mater. 84 (2015) 385-392.

# Chapter 3 Fabrication of *n*-type Bi-Te-Se bulk materials by MA and hot-extrusion technique

## 3.1 Introduction

As is well known, both *n*-type and *p*-type semiconductors are essential for a thermoelectric device. In Chapter 2, *p*-type Bi-Te-Sb bulk materials have been successfully fabricated by MA and hot-extrusion technique. The purpose of this chapter is to fabricate *n*-type $Bi_2Te_{2.85}Se_{0.15}$ bulk thermoelectric materials by MA and hot-extrusion technique and understand the relationships among processing conditions, extrusion behavior, microstructure, texture, thermoelectric and mechanical properties.

## 3.2 Experimental procedure

### 3.2.1 Starting materials

High purity Bi (99.99%, 63~106 µm), Se (99.9%, 10 µm), and Te (99.99%, 45µm) powders were used as the starting materials. Bi and Te powders used in this chapter are the same as those used in Chapter 2. Se powder exhibits homogeneous morphology with particle sizes of <10 µm observed from the SEM image of Se (Fig. 3.1).
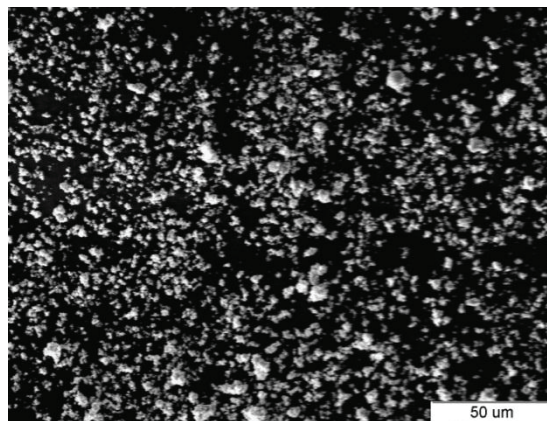


Fig. 3.1 SEM image of Se.

### 3.2.2 Preparation of alloy powder by MA

The starting powders were pre-mixed in a mortar and pestle, and then subjected to MA in a planetary ball milling system using an argon-filled $Al_2O_3$ pot and $ZrO_2$ ($\Phi$10mm) balls. The MA conditions are listed in Table 3.1.

Table 3.1 MA conditions.

| Ball: powder (weight) | 20:1 |
|---|---|
| Rotation speed | 200 rpm |
| Milling time | 0~24 h |
| Atmosphere | Ar |

### 3.2.3 Consolidation by hot extrusion

The MAed powders were pressed into a cylindrical green compact at the room temperature by uniaxial pressing to obtain a billet used for hot extrusion. The cold-pressing conditions refer to that as listed in Table 2.2.

The obtained billet was subjected to hot extrusion subsequently. The extrusion conditions are listed in Table 3.2.

Table 3.2 Conditions of hot extrusion.

| Extrusion billet | Cold-pressed compact |
|---|---|
| Atmosphere | Air |
| Extrusion temperature | 340~450℃ |
| Extrusion ratio | 25 |
| Extrusion speed | 1mm/min |

### 3.2.4 Characterization

The density of the extruded samples was determined by the Archimedes method. Phase identification was performed by X-ray diffraction (XRD) with Cu Kα radiation. The orientation degree was determined using the Lotgering method [1]. Microstructural observation and compositional analysis were conducted by scanning electron microscopy (SEM) and energy dispersive X-ray spectroscopy (EDS), respectively. Orientation imaging microscopy (OIM) analysis was performed using an

SEM equipped with an electron backscattered diffraction (EBSD) system (JEOL-7001FA). The OIM maps and pole figures were obtained from analysis of the EBSD data by the software TSL-OIM analysis 6.2.

The electron transport properties were evaluated by a Hall effect measurement system (TOYO Corp., Resi Test 8300). The Seebeck coefficient ($\alpha$) and electrical resistivity ($\rho$) of the samples were simultaneously measured by static DC method and four-probe method, respectively, using a thermoelectric property test apparatus (ULVAC-RIKO, ZEM-3). The thermal conductivity ($\kappa$) was measured by laser flash method (NETZSCH, LFA457 Micro Flash). In the thermal conductivity measurements, the direction of the heat flux was set to the extrusion direction. The dimensionless figure of merit of the samples was calculated by the equation of $ZT=\alpha^2 T/(\rho\kappa)$.

The mechanical properties at room temperature were evaluated by the Vickers hardness tests at a load of 1.96 N (Shimadzu, HMV-2000). Details of the evaluation methods have been described in section 2.2.4.

## 3.3 Results and discussion

### 3.3.1 Preparation of alloy powders

The starting powders with a nominal composition of $Bi_2Te_{2.85}Se_{0.15}$ were milled with different times up for 24 h. The XRD patterns of the as-mixed and MAed powders are shown in Fig. 3.2. The peaks attributed to the raw powders disappeared and the broadened peaks from $Bi_2Te_{2.85}Se_{0.15}$ phase occurred instead after MA. When the milling time reached 8 h, the powder can be regarded as a single-phase $Bi_2Te_{2.85}Se_{0.15}$ solid solution, as shown in Fig. 3.2(c). The average crystallite sizes calculated by Scherrer equation [2] were 11.30 nm, 10.47 nm, and 9.96 nm for MAed-8h, MAed-12h, and MAed-24h powders, respectively. There is no significant reduction in crystallite size with increasing the milling time. In order to avoid more contamination and mechanical defects induced by MA, all extruded samples were fabricated by using the powder prepared by MA for 12 h. The morphology of the MAed powder is shown in Fig. 3.3. The powder exhibited fine particles with an

average diameter of < 1μm.
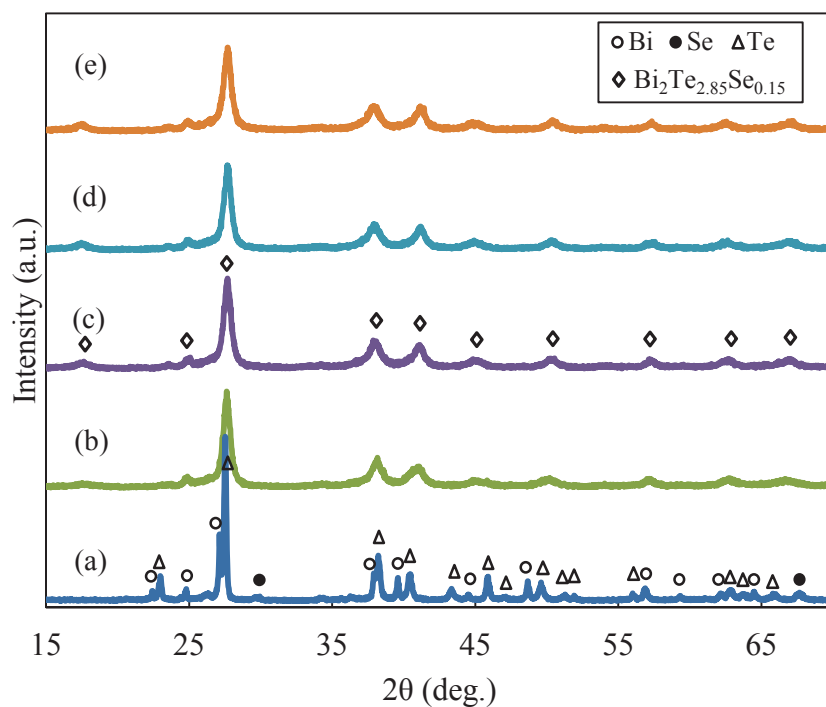


Fig. 3.2 XRD patterns of (a) as-mixed, (b) MAed-4h, (c) MAed-8h, (d) MAed-12h, and (e) MAed-24h powders.
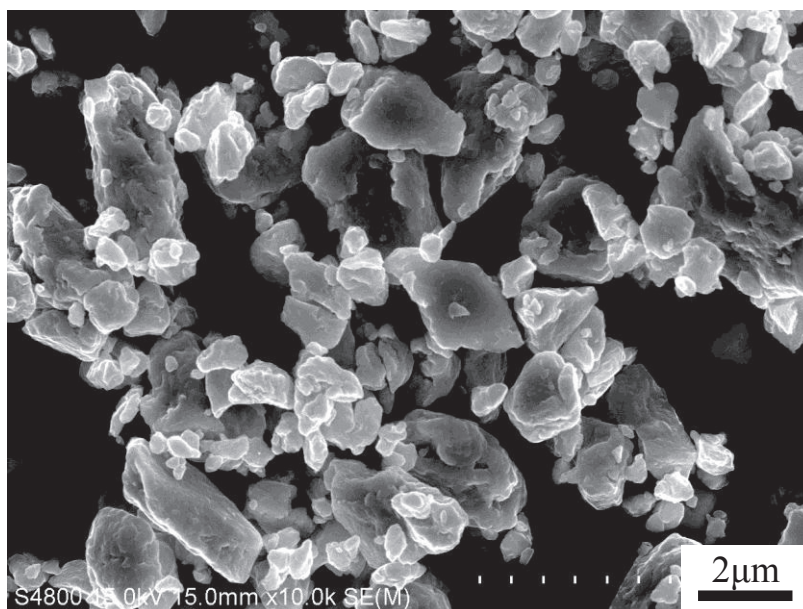


Fig. 3.3 SEM image of $Bi_2Te_{2.85}Se_{0.15}$ powder MAed for 12h.

3.3.2 Extrusion behavior

Fig. 3.4 shows the extrusion pressure–stroke curves at different temperatures. In the initial period, the billet is compacted in the container, resulting in a gradual increase in pressure. As the billet is further compacted and flows into the die, the pressure abruptly increases. The extrusion begins at the point where the pressure attains a peak or the pressure gradient starts to relax. In the steady extrusion stage, the pressure change was small. As the extrusion temperature decreased, the pressure level increased, because of larger deformation resistance of the billet at a lower temperature.
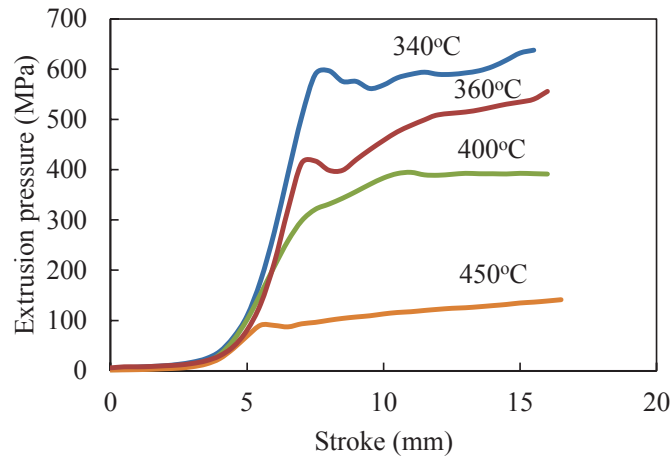


Fig. 3.4 Extrusion pressure–stroke curves at different temperatures.

Fig. 3.5 shows the appearances of the samples extruded in a temperature range of 340-450$^{o}$C. It is shown that all the samples exhibited sound appearances and no evident defects were observed. Furthermore, all the extrudates had high relative density values of >98%. It was noted that the surfaces of the extrudates became rough when the extrusion temperature was >450$^{o}$C. Under the conditions used in the present work, dense, crack-free and single phase $Bi_2Te_{2.85}Se_{0.15}$ bulk extrudates can be obtained in a temperature range of 340~450$^{o}$C.
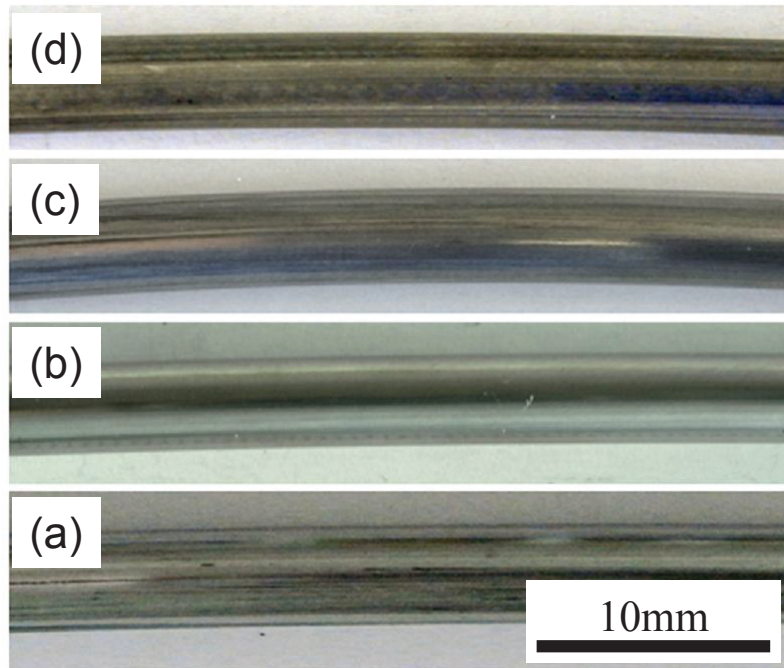
Fig. 3.5 Appearances of the samples extruded at (a) 340$^{\circ}$C, (b) 360$^{\circ}$C, (c) 400$^{\circ}$C, and (d) 450$^{\circ}$C.

### 3.3.3 Microstructure and texture

The OIM maps and corresponding (0 0 0 1) pole figures at different positions of an extruded sample are shown in Fig. 3.6, which were measured on the longitudinal section parallel to the extrusion direction. At position "a", where the powder was subjected to compaction during both cold pressing and subsequent hot extrusion, the basal plane (0 0 0 1) is oriented perpendicular to the extrusion direction. As the extrusion proceeds, the (0 0 0 1) pole gradually appears on the equatorial axis of the projection (position "b"). At position "c", a fiber texture is formed, which is parallel to the extrusion direction. These results are in good agreement with the extrusion behavior of Bi$_2$Te$_3$ compound [3]. After extrusion, the microstructure was characterized by fine and equiaxed grains, and the average grain size was measured as 0.54 μm (Fig. 3.6(c)). This is mainly due to the dynamic recrystallization during the extrusion and static recrystallization after the extrusion [3]. The above results suggest that the basal plane is gradually rotated from an orientation perpendicular to the extrusion direction to an orientation parallel to the extrusion direction during the extrusion process. This is beneficial to improving the thermoelectric performance of

the extruded materials.
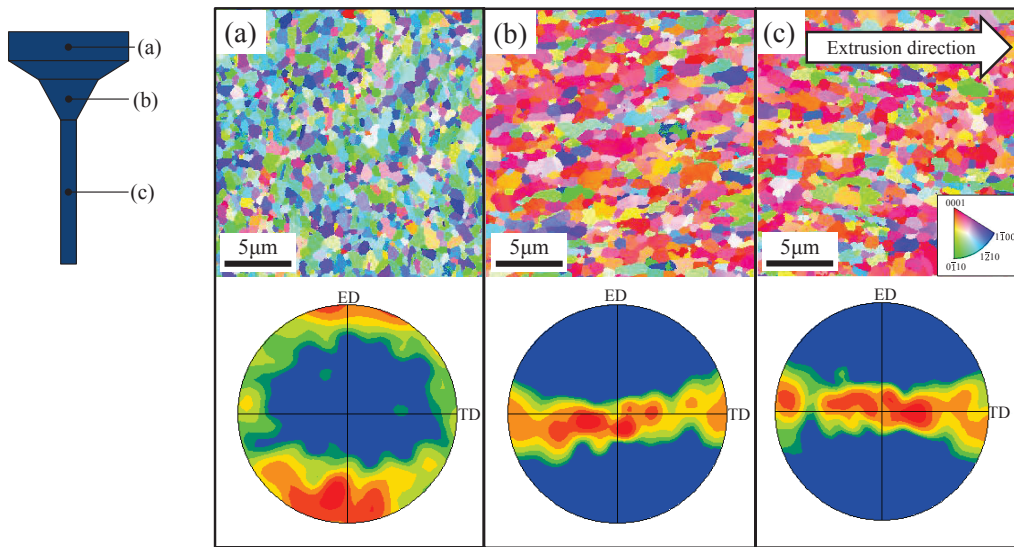


Fig. 3.6 OIM maps and (0 0 0 1) pole figures on longitudinal section at different positions of the sample extruded at 360°C (ED: extrusion direction and TD: transverse direction).

Fig. 3.7 illustrates the XRD patterns measured on the longitudinal and transverse sections of the sample extruded at 360°C. As a reference, the pattern of as-MAed powder is also included in Fig. 3.7. The longitudinal section exhibited much stronger diffraction intensities on (0 0 $l$) basal planes such as (0 0 6) and (0 0 15). These results also indicate that the basal planes are preferentially oriented parallel to the extrusion direction after the hot extrusion. Similar results have been confirmed in other samples extruded at different temperatures. The SEM images of the fracture surfaces of the sample extruded at 360°C are shown in Fig. 3.8. Layered and flaky morphologies are observed on the fracture surfaces which are perpendicular and parallel to the extrusion axis, respectively, indicating preferential deformation along the basal planes during the hot extrusion. This is in good agreement with the EBSD and XRD results mentioned above.
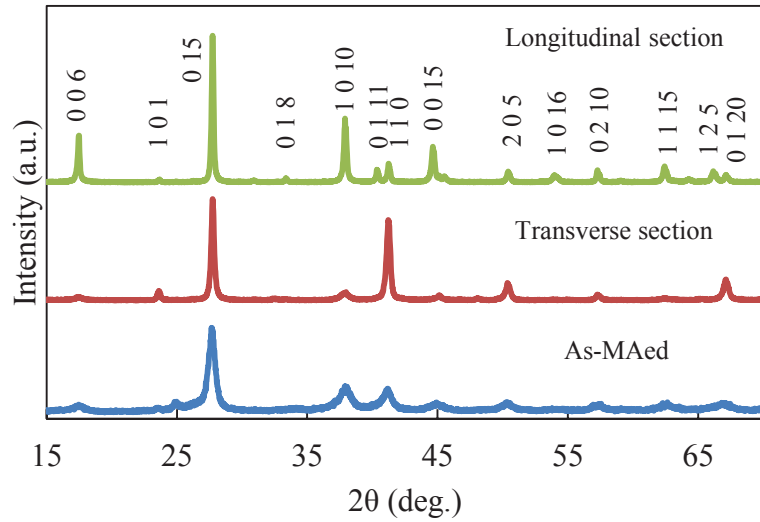
Fig. 3.7 XRD patterns on the longitudinal and transverse sections of the sample hot-extruded at 360°C.
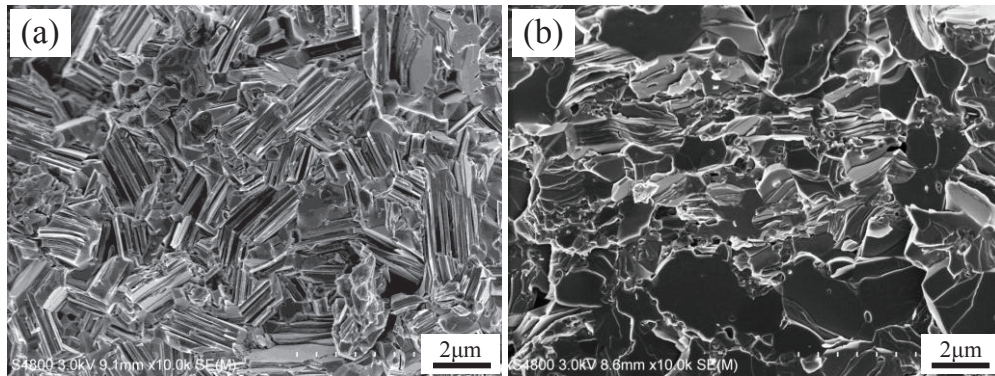


Fig. 3.8 SEM images of the fracture surfaces, (a) perpendicular and (b) parallel to the extrusion axis.

The OIM maps on the longitudinal sections of the samples extruded at different temperatures are shown in Fig. 3.9. It was easily found from Fig. 3.9 and Fig. 3.6(c) (T=360°C) that the grains grew up gradually with the increase in extrusion temperature. The average grain sizes were measured as 0.41 μm, 0.54 μm, 0.75 μm, and 1.24 μm at 340°C, 360°C, 400°C, and 450°C, respectively. Accordingly, with the help of mechanical alloying and hot-extrusion processes, fine-grained microstructure with a submicron order can be obtained at extrusion temperatures of ≤400°C. But at 450°C, many elongated grains are observed as shown in Fig. 3.9(c). This is probably due to the generation of Te-rich and Te-poor phases which deviate from the nominal

composition of Te in $Bi_2Te_{2.85}Se_{0.15}$ compound.
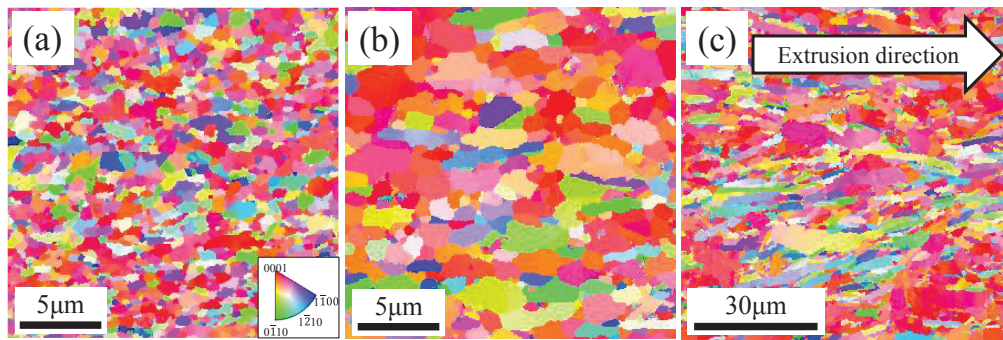


Fig. 3.9 OIM maps on the longitudinal sections of the samples extruded at (a) 340$^o$C, (b) 400$^o$C, and (c) 450$^o$C.

Fig. 3.10 shows an SEM image of the sample extruded at 450$^o$C. There are some dark regions with larger sizes (*e. g.*, "P$_1$") and light-grey regions with smaller sizes (*e.g.*, point "P$_2$"), which are distributed in the matrix. The EDS composition analysis indicated that the Te contents in the dark and light-grey regions were much higher (*e. g.*, 96.83 at% for point "P$_1$") and slightly lower (an average value of 52.01 at%) than the nominal composition of Te (57 at%) in $Bi_2Te_{2.85}Se_{0.15}$ compound, respectively. Thus, the dark regions can be regarded as a Te-rich phase, which may result from the eutectic reaction occurring when the sample is extruded out of the die at an extrusion temperature of ≥413$^o$C based on the phase diagram [4]. On the other hand, the light-grey Te-poor phase is considered to be attributed to the sublimation of Te from the matrix during the hot extrusion due to a high vapour pressure of Te [5]. The formation of some elongated grains shown in Fig. 3.9(c) may be associated with the inhomogeneous distribution of the Te-poor phase. For example, a region indicated by an arrow "R" in Fig. 3.10 showed an elongated morphology, which was surrounded by the Te-poor phase. It should be noted that it is difficult to detect the peaks attributed to Te-rich and Te-poor phase in the XRD patterns, because the former has a small amount and the latter has compositions close to the nominal composition. Detailed formation mechanisms of the Te-rich and Te-poor phases and related microstructure feature will be discussed in the next chapter.
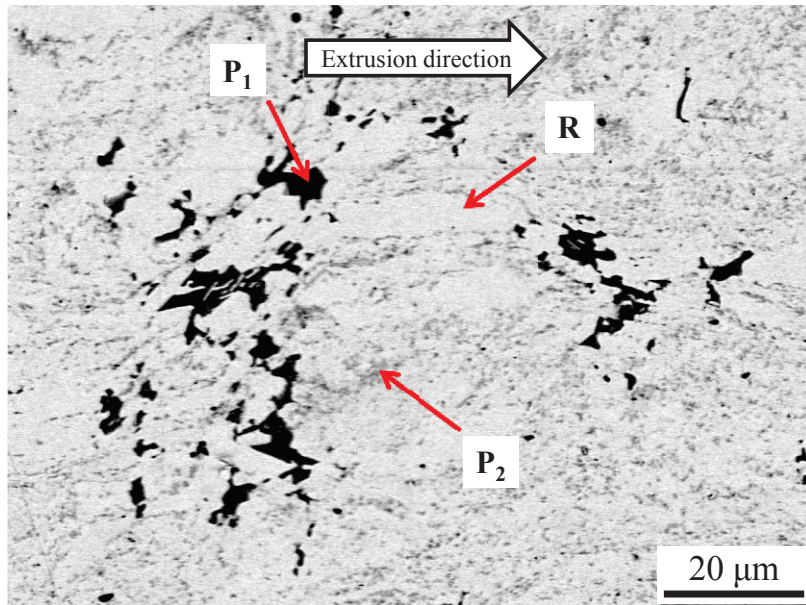
Fig. 3.10 SEM image of the sample extruded at 450$^\circ$C.

The above results of microstructural observations reveal that the extruded samples show preferential orientations along the extrusion direction after the extrusion. The quantitative evaluation of (0 0 $l$) orientation in the extruded samples has been conducted according to the Lotgering method [1]. Fig. 3.11 shows the dependence of the orientation factor $f_{(00l)}$ on extrusion temperature. The orientation factor gradually increased with increasing the extrusion temperature below 400$^\circ$C, but it was slightly reduced at 450$^\circ$C. It has been reported that highly oriented textures are easy to form in large grains [6, 7]. The reason for the decrease in orientation degree at 450$^\circ$C may be also related to the generation of the Te-poor phase.
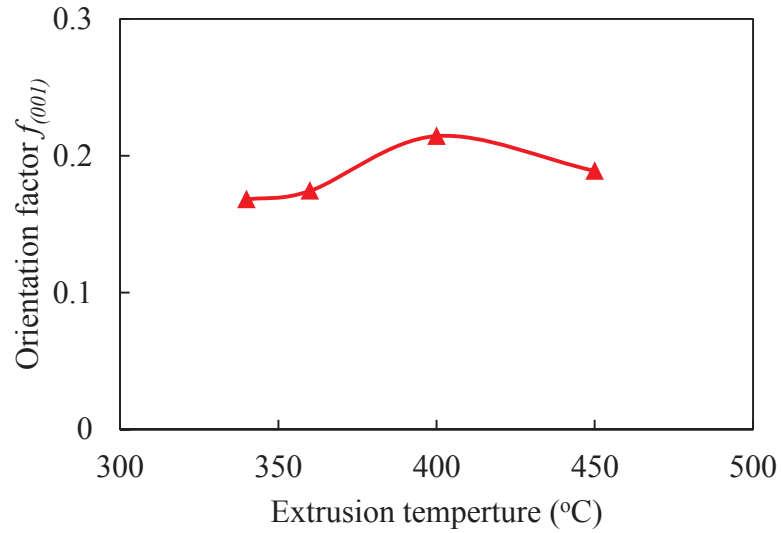
Fig. 3.11 Dependence of orientation factor $f_{(00l)}$ on extrusion temperature.

### 3.3.4 Thermoelectric properties

Fig. 3.12 shows the dependence of electron transport properties on extrusion temperature. The carrier concentration gradually increased with increasing the extrusion temperature. The Hall mobility exhibited the same tendency as the carrier concentration when the extrusion temperature is lower than $400^{\circ}C$, but it was slightly reduced at $450^{\circ}C$.
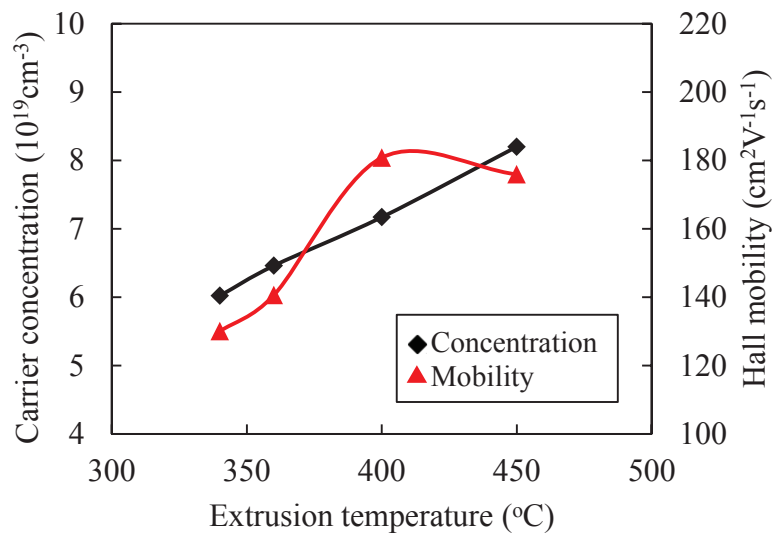


Fig. 3.12 Dependence of electron transport properties on extrusion temperature.

It is well known that carrier concentration is highly sensitive to chemical composition and lattice defects in atomic scale [8-10]. Recently, some researches focus on the effect of those point defects resulting from mechanical deformation on the transport properties [11-13]. Liu et al. [11] pointed out that the evaporation of Te is much easier than that of Bi since Te has a lower energy of evaporation (52.55 kJ/mol) than Bi (104.80 kJ/mol). The evaporation of each Te results in formation of one Te vacancy $[V_{Te}]$ with two free electrons $[e]$, which can be expressed by the following equation [11]:

$$Bi_2Te_3 = 2Bi_{Bi}^{\times} + (3-x)Te_{Te}^{\times} + xTe(g)\uparrow + xV_{Te}^{2+} + 2xe^-$$  (3.1)
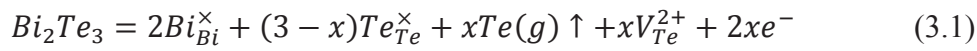
In this work, high extrusion temperature leads to significant evaporation of Te, and thus increase in carrier concentration. On the other hand, the mobility parallel to the basal plane is larger than that perpendicular to the basal plane, and it is significantly related to orientation degree [14]. Thus, similar dependences of the mobility and orientation factor on extrusion temperature are obtained.

Fig. 3.13 shows the extrusion temperature dependence of the Seebeck coefficient and electrical resistivity of the hot-extruded samples, measured at room temperature. As the extrusion temperature rose, both the absolute value of the Seebeck coefficient and electrical resistivity were reduced. The Seebeck coefficient and electrical resistivity are significantly related to electron transport properties. The relationship between the Seebeck coefficient and carrier concentration can be given by the following equation [15]:

$$\alpha \approx \gamma - \ln n$$  (3.2)

where $\alpha$, $\gamma$ and $n$ are the Seebeck coefficient, the scattering factor, and the carrier concentration, respectively. Thus, the decreased level of the Seebeck coefficient is

mainly due to the increased carrier concentration with increasing the extrusion temperature.

Electrical resistivity depends on carrier concentration and mobility, and the corresponding relationship can be described by the following equation:

$$\rho = \frac{1}{ne\mu} \tag{3.3}$$

where $\rho$, $e$ and $\mu$ are the electrical resistivity, the electron charge, and the carrier mobility, respectively. From the results shown in Fig. 3.12, the decrease in electrical resistivity with increasing extrusion temperature is mainly attributed to the increase in both carrier concentration and mobility. Moreover, a lower extrusion temperature leads to formation of a fine-grained microstructure, hence resulting in increase in scattering of carriers and thus electrical resistivity.
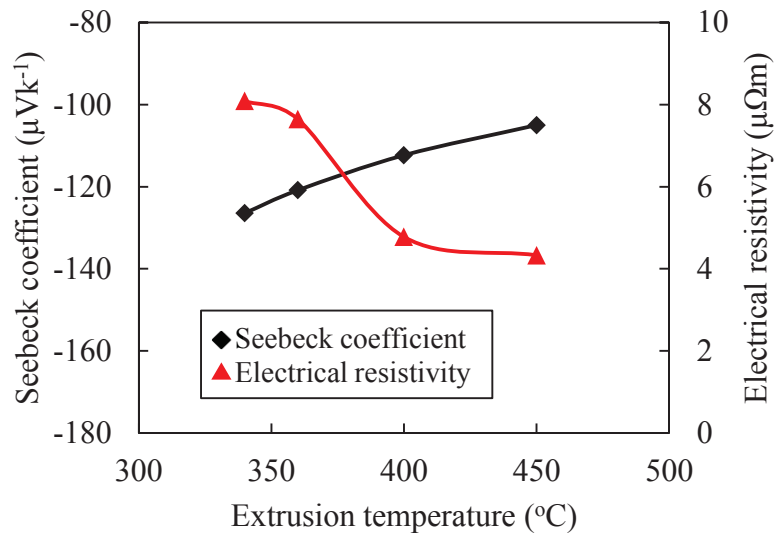


Fig. 3.13 Dependences of the Seebeck coefficient and electrical resistivity on extrusion temperature.

Fig. 3.14 shows the dependence of thermal conductivity and figure of merit (*ZT*) on extrusion temperature. The thermal conductivity increased with increasing the extrusion temperature. The thermal conductivity, $\kappa$, is determined by lattice thermal conductivity ($\kappa_{ph}$) and electron thermal conductivity ($\kappa_{el}$) [16]:

$$\kappa = \kappa_{ph} + \kappa_{el} \tag{3.4}$$

The lattice ($\kappa_{ph}$) and electron ($\kappa_{el}$) thermal conductivities depend on the scattering

of phonons and electrons, respectively. In this work, one of the reasons for increased thermal conductivity ($\kappa$) with increasing the extrusion temperature is grain growth at a higher temperature, which causes the decrease in phonons scattering from grain boundaries and thus increase in thermal conductivity. Another reason is the increased carrier concentration, which leads to the increase in $\kappa_{el}$. As a result, a largest *ZT* value of 0.47 was obtained at room temperature for the sample extruded at 400°C.
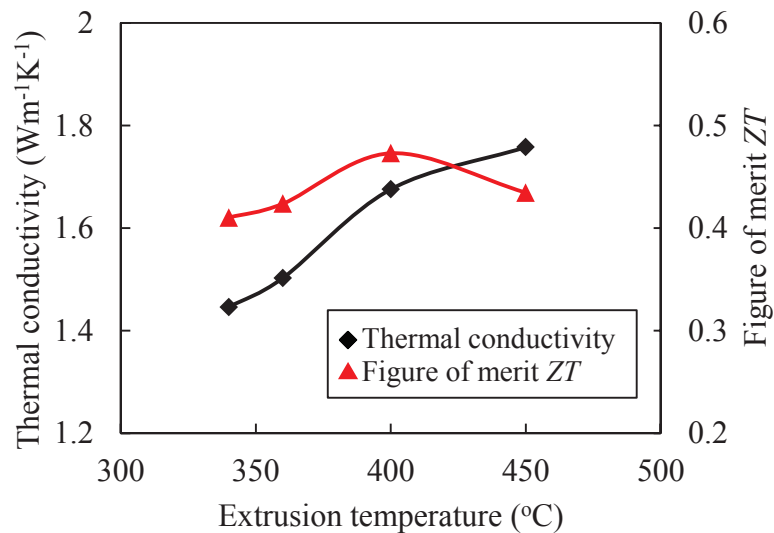


Fig. 3.14 Dependence of thermal conductivity and figure of merit (*ZT*) on extrusion temperature.

### 3.3.5 Mechanical properties

Fig. 3.15 shows the Vickers hardness as a function of extrusion temperature. The hardness monotonically decreased with increasing the extrusion temperature. The reason for this tendency is that a lower extrusion temperature results in a smaller average grain size. Although the Vickers hardness exhibits a decreased tendency as the increasing extrusion temperature, the lowest hardness value is still 2 times larger than that for hot-pressed sample [17].
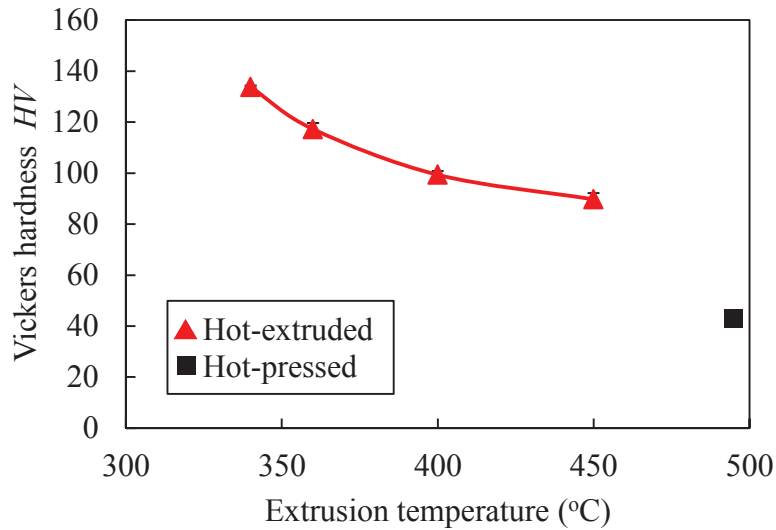
Fig. 3.15 Dependence of Vickers hardness on extrusion temperature.

## 3.4 Conclusions

In this chapter, the effect of extrusion temperature on extrusion behavior, microstructure, texture, thermoelectric and mechanical properties was investigated. Some main findings of this chapter are summarized as follows.

(1) Sound and dense $n$-type $Bi_2Te_{2.85}Se_{0.15}$ bulk thermoelectric materials were successfully fabricated by MA and hot-extrusion technique.

(2) Fine-grained microstructure with a submicron order was obtained at extrusion temperatures of $\leq 400°C$.

(3) The basal planes in the extrudates were preferentially oriented parallel to the extrusion direction.

(4) The carrier mobility was found to be related to the orientation degree of the basal planes. As the extrusion temperature increased, carrier concentration and thermal conductivity increased, whereas the absolute value of the Seebeck coefficient and electrical resistivity decreased. A largest dimensionless figure of merit value of 0.47 was achieved at room temperature for the sample extruded at 400°C.

(5) Although the Vickers hardness was reduced with increasing the extrusion temperature due to grain growth, all the extruded samples exhibited high hardness values.

## References

[1] F. K. Lotgering, J. Inorg. Chem. 9 (1959) 113-123.

[2] P. Scherrer, Math-Phys Klasse 2 (1918) 98-100.

[3]  Z. C. Chen, K. Suzuki, S. Miura, K. Nishimura, K. Ikeda, Mater. Sci. Eng., A 500 (2009) 70-78.

[4] A. Brown, B. Lewis, J. Phys. Chem. Solids 23 (1962) 1597-1604.

[5]  Y. Suga, Thermoelectric semiconductor, Makisyoten, Tokyo, 1966.

[6] K. Fukuda, H. Imaizumi, T. Ishii, F. Toyoda, M. Yamanashi, Y. Kibayashi, Proc. 15th Inter. Conf. on Thermoelec. (1996) 37.

[7] J. Jiang, L. D. Chen, S. Q. Bai, Q. Yao, Q. Wang, Mater. Sci. Eng., B 117 (2005) 334-338.

[8] L. D. Zhao, B. P. Zhang, W.S. Liu, H.L. Zhang, J.F. Li, J. Alloys Compd. 467 (2009) 91-97.

[9] J. M. Schultz, J. P. Mchugh, W. A. Tiller, J. Appl. Phys. 33 (1962) 2443-2450.

[10] J. Navrátil, Z. Starý, T. Plecháček, Mater. Res. Bull. 31 (1996) 1559-1566.

[11] W. S. Liu, Q. Zhang, Y. Lan, S. Chen, X. Yan, Q. Zhang, H. Wang, D. Z. Wang, G. Chen, Z. F. Ren, Adv. Energy Mater. 1(4) (2011) 577-587.

[12] L. Hu, T. Zhu, X. Liu, X. Zhao, Adv. Funct. Mater. 24(33) (2014) 5211-5218.

[13] Y. Pan, T. R. Wei, C. F. Wu, J. F. Li, J. Mater. Chem. C 3(40) (2015) 10583-10589.

[14] W. E. Bies, R. J. Radtke, H. Ehrenreich, E. Runge, Phys. Rev. B 65 (2002) 085208.

[15] X. D. Liu, Y. H. Park, Mater. Trans. 43 (2003) 681.

[16] T. S. Kim, I. S. Kim, T. K. Kim, S. J. Hong, B. S. Chun, Mater. Sci. Eng. B 90 (2002) 42-46.

[17] S. Miura, Doctoral dissertation, Tohoku University, (2000) 31.

**Chapter 4 Formation of Te-rich phase and its effect on microstructure and thermoelectric properties of hot-extruded Bi-Te-Se bulk materials**

**4.1 Introduction**

In Chapters 2 and 3, a Te-rich phase was firstly found in the extruded samples. So far, there have been several reports related to formation of the Te-rich phase [1-5]. Most of them described that the Te-rich phase existed in the ingots grown by zone melting or Bridgman method. Yim et al. [1] indicated that a Te-rich phase resulting from eutectic reaction was distributed along the grain boundaries with a lamellar structure. A similar lamellar microstructure of Te-rich phase was also found by Yamashita et al. [2]. However, Custódio et al. [3] reported that the Te-rich phase exhibited different distribution morphologies with an undefined microstructure. Ha et al. [4] found that the distribution of Te-rich phase corresponded to the growth speed of the ingots, where the Te-rich phase appeared over the entire ingot grown at rapid speed, but it only presented near the end of the solidified part at a slow growth speed. All these reports attributed the Te-rich phase to a product of the eutectic reaction. On the other hand, Hamachiyo et al. [5] observed many pores in their samples fabricated by MA and hot-pressing technique. They explained this phenomenon as a result of the sublimation of Te during hot pressing.

Hence, the formation and distribution of Te-rich phase as well as its effect on microstructure and thermoelectric properties are not well understood. Moreover, so far, no detailed research on Te-rich phase in hot-extruded products has been reported. On the other hand, because of the formation of Te-rich phase, the Te content in the matrix should be reduced relative to the nominal composition. In order to compensate the loss of Te, excessive amount of Te was incorporated in this study, considering high dependence of thermoelectric performance on stoichiometric ratios of Bi, Te and Se [6, 7].

Thus, this chapter focuses on the formation and distribution of Te-rich phase as well as its effect on microstructure and thermoelectric properties of the hot-extruded

Bi-Te-Se bulk materials.

## 4.2 Experimental and procedure

4.2.1 Sample preparation

High purity Bi, Te, and Se powders (>99.9% purity) were used as the starting materials. The powders with nominal compositions of $Bi_2Te_{2.85+x}Se_{0.15}$ (x=0-0.15) were pre-mixed in a mortar and pestle, and then mechanically alloyed under 200 rpm for 12 h in a purified argon atmosphere using a planetary ball milling system. Subsequently, the MAed powders were pressed into a cylindrical green compact (30 mm in diameter and 25 mm in height) by uniaxial pressing, and used as an extrusion billet. Hot extrusion was performed in a temperature range of 340-450°C with an extrusion ratio of 25:1 at a punch speed of 1 mm/min.

4.2.2 Characterization

Microstructural observation and compositional analysis were conducted by scanning electron microscopy (SEM) and energy dispersive X-ray spectroscopy (EDS), respectively. Differential scanning calorimetry (DSC) analysis was carried out in a purified argon atmosphere at heating/cooling rates of $10^{o}$C/min and $2^{o}$C/min. Phase identification was performed by X-ray diffraction (XRD) with Cu Kα radiation. The orientation degree was determined using the Lotgering method [8]. Orientation imaging microscopy (OIM) analysis was performed using an SEM equipped with an electron backscattered diffraction (EBSD) system.

The electron transport properties were evaluated by a Hall effect measurement system (TOYO Corp., Resi Test 8300). The Seebeck coefficient and electrical resistivity of the samples were simultaneously measured by static DC method and four-probe method, respectively, using a thermoelectric property test apparatus (ULVAC-RIKO, ZEM-3). The thermal conductivity was measured by laser flash method (NETZSCH, LFA457 Micro Flash). In the thermal conductivity measurements, the direction of the heat flux was set to the extrusion direction. The dimensionless figure of merit of the samples was calculated by the equation of

$ZT=\alpha^2 T/(\rho\kappa)$. Details of the evaluation methods have been described in section 2.2.4.

## 4.3 Results and discussion

4.3.1 Formation and distribution of Te-rich phase

Fig. 4.1 shows the SEM images (backscattered electron (BE) mode) of the extruded samples on their longitudinal sections, which are parallel to the extrusion direction. Some dark regions with different sizes and distributions are observed in all the extruded samples, which have been confirmed by EDS as a Te-rich phase, just as described in chapter 3. As shown in Fig. 4.1, small-sized Te-rich phase was distributed discretely in the matrix in both samples extruded at 340$^{o}$C and 360$^{o}$C. At temperatures above 400$^{o}$C, in addition to discrete small-sized Te-rich phase, large-sized Te-rich phase was distributed along the extrusion direction (ED) and massively agglomerated in the samples extruded at 400$^{o}$C and 450$^{o}$C, respectively.
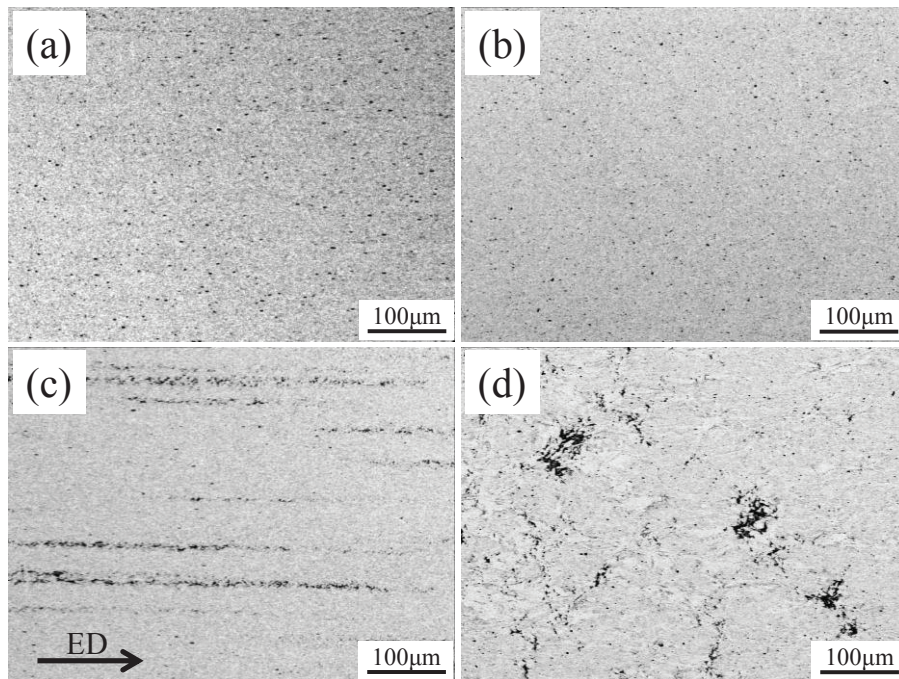


Fig. 4.1 SEM images (backscattered electron mode) of the samples extruded at (a) 340$^{o}$C, (b) 360$^{o}$C, (c) 400$^{o}$C, and (d) 450$^{o}$C.

In order to clarify the difference in distribution of the Te-rich phase at different extrusion temperatures, the compositional analyses of Te in the Te-rich phase and

matrix were carried out using EDS quantitative analysis. Fig. 4.2 shows the dependence of Te content in the Te-rich phase and matrix on extrusion temperature. It was found that the Te content was highly different, depending on the extrusion temperature. The Te contents in the Te-rich phase in the samples extruded at $340^{\circ}$C and $360^{\circ}$C were about 70 at%, whereas those in the samples extruded at $400^{\circ}$C and $450^{\circ}$C were close to 100 at%. On the other hand, the Te content in the matrix was lower than the nominal composition of Te (57 at%) in $Bi_2Te_{2.85}Se_{0.15}$, and it gradually decreased with increasing the extrusion temperature. The formation of smaller Te-rich phase is attributed to the sublimation of Te from the matrix during the hot extrusion due to a high vapor pressure of Te [9], while the larger Te-rich phase is likely to result from the eutectic reaction as reported by Yim et al. [1].
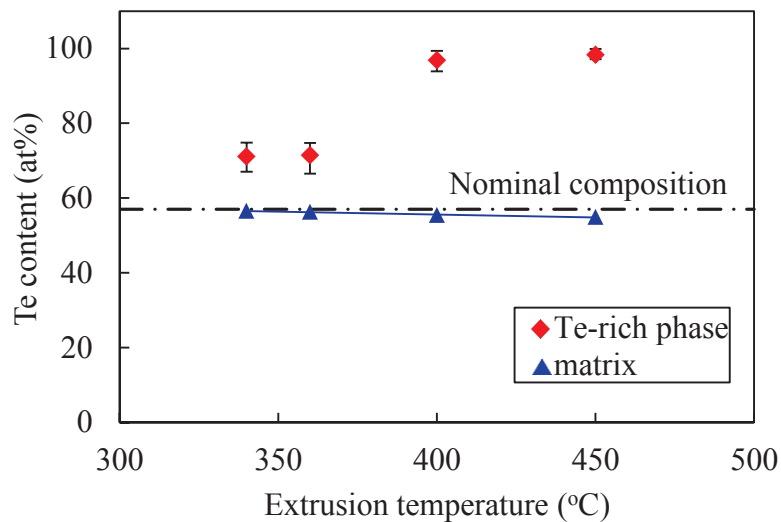


Fig. 4.2 Dependence of Te content in Te-rich phase and matrix on extrusion temperature.

DSC measurements for MAed powder with a composition of $Bi_2Te_{2.85}Se_{0.15}$ were carried out to confirm occurrence of the eutectic reaction. Fig. 4.3 shows the DSC curves of the MAed powder, measured by using different heating/cooling rates. At $10^{\circ}$C/min (curve (a) in Fig. 4.3), an endothermic peak "1" at $417^{\circ}$C and an exothermic peak "2" at $396^{\circ}$C are present in the heating and cooling stages, respectively. Similar endothermic and exothermic peaks ("4" and "5" at $416^{\circ}$C and $399^{\circ}$C, respectively) are also observed at $2^{\circ}$C/min (curve (b) in Fig. 4.3). It is believed that these endothermic

and exothermic peaks correspond to the melting of small amount of MAed powder with a nominal composition $Bi_2Te_{2.85}Se_{0.15}$ and eutectic reaction, respectively. It is noted that there is a temperature difference between the endothermic and exothermic peaks ($\Delta T = T_{end} - T_{exo}$) due to overheating and undercooling during heating and cooling stages, respectively. For example, $\Delta T = 21^{o}C$ at the rate of $10^{o}C$/min. In comparison with the curves (a) and (b), when a smaller heating/cooling rate was used, $T_{end}$ and $T_{exo}$ were shifted to lower and higher temperatures, respectively, *i.e.*, $\Delta T$ was reduced. In addition, as shown in Fig. 4.3, there exists a small exothermic peak "3" at $372^{o}C$ in the heating stage at a heating rate of $10^{o}C$/min, but it does not appear at $2^{o}C$/min. This is likely to be associated with further alloying or structural relaxation of the milled powder.
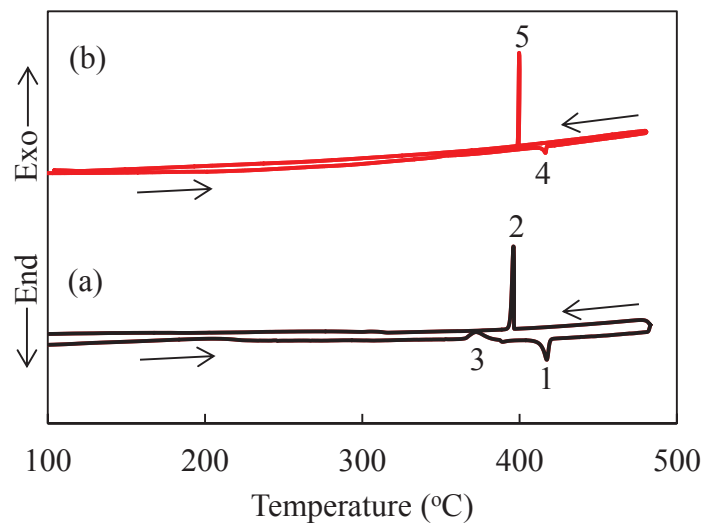


Fig. 4.3 DSC curves of the MA powder at heating/cooling rates of (a) $10^{o}C$/min and (b) $2^{o}C$/min.

Fig. 4.4(a) shows an SEM image (BE) with a magnification higher than Fig. 4.1(d) for the sample extruded at $450^{o}C$. It can be seen from this image that there exist white, light gray, and dark gray regions. Different contrasts in the image are mainly related to the mean atomic number of each region. EDS analyses have demonstrated that the dark gray and white regions corresponded to Te-rich phase and Bi-Te-Se compound with the nominal composition, respectively. As mentioned above, large-sized Te-rich phase is attributed to the eutectic reaction, whereas small-sized Te-rich phase is

associated with the sublimation of Te. It should be pointed out that some small dark points correspond to pores remained in the sample after hot extrusion, which is difficult to be distinguished from small-sized Te-rich phase. Concurrent with the sublimation of Te and formation of small-sized Te-rich phase, a Te-poor phase with light gray contrast appears at original positions in the matrix.

Fig. 4.4(b) shows an example revealing the morphology of large-sized Te-rich phase formed by the eutectic reaction. The dark regions correspond to the Te-rich phase, in which Bi-Te-Se compound with a contrast almost the same as the matrix is distributed, showing a eutectic microstructural feature. Fig. 4.4(c) shows an OIM map with the same area as Fig. 4.4(b). Different colors in Fig. 4.4(c) represent the difference in confidence index (CI), which is determined by the crystal structure of Bi-Te-Se compound. It should be noted that the structure of Te-rich phase is undefined. In comparison with Figs. 4.4(b) and (c), the regions with a low CI value correspond to the Te-rich phase.
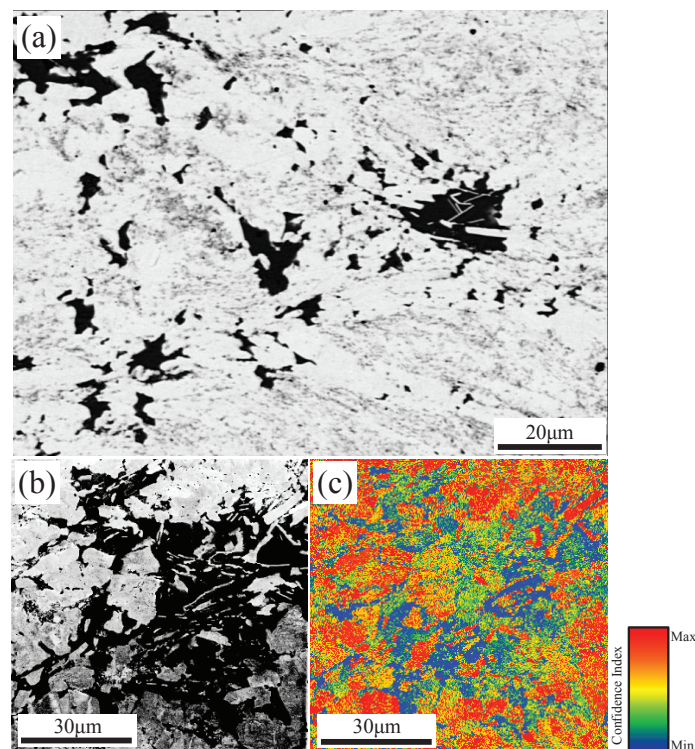


Fig. 4.4 (a) and (b) SEM images and (c) OIM map of the sample extruded at 450$^{\circ}$C.

Fig. 4.5 shows the OIM maps of the extruded samples, exhibiting the distribution

of small-sized Te-rich phase. Due to the significant sublimation of Te at higher extrusion temperatures, the size and amount of the Te-rich phase increased with increasing the extrusion temperature. In addition, it seems that the Te-rich phase is distributed around the grain boundaries, which has also been reported by Yim et al. [1].
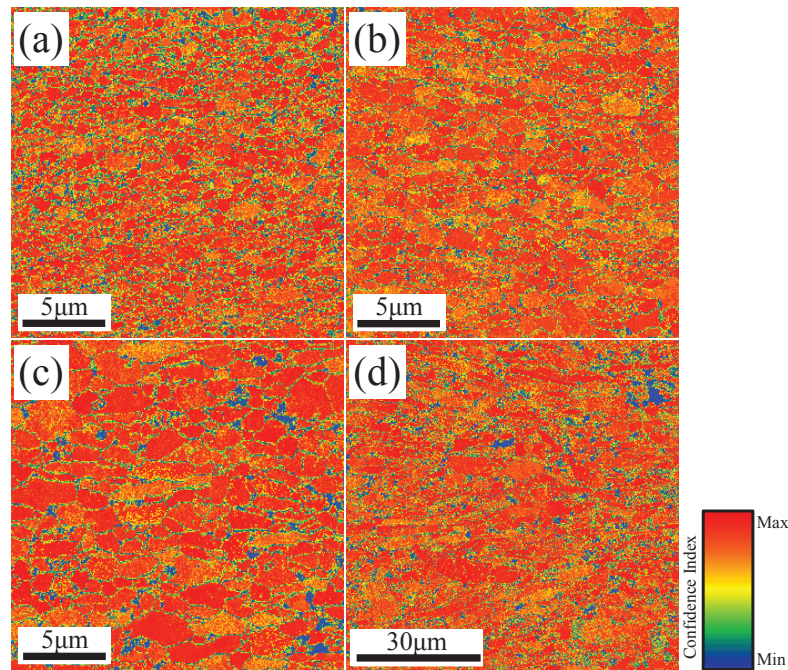


Fig. 4.5 OIM maps of the samples extruded at (a) 340$^{\circ}$C, (b) 360$^{\circ}$C, (c) 400$^{\circ}$C, and (d) 450$^{\circ}$C.

The above results indicate that the formation and distribution of the Te-rich phase are mainly attributed to two different mechanisms: sublimation and eutectic reaction. The former occurs at any extrusion temperature and leads to formation of small-sized Te-rich phase, while the latter occurs at ≥400$^{\circ}$C and the resultant Te-rich phase possesses large sizes. At an extrusion temperature of 400$^{\circ}$C, it is clear that this temperature is close to the eutectic temperature from the DSC results shown in (Fig. 4.3). Moreover, the practical temperature in some areas of the extrusion billet may be slightly higher than the setting temperature of 400$^{\circ}$C, resulting in formation of some liquid phase inside the billet. As the extrusion proceeds, when the billet starts to enter the extrusion die, where the temperature is slightly lower because the bottom of the extrusion die is exposed in air, the eutectic reaction occurs immediately before the

extrusion. The resultant Te-rich phase is subjected to shear deformation during subsequent extrusion, and thus resulting in the distribution of Te-rich phase along the extrusion direction, as shown in Fig. 4.1(c).

At $450^{\circ}$C, when the sample is extruded out of the die, its temperature is still much higher than the eutectic temperature and hence the liquid phase remains in the extruded sample. The eutectic reaction does not take place until the temperature of the extruded sample is reduced to the eutectic temperature during the cooling stage after the extrusion. Due to lack of shear deformation, the Te-rich phase shows a massively agglomerated morphology.

4.3.2 Effect of excessive Te addition on microstructure

Because of the formation of Te-rich phase in the extruded samples, the Te content in the matrix was reduced relative to the nominal composition (Fig. 4.2). In order to compensate the loss of Te, excessive amount of Te was incorporated. The powders with compositions of $Bi_2Te_{2.85+x}Se_{0.15}$ (x=0.05-0.15) were prepared by MA and then hot-extruded at $400^{\circ}$C. The compositional analysis was conducted by EDS and the results are shown in Fig. 4.6. The measured Te content in the matrix increased slightly with increasing the amount of excessive Te added. As Te content increased, the difference between the experimental and nominal compositions became large. These results suggest that the incorporation of excessive amount of Te does not compensate the loss of Te content due to sublimation and/or eutectic reaction. On the contrary, it seems that much more Te-rich phase is formed.
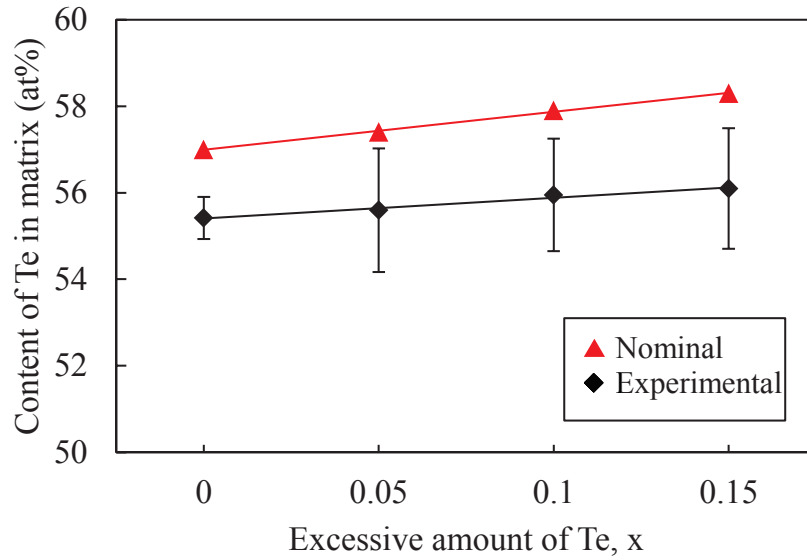
Fig. 4.6 Dependence of measured Te content in the matrix on excessive amount of Te added.

Fig. 4.7 illustrates the XRD patterns of the extruded samples with different amounts of excessive Te. All the patterns of the samples with excessive Te addition are similar to that without excessive Te addition. The main peaks relate to $Bi_2Te_{2.85}Se_{0.15}$ phase, but an impurity phase of $Bi_2O_3$ was detected in all the hot-extruded samples. This bismuth oxide was also found in MA/SPS samples reported by Zhao et al. [10]. They explained that the formation of $Bi_2O_3$ is associated with the oxidation of extra Bi after Te is vaporized. It seems that the situation is suitable for the hot-extrusion process in this study. When excessive amount of Te was incorporated, the peak intensity of $Bi_2O_3$ phase was higher than that in the samples without excessive Te addition (Fig. 4.7). This may be attributed to formation of more Te-rich phase, which causes formation of much more extra Bi, and thus results in the increase in peak intensity of $Bi_2O_3$.
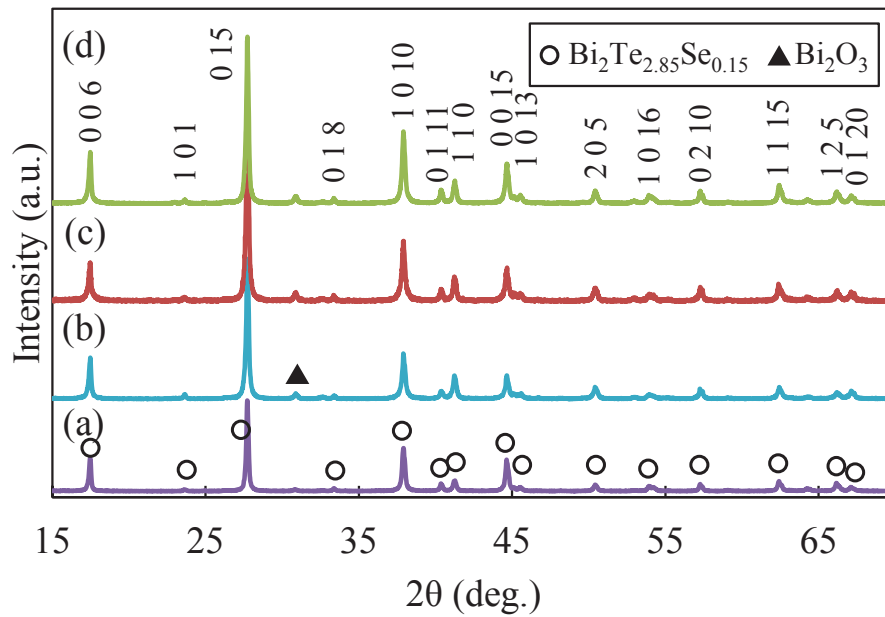
Fig. 4.7 XRD patterns of extruded $Bi_2Te_{2.85+x}Se_{0.15}$ samples with (a) x=0, (b) x=0.05, (c) x=0.10, and (d) x=0.15.

Fig. 4.8 shows the OIM maps on the longitudinal sections of the $Bi_2Te_{2.85+x}Se_{0.15}$ samples extruded at 400°C. As a reference, the map of $Bi_2Te_{2.85}Se_{0.15}$ with x=0 (Fig. 3.9(b)) is also included. Similar refined and equiaxed microstructures are observed for all the extruded samples with different amounts of excessive Te. The average grain sizes were measured as 0.75 μm, 0.60 μm, 0.59 μm, and 0.60 μm for x=0, 0.05, 0.10, and 0.15, respectively. When excessive Te was incorporated, the grain size obviously decreased. This may be associated with the existence of small-sized Te-rich phase, which inhibits the migration of grain boundaries via pinning effect.
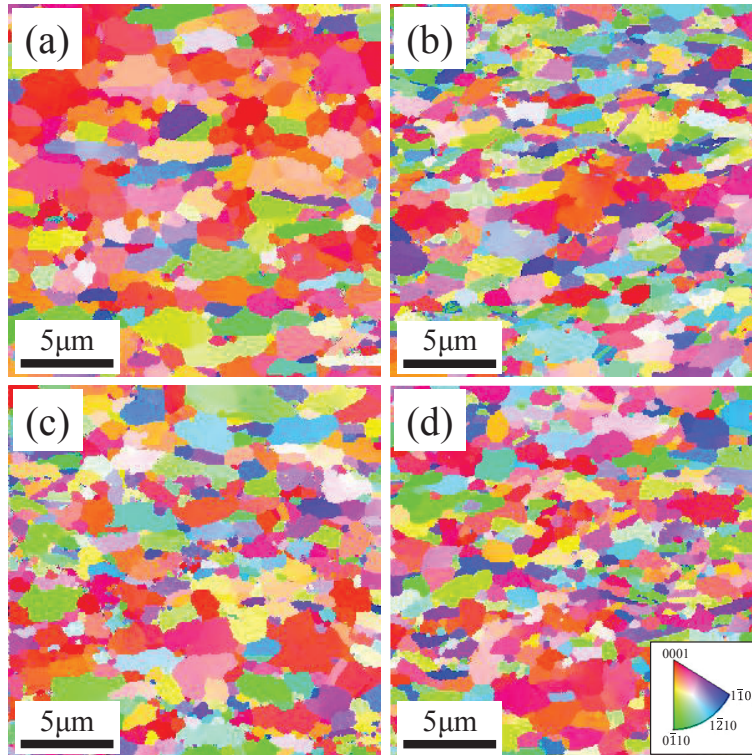
Fig. 4.8 OIM maps of extruded $Bi_2Te_{2.85+x}Se_{0.15}$ samples with (a) x=0, (b) x=0.05, (c) x=0.10, and (d) x=0.15.

As shown in Fig. 4.8, all the extruded samples with excessive Te addition exhibited a preferential orientation of (0 0 0 1). In order to further understand the effect of excessive Te addition on grain orientation, quantified orientation degree was calculated from the XRD patterns (Fig. 4.7) using the Lotgering method. Fig. 4.9 shows the dependence of orientation factor $f_{(00l)}$ on excessive amount of Te. The result exhibits that the orientation degree tends to decrease with increasing excessive amount of Te. This is also attributed to the formation of more Te-rich phase, which inhibits the grain rotation and hence causes a reduction in orientation degree. It should be pointed out that some errors may occur in calculation of the orientation factors from the XRD data shown in Fig. 4.7 due to the existence of $Bi_2O_3$ peaks. Nevertheless, the intensity of the oxide peaks is weak enough to be ignored during the calculation of orientation factor.
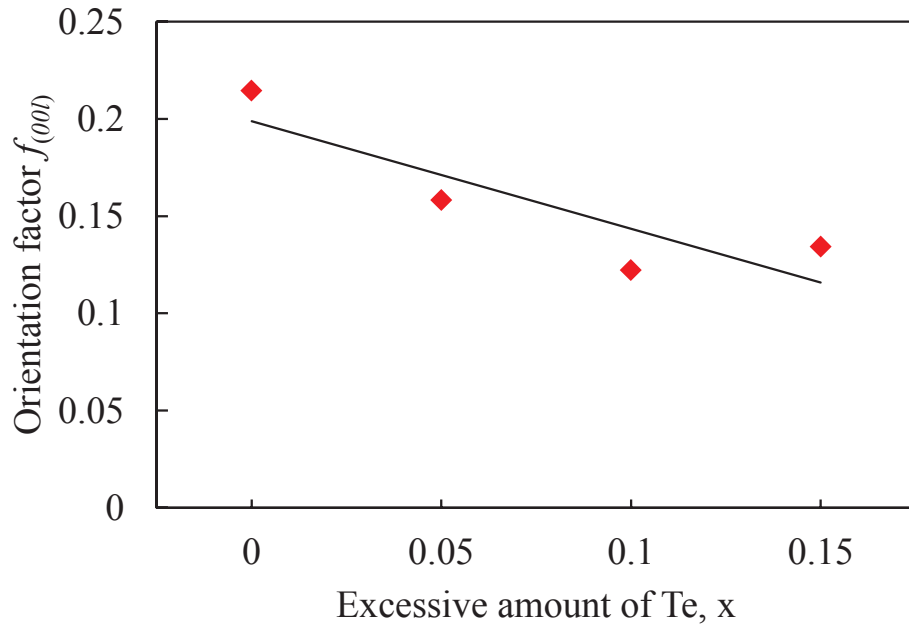
Fig. 4.9 Dependence of orientation factor $f_{(00l)}$ on excessive amount of Te.

### 4.3.3 Effect of excessive Te addition on thermoelectric properties

Fig. 4.10 shows the dependence of the electron transport properties on excessive amount of Te. As the excessive amount of Te increased, the carrier concentration increased, while the mobility decreased.
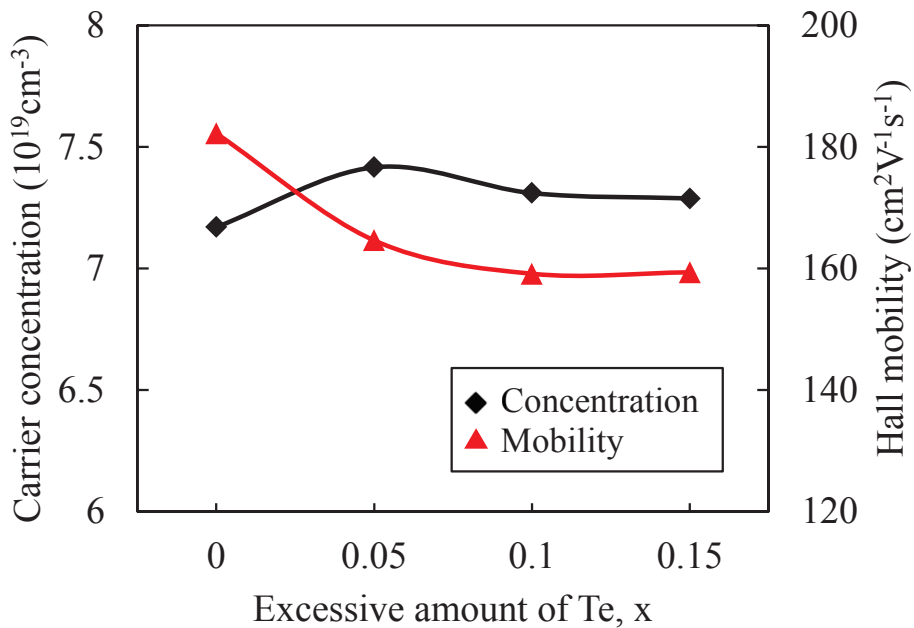


Fig. 4.10 Dependence of electron transport properties on excessive amount of Te.

In Chapter 3, it has been demonstrated that the evaporation of each Te results in formation of one Te vacancy $[V_{Te}]$ with two free electrons $[e]$, which can be expressed by the following equation [11]:

$$Bi_2Te_3 = 2Bi_{Bi}^\times + (3-x)Te_{Te}^\times + xTe(g) \uparrow + xV_{Te}^{2+} + 2xe^- \qquad (4.1)$$

In this work, when excessive amount of Te is incorporated, much more small-sized Te-rich phase is formed due to sublimation of Te, as demonstrated by compositional analysis results shown in Fig. 4.6. This inevitably leads to formation of much more $[V_{Te}]$ and thus the increase in carrier concentration (in the case of x=0.05 in Fig. 4.10). However, the carrier concentration does not increase with further increasing excessive Te, which is likely due to the compensation of Te in the matrix, as shown in Fig. 4.6. In addition, the dangling bonds at grain boundaries as a result of Te deficiencies can also be regarded as fractional-$[V_{Te}]$ resulting in increase of carrier concentration [11]. It is worth noting that Eq. (4.1) describes the point defects in Bi$_2$Te$_3$ binary compound, and the defects at Se-sites are not discussed here due to a small amount of Se. Actually, Se vacancies $[V_{Se}]$ are more easily to be formed because of lower evaporation energy of Se (37.70 kJ/mol) than that of Te (52.55 kJ/mol), and thus provide electrons [12, 13].

On the other hand, in Bi$_2$Te$_3$ compounds, high-energy ball milling can introduce anti-site defects [11, 14, 15] such as $[Bi_{Te}]$, which can also be regarded as doping defects. Liu et al. [11] pointed out that one $[Bi_{Te}]$ anti-site defect donates one hole $[h]$ that contributes to p-type semiconductor. Nevertheless, for n-type Bi-Te-Se compounds examined in the present work, the effect of anti-site defects on transport properties may be small, and Te vacancies $[V_{Te}]$ are believed to be dominant donors.

As shown in Fig. 4.10, the mobility decreased significantly when excessive Te was added, but the change was gradually saturated at x>0.05. This is attributed to smaller grain sizes in the samples with excessive Te addition. Fine grains promote carriers scattering at grain boundaries and thus decrease the mobility. Therefore, similar dependence of the mobility and grain size on excessive amount of Te is obtained. Moreover, the mobility of Bi$_2$Te$_3$-based compounds highly depends on the

orientation degree [16]. The decrease in mobility also corresponds to the reduction in orientation degree.

Fig. 4.11 illustrates the dependence of the Seebeck coefficient and electrical resistivity on excessive amount of Te. The incorporation of excessive Te caused decrease in the level of the Seebeck coefficient. As is well known, the Seebeck coefficient highly depends on carrier concentration, and it can be given by the following equation [17]:

$$\alpha \approx \gamma - ln\,n \tag{4.2}$$

where $\alpha$, $\gamma$, and $n$ are the Seebeck coefficient, the scattering factor, and the carrier concentration, respectively. Therefore, the reduction in the Seebeck coefficient is mainly because of the increased carrier concentration after incorporation of excessive Te.

The electrical resistivity slightly increased with increasing the excessive amount of Te. Electrical resistivity depends on carrier concentration and mobility, and the corresponding relationship can be described by the following equation [17]:

$$\rho = \frac{1}{ne\mu} \tag{4.3}$$

where $\rho$, $e$, and $\mu$ are the electrical resistivity, the electron charge, and the carrier mobility, respectively. As shown in Fig. 4.11, the increased carrier concentration of the samples with excessive Te addition should lead to a reduction in electrical resistivity, while the decreased mobility should cause an increase in electrical resistivity. Therefore, under the interaction of these two contradictory factors, it seems that the reduction in mobility becomes predominant, and thus resulting in an increase in electrical resistivity. Furthermore, the increase in electrical resistivity is also related to the smaller average grain sizes in the samples with excessive Te addition, which increase scattering of carriers.
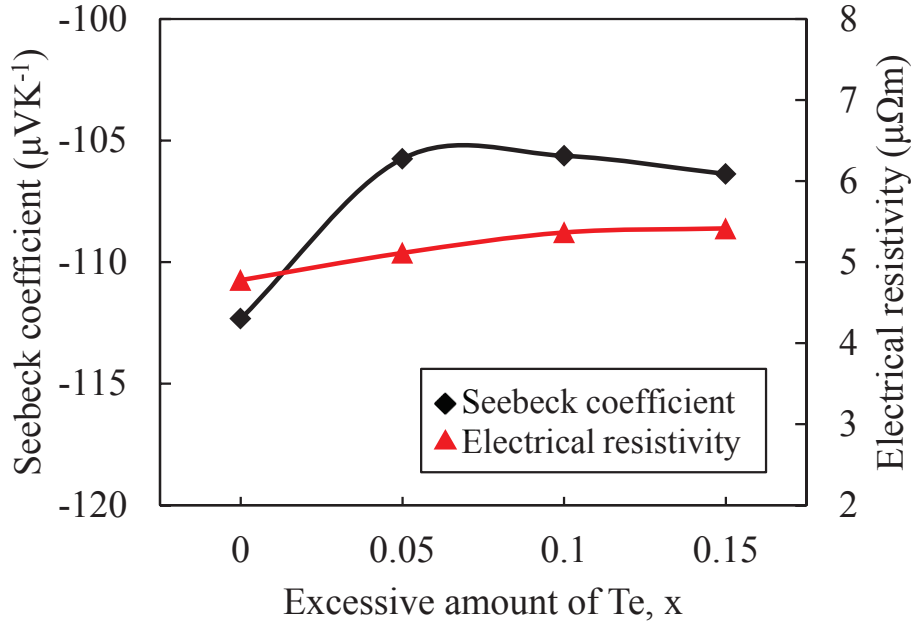
Fig. 4.11 Dependence of the Seebeck coefficient and electrical resistivity on excessive amount of Te.

Fig. 4.12 shows the dependence of thermal conductivity and figure of merit $ZT$ on excessive amount of Te. The thermal conductivity, $\kappa$, is determined by lattice thermal conductivity ($\kappa_{ph}$) and electron thermal conductivity ($\kappa_{el}$) [18]:

$$\kappa = \kappa_{ph} + \kappa_{el} \tag{4.4}$$

The lattice ($\kappa_{ph}$) and electron ($\kappa_{el}$) thermal conductivities are strongly related to the scattering of phonons at grain boundaries and carrier concentration, respectively. The decreased grain sizes in the samples with excessive Te addition should promote the scattering of phonons and thus decrease the thermal conductivity. As shown in Fig. 4.12, however, excessive Te-added samples showed higher values of thermal conductivity compared to the sample with a normal composition (x=0). The increase in thermal conductivity is likely to be associated with the Te-rich phase. It was reported that the Te-rich phase might enhance the thermal conduction by "circulating current" [3, 19, 20], which is developed between the Te-rich phase and matrix, acting as a transport channel for the phonons and promoting thermal conduction. In addition, the increased carrier concentration in the samples with excessive Te addition causes

an increase in $\kappa_{el}$. As a result, the calculated figure of merit $ZT$ decreased significantly after the incorporation of excessive Te.
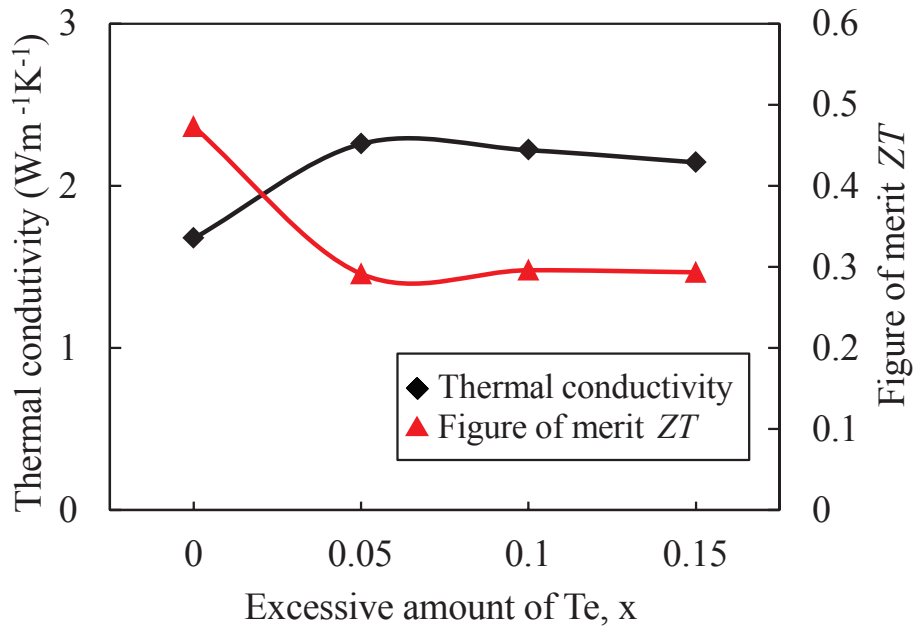


Fig. 4.12 Dependence of thermal conductivity and figure of merit ($ZT$) on excessive amount of Te.

## 4.4 Conclusions

In this chapter, the formation and distribution of Te-rich phase and its effect on microstructure and thermoelectric properties were investigated. Some conclusions of this chapter are summarized as follows.

(1) The formation of Te-rich phase in hot-extruded samples is attributed to two different mechanisms: sublimation of Te and eutectic reaction. The former occurs at any extrusion temperature and leads to formation of small-sized Te-rich phase, while the latter occurs at $\geq 400^{\circ}C$ and the resultant Te-rich phase possesses large sizes.

(2) The small-sized Te-rich phase was distributed discretely around the grain boundaries in extruded samples. The distribution of the Te-rich phase in hot-extruded samples is also related to extrusion temperature. For example, at an extrusion temperature of $400^{\circ}C$, the large-sized Te-rich phase was distributed along the extrusion direction due to shear deformation during the extrusion. At

450$^\text{o}$C, however, the Te-rich phase exhibited a massively agglomerated morphology because the eutectic reaction occurs during the cooling stage after the extrusion and, of course, no shear deformation exists.

(3) The incorporation of excessive amount of Te did not compensate the loss of Te content due to sublimation and/or eutectic reaction. On the contrary, much more Te-rich phase was formed, which resulted in decreases in grain size and orientation degree.

(4) The addition of excessive Te led to increase of carrier concentration and decrease of the mobility, which resulted in significant decrease of the Seebeck coefficient and slight increase of electrical resistivity. In addition, the addition of excessive Te caused an increase of thermal conductivity. As a result, a significant reduction in *ZT* value was found.

## References

[1] W. M. Yim, E. V. Fitzke, F. D. Rosi, J. Mater. Sci. 1(1) (1966) 52-65.

[2] O. Yamashita, S. Tomiyoshi, K. Makita, J. Appl. Phys. 93(1) (2003) 368-374.

[3] M. C. C. Custódio, A. C. Hernandes, J. Cryst. Growth 205(4) (1999) 523-530.

[4] H. P. Ha, Y. W. Cho, J. Y. Byun, J. D. Shim, J. Phys. Chem. Sol. 55(11) (1994) 1233-1238.

[5] T. Hamachiyo, M. Ashida, K. Hasezaki, J. Electron. Mater. 38(7) (2009) 1048-1051.

[6] N. Keawprak, S. Lao-Ubol, C. Eamchotchawalit, Z. M. Sun, J. Alloys Compd. 509(38) (2011) 9296-9301.

[7] L. D. Ivanova, L. I. Petrova, Y. V. Granatkina, V. S. Zemskov, O. B. Sokolov, S. Y . Skipidarov, N. I. Duvankov, Inorg. Mater. 45(2) (2009) 123-128.

[8] F. K. Lotgering, J. Inorg. Chem. 9 (1959) 113-123.

[9] Y. Suga, Thermoelectric semiconductor, Makisyoten, Tokyo, 1966.

[10] L. D. Zhao, B. P. Zhang, W. S. Liu, H. L. Zhang, J. F. Li, J. Alloys Compd. 467 (2009) 91-97.

[11] W. S. Liu, Q. Zhang, Y. Lan, S. Chen, X. Yan, Q. Zhang, H. Wang, D. Z. Wang, G. Chen, Z. F. Ren, Adv. Energy Mater. 1(4) (2011) 577-587.

[12] L. Hu, T. Zhu, X. Liu, X. Zhao, Adv. Funct. Mater. 24(33) (2014) 5211-5218.

[13] Y. Pan, T. R. Wei, C. F. Wu, J. F. Li, J. Mater. Chem. C 3(40) (2015) 10583-10589.

[14] J. Navrátil, Z. Starý, T. Plecháček, Mater. Res. Bull. 31 (1996) 1559-1566.

[15] G.R. Miller, C.Y. Li, J. Phys. Chem. Solids 26 (1965) 173-177.

[16] W. E. Bies, R. J. Radtke, H. Ehrenreich, E. Runge, Phys. Rev. B 65 (2002).085208.

[17] X. D. Liu, Y. H. Park, Mater. Trans. 43 (2003) 681.

[18] T. S. Kim, I. S. Kim, T. K. Kim, S. J. Hong, B. S. Chun, Mater. Sci. Eng. B 90 (2002) 42-46.

[19] S.V. Airapetiants, Soviet Phys.-Tech. Phys. 2 (1957) 429.

[20] G. J. Cosgrove, J. P. Mchugh, W. A. Tiller, J. Appl. Phys. 32 (1961) 621.

# Chapter 5 Effect of Cu-doping on microstructure and thermoelectric properties of Bi-Te-Se bulk materials

## 5.1 Introduction

Since both *p*-type and *n*-type materials are essential for a thermoelectric device, it is important to improve the thermoelectric performance of the *n*-type $Bi_2Te_3$-based compounds, thus many efforts have been done to enhance the *ZT* value. As is well known, doping is an effective method to enhance thermoelectric properties. Cu as one of the best dopants for $Bi_2Te_3$-based compounds has been widely investigated and reported. The effect of Cu addition on the TE properties has been investigated in both single crystals grown by unidirectional solidification methods [1-4] and polycrystals [5-10]. However, the effect of Cu and corresponding mechanism are not well understood, so far. For example, Cui et al. [9] have found an increase in the Seebeck coefficient with increasing Cu content, while the Seebeck coefficient decreases with increasing Cu content as reported by Liu et al. [10]. This may be due to different doping contents and fabrication methods. Moreover, no research work has been conducted on thermoelectric properties of Cu-doped samples fabricated by hot-extrusion technique. Consequently, in this chapter, small amount of Cu was incorporated into *n*-type Bi-Te-Se compounds as a dopant. The purpose is to investigate the effect of Cu-doping on microstructure and thermoelectric properties and find optimal doping content.

## 5.2 Experimental procedure

### 5.2.1 Preparation of alloy powders

High purity Bi (99.99%, 63~106 μm), Se (99.9%, 10 μm), Te (99.99%, 45μm), and Cu (99.99%, 45μm) were used as the starting materials. Bi, Se and Te powders used in this chapter are the same as those used in Chapters 2 and 3. The SEM image of Cu is shown in Fig. 5.1. Cu particles are agglomerated into a needle shape. The starting powders with compositions of $Cu_xBi_2Te_{2.85}Se_{0.15}$ (x=0~0.05) were pre-mixed in a mortar and pestle, and then mechanically alloyed under 200 rpm for 12 h in a

purified argon atmosphere using a planetary ball milling system.
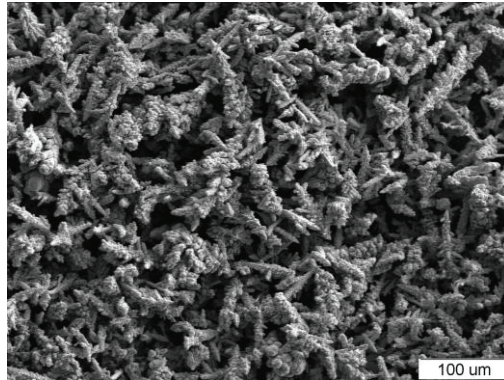


Fig. 5.1 SEM image of Cu powder.

5.2.2 Consolidation by SPS

The MAed powders were firstly consolidated by SPS for optimization of doping conditions. SPS was conducted in a temperature range of 300~400$^o$C under an axial compressive stress of 50 MPa and sintering time of 5 min. The schematic drawing of SPS device is shown in Fig. 5.2.
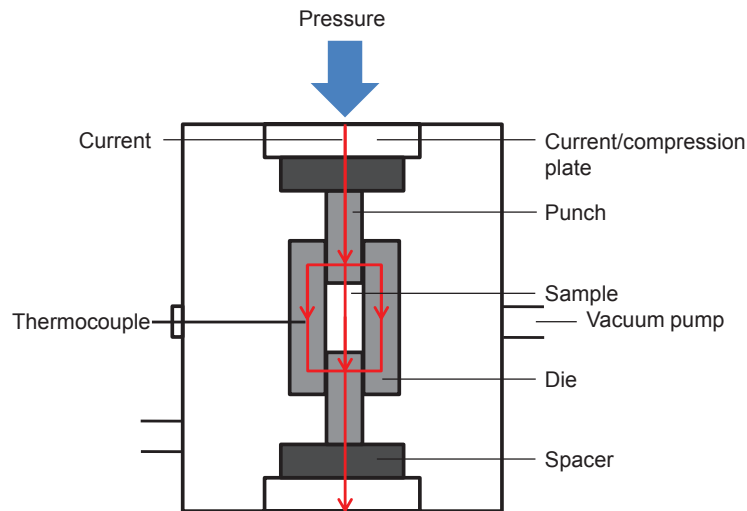


Fig. 5.2 Schematic drawing of SPS device.

5.2.3 Consolidation by hot extrusion

The MAed powders were pressed into a cylindrical green compact at room temperature by uniaxial pressing under 200 MPa and used as a hot-extrusion billet. Hot extrusion was performed at 400°C with an extrusion ratio of 25:1 at a punch

speed of 1 mm/min.

### 5.2.4 Characterization

The density of the extruded samples was determined by the Archimedes method. Phase identification was performed by X-ray diffraction (XRD) with Cu Kα radiation. The orientation degree was determined using the Lotgering method [11]. Microstructural observation and compositional analysis were conducted by scanning electron microscopy (SEM). Composition analysis was carried out by electron probe micro-analyzer (EPMA). Orientation imaging microscopy (OIM) analysis was performed using an SEM equipped with an electron backscattered diffraction (EBSD) system (JEOL, JSM-7001FA). The OIM maps and pole figures were obtained from analysis of the EBSD data by the software TSL-OIM analysis 6.2.

The electron transport properties were evaluated by a Hall effect measurement system (TOYO Corp., Resi Test 8300). The Seebeck coefficient ($\alpha$) and electrical resistivity ($\rho$) of the samples were simultaneously measured by static DC method and four-probe method, respectively, using a thermoelectric property test apparatus (ULVAC-RIKO, ZEM-3). The thermal conductivity ($\kappa$) was measured by laser flash method (NETZSCH, LFA457 Micro Flash). The dimensionless figure of merit of the samples was calculated by the equation of $ZT=\alpha^2 T/(\rho\kappa)$.

The mechanical properties at room temperature were evaluated by the Vickers hardness tests at a load of 1.96 N (Shimadzu, HMV-2000). Details of the evaluation methods have been described in section 2.2.4.

## 5.3 Results and discussion

### 5.3.1 Effect of doping amount on microstructure and thermoelectric properties

Fig. 5.3 shows the XRD patterns of as-mixed and MAed powders with different Cu contents. The peaks of the as-mixed powder consist of Bi, Te, and Se (Fig. 5.2(a)), as expected. After MA, the peaks attributed to the raw powders disappeared and the broadened peaks from $Bi_2Te_{2.85}Se_{0.15}$ phase occurred instead. Due to small amounts of Cu, no peaks derived from Cu were detected in the XRD patterns before and after
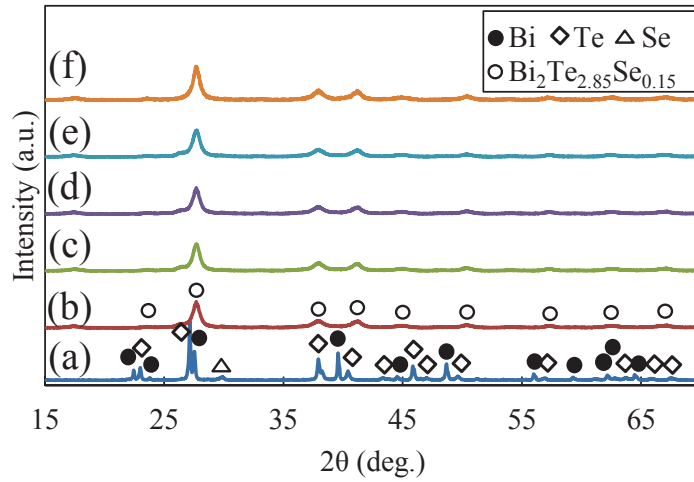
MA.



Fig. 5.3 XRD patterns of (a) as-mixed and (b)-(f) MAed $Cu_xBi_2Te_{2.85}Se_{0.15}$ powders with (a) x=0.01, (b) x=0, (c) x=0.01, (d) x=0.015, (e) x=0.03, and (f) x=0.05.

Fig. 5.4 illustrates the XRD patterns of the samples SPSed at 300°C. All the peaks were attributed to $Bi_2Te_{2.85}Se_{0.15}$ phase and no shift of diffraction angles was found in Cu-doped samples. Similar results were also found in the samples sintered at other temperatures. Furthermore, all the sintered samples exhibited high relative density values of >98%. These results indicate that alloyed and densified $Cu_xBi_2Te_{2.85}Se_{0.15}$ bulk materials can be synthesized through MA and SPS process.



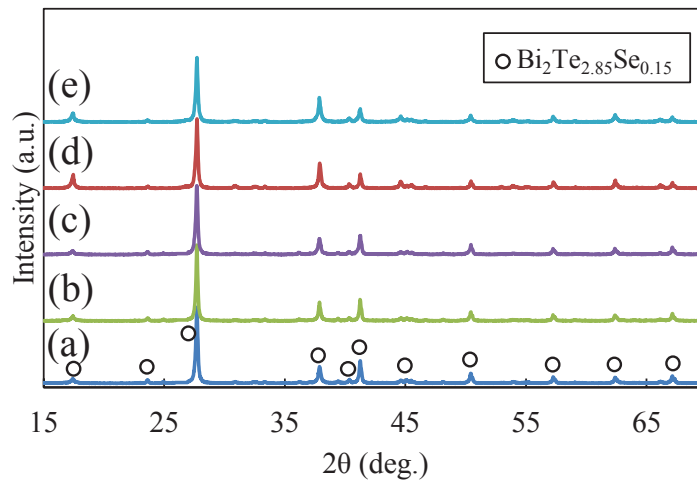Fig. 5.4 XRD patterns of SPSed $Cu_xBi_2Te_{2.85}Se_{0.15}$ samples with (a) x=0, (b) x=0.01, (c) x=0.015, (d) x=0.03, and (e) x=0.05.

Fig. 5.5 shows the EPMA results of the samples SPSed at 300$^o$C. The different colors in the maps represent different composition (CP) levels. From the backscattered electron image (BEI) shown in Fig. 5.5(a), where no Cu was doped, it can be found that there exist some dark regions in the matrix. In comparison with the distribution map of Te, these dark regions can be regarded as a Te-rich phase, which is considered to result from the vaporization or sublimation of Te from $Bi_2Te_{2.85}Se_{0.15}$ matrix due to its high vapor pressure, as revealed in Chapter 4. Bi and Se exhibited homogeneous distributions, as shown in Bi and Se maps. Fig. 5.5(b) illustrates the maps of Cu-doped sample. Although Cu exhibited a low composition level, no severe segregation was observed and the Te-rich phase was still present in the matrix. Similar situations were found in other sintered samples.
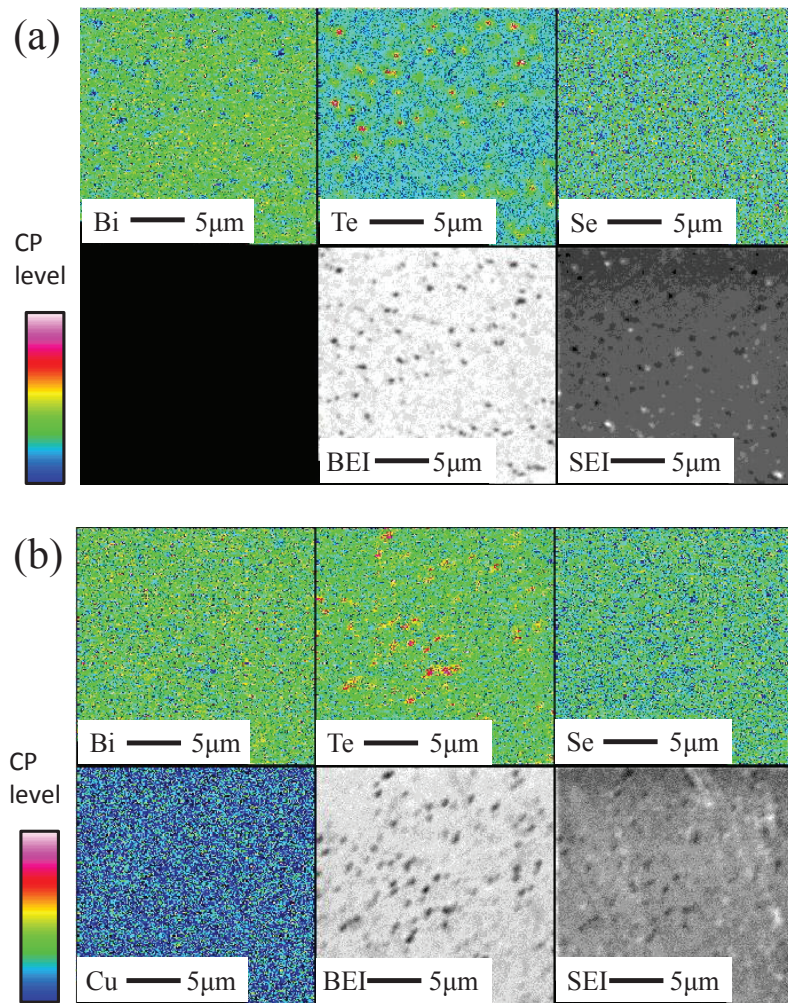


Fig. 5.5 EPMA maps of SPSed $Cu_xBi_2Te_{2.85}Se_{0.15}$ samples with (a) x=0 and (b) x=0.01. BEI: backscattered electron image and SEI: secondary electron image.

Fig. 5.6 shows the OIM maps of the SPSed samples on their cross sections perpendicular to the pressing direction. The sintered samples exhibited fine microstructures with average grain sizes of 0.31 μm and 0.39 μm for the samples SPSed 340°C and 400°C, respectively. Fine-grained microstructures were also observed in the samples SPSed at other sintering temperatures.
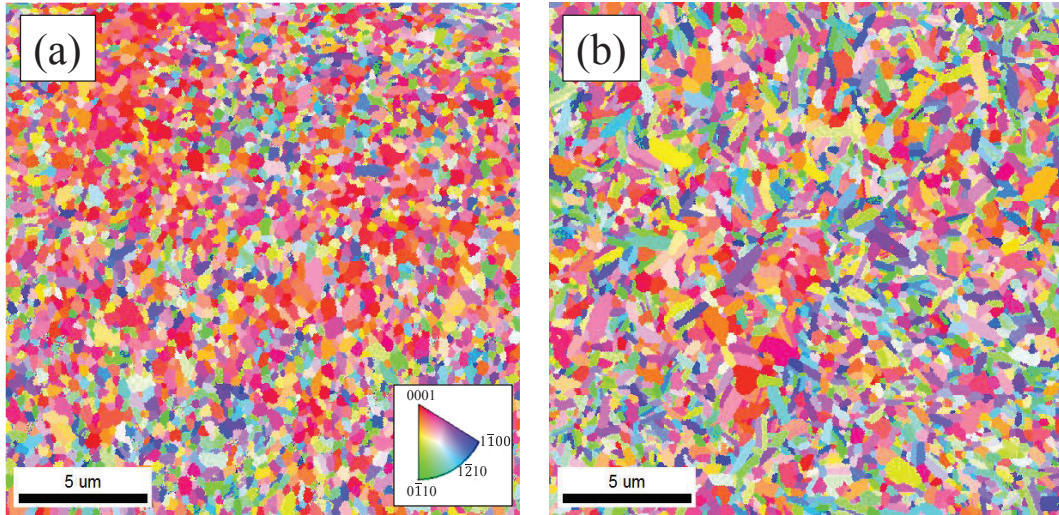


Fig. 5.6 OIM maps of the samples SPSed at (a) 340°C and (b) 400°C.

Fig. 5.7 shows the dependence of carrier concentration on Cu content. The carrier concentration exhibited a significantly decreased tendency with increasing the Cu content at a sintering temperature of 400°C, while there was a small change at 300°C. This result contradicts the common opinion in which Cu acts as a donor of free electrons and should increase carrier concentration. The reason for the reduction of carrier concentration is likely to be related to the mechanical defects, such as Te vacancies [$V_{Te}$], introduced by MA [12, 13]. In Chapter 3, it has been demonstrated that the evaporation of each Te results in formation of one Te vacancy [$V_{Te}$] with two free electrons [$e$], which can be expressed by the following equation [10]:

$$Bi_2Te_3 = 2Bi_{Bi}^{\times} + (3-x)Te_{Te}^{\times} + xTe(g) \uparrow + xV_{Te}^{2+} + 2xe^- \qquad (5.1)$$
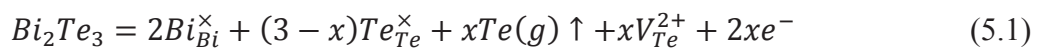
Liu et al. [10] have also pointed out that the formation of [$V_{Te}$] is limited due to the presence of Cu, which results in a reduction of [e], and thus causes decrease in carrier

concentration in this work.

It has been confirmed that the donor-like defects ($[V_{Te}]$) can be reduced by annealing treatment [13, 15]. Consequently, at a higher sintering temperature, fewer defects remain, which causes a shift of the reaction in Eq. (5.1) from the left to the right, resulting in an increase in [e]. Thus, when small amounts of Cu ($x \leq 0.015$) were doped, the carrier concentration exhibited a higher level at $400^{\circ}$C than that at $300^{\circ}$C. As Cu content increases, it seems that the limitation of $[V_{Te}]$ by Cu becomes predominant, which results in significant decrease in carrier concentration at $400^{\circ}$C. The significant reduction at $400^{\circ}$C and small change at $300^{\circ}$C may be possible because the diffusion of Cu occurs easily at a higher temperature.
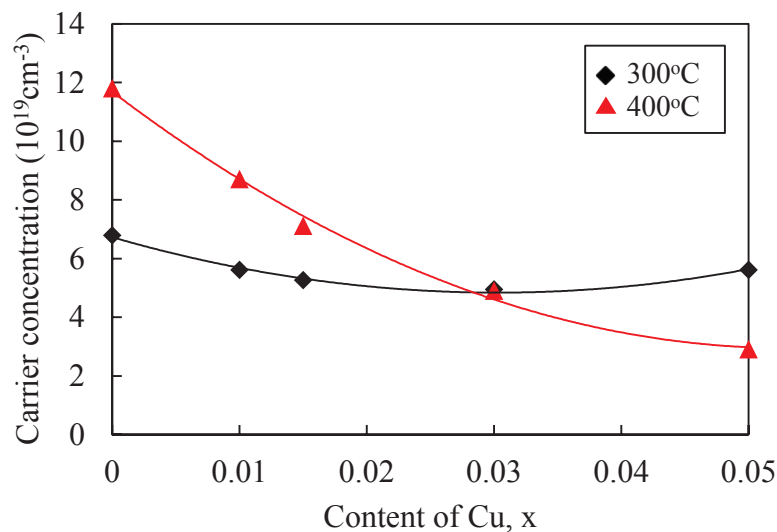


Fig. 5.7 Dependence of carrier concentration on content of Cu.

Fig. 5.8 shows the dependence of mobility on Cu content. The change of mobility at $300^{\circ}$C was still not evident, while the mobility exhibited an increasing tendency at $400^{\circ}$C. The increase in mobility with increasing Cu content at $400^{\circ}$C was also found by Svechnikova et al. [16]. They explained that Cu was placed at the interstitial site between two quintets (Te(1)-Te(1)) and achieved an electrical connection and thus resulted in increase of mobility. The different variations of mobility at different sintering temperature were also attributed to diffusion of Cu.
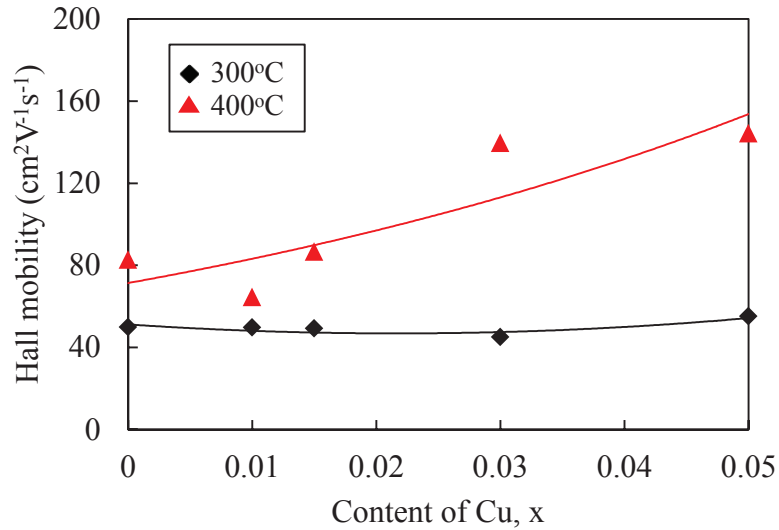
Fig. 5.8 Dependence of mobility on content of Cu.

Fig. 5.9 shows the dependence of the Seebeck coefficient on Cu content. The absolute values of the Seebeck coefficient increased with increasing Cu content. The change was larger at 400°C than that at 300°C. The Seebeck coefficient highly depends on carrier concentration, and it is determined by [17]:

$$\alpha \approx \gamma - lnn \tag{5.2}$$

where $\alpha$, $\gamma$ and $n$ are the Seebeck coefficient, scattering factor, and carrier concentration, respectively. Thus, the variations of the Seebeck coefficient are in good agreement with the results of carrier concentration shown in Fig. 5.7.
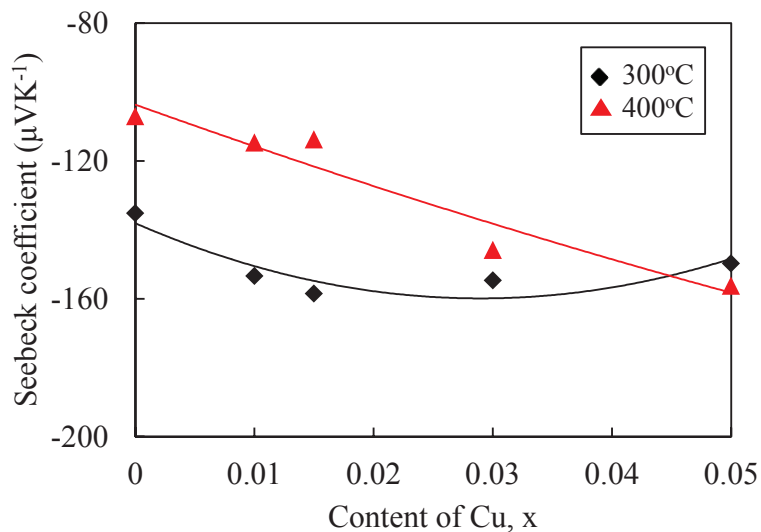


Fig. 5.9 Dependence of the Seebeck coefficient on content of Cu.

Fig. 5.10 shows the dependence of the electrical resistivity on Cu content. It appears that the electrical resistivity does not change significantly with increasing Cu content. However, the electrical resistivity of the sample sintered at 300°C was much higher than that sintered at 400°C. This is mainly because that a lower sintering temperature leads to formation of a fine-grained microstructure, as shown in Fig. 5.6, resulting in increase in scattering of carriers and thus electrical resistivity.
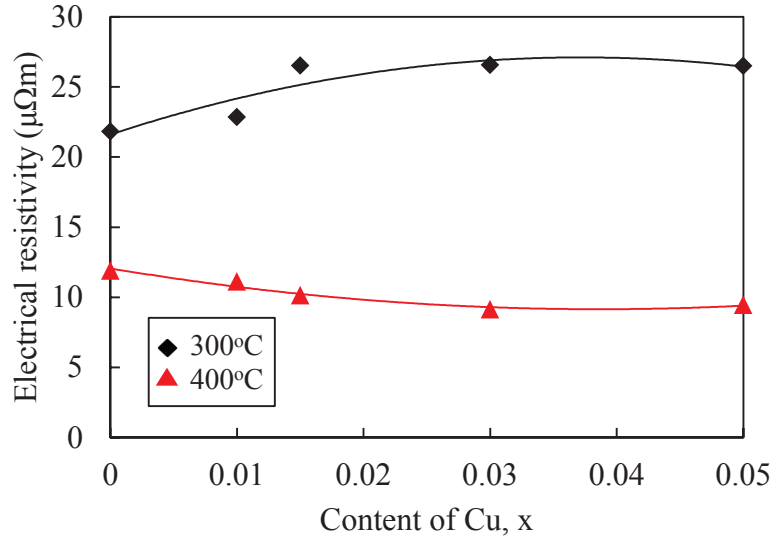


Fig. 5.10 Dependence of the electrical resistivity on content of Cu.

Fig. 5.11 shows the dependence of thermal conductivity on Cu content. A slight decrease of thermal conductivity was found at sintering temperature of 400°C, while almost no change at 300 °C as the Cu content increased. In addition, the samples SPSed at 400°C exhibited higher thermal conductivity than those SPSed at 300°C. Thermal conductivity is related to electron-phonon interaction and it can be expressed according to the following equation [18]:

$$\kappa = \kappa_{ph} + \kappa_{el} \tag{5.3}$$

where $\kappa_{ph}$ and $\kappa_{el}$ are lattice thermal conductivity and electron thermal conductivity, respectively. Higher thermal conductivity at 400°C is due to larger grain sizes at higher sintering temperature, which causes the decrease in phonon scattering from grain boundaries and thus increase in thermal conductivity. The slight decrease with

increasing Cu content is attributed to the decreased carrier concentration and thus decrease in $\kappa_{el}$.
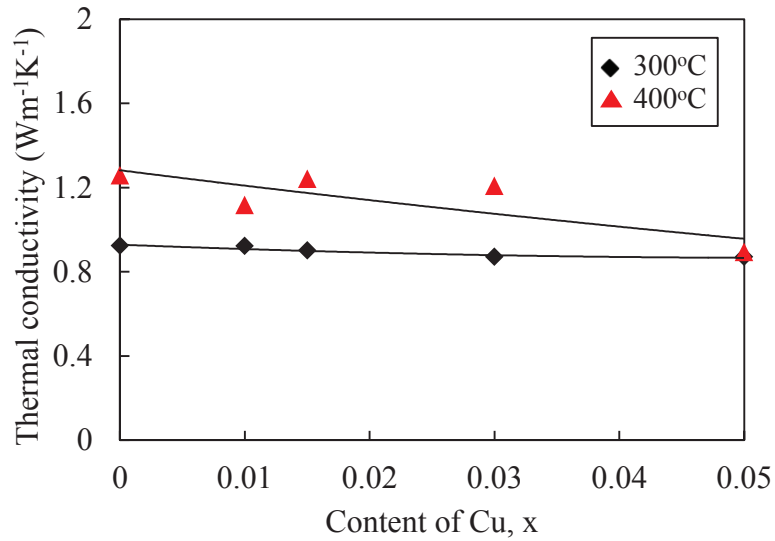


Fig. 5.11 Dependence of thermal conductivity on content of Cu.

Fig. 5.12 shows the dependence of figure of merit $ZT$ on content of Cu. A significant increase of $ZT$ value with increasing Cu content was found at 400$^{\rm o}$C, where the largest $ZT$ value of 0.87 was obtained at room temperature for the sample of $Cu_{0.05}Bi_2Te_{2.85}Se_{0.15}$. However, the $ZT$ values for the samples SPSed at 300$^{\rm o}$C exhibited a lower level and independence on Cu content.
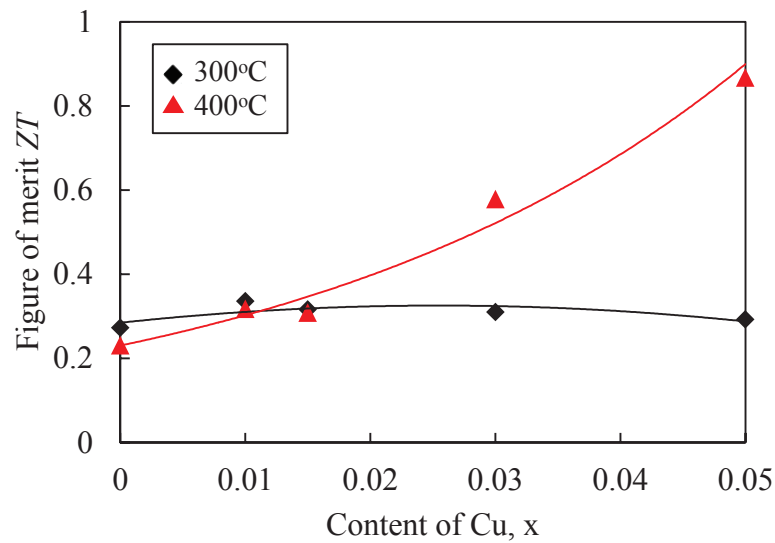


Fig. 5.12 Dependence of figure of merit $ZT$ on content of Cu.

5.3.2 Doping effect in hot-extruded samples

Base on the SPS results, the alloy powders with composition of $Cu_xBi_2Te_{2.85}Se_{0.15}$ (x=0~0.05) was consolidated by hot extrusion at $400^oC$.

Fig. 5.13 shows the extrusion pressure–stroke curves with different Cu contents. The pressure evolution in extrusion process has been discussed in Chapters 2 and 3. It should be noted that, as the Cu content increased, the pressure level decreased. The extruded samples showed sound appearances, as shown in Fig. 5.14, but the relative density was reduced with increasing the Cu content (Fig. 5.15).
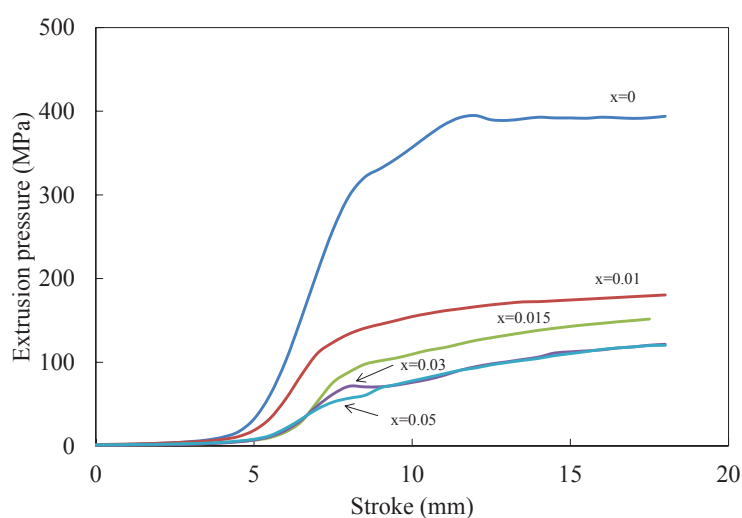


Fig. 5.13 Extrusion pressure–stroke curves with different Cu contents.

Liu et al. [10] pointed out that the lattice parameter $c$ of $Cu_xBi_2Te_{2.7}Se_{0.3}$ compounds increased with increasing Cu content. They attributed this to entrance of Cu atoms into the interstitial site formed by Te(1)-Te(1) (Fig. 1.6), which increased the distance between the weak van der Waals force bounded layers. Therefore, it seems that the reductions of extrusion pressure (Fig. 5.13) and relative density (Fig. 5.15) are related to the intercalation of Cu into Te(1)-Te(1), which contributes to the occurrence of cleavage and increase of unit cell volume. In the further work, transmission electron microscopy (TEM) will be used to analyses the lattice structures of the extruded samples.
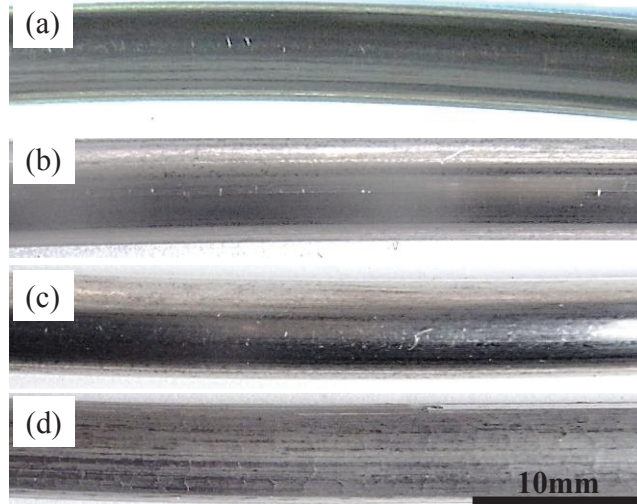
Fig. 5.14 Appearances of the extruded samples with different Cu contents of (a) x=0, (b) x=0.01, (c) x=0.015, and (d) x=0.03.
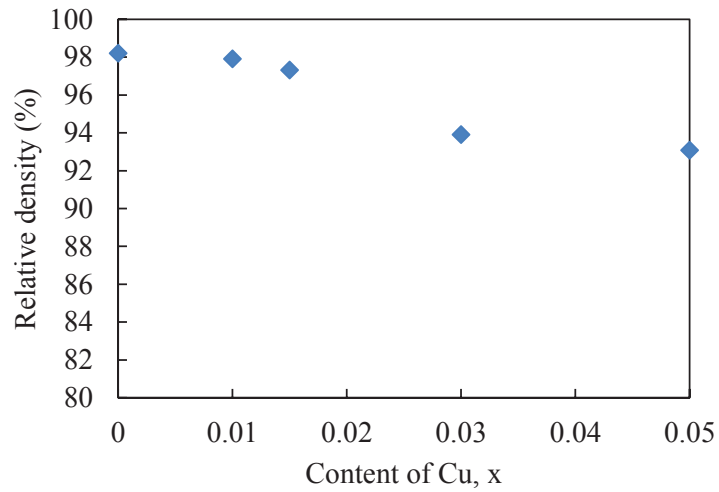


Fig. 5.15 Relative density of the extruded samples with different Cu contents.

Fig. 5.16 shows the XRD patterns of the extruded samples with different Cu contents. All the peaks were attributed to $Bi_2Te_{2.85}Se_{0.15}$ phase and no shift of diffraction angles was found in Cu-doped samples.
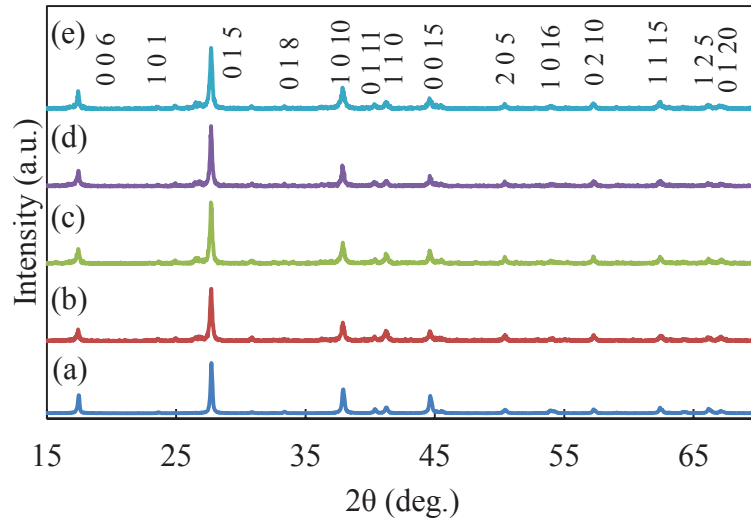
Fig. 5.16 XRD patterns of the extruded samples with different Cu contents of (a) x=0, (b) x=0.01, (c) x=0.015, (d) x=0.03, and (e) x=0.05.

Fig. 5.17 shows the OIM maps on the longitudinal sections of the extruded samples with different Cu contents. Fine and equiaxed grains were observed in the Cu-free sample (Fig. 5.17(a)), while the grains exhibited elongated shapes in the Cu-doped samples. In order to understand the distribution of Cu in $Bi_2Te_{2.85}Se_{0.15}$ extruded samples, Cu phase is highlighted in the OIM maps. Fig. 5.17(f) illustrates an OIM map of $Cu_xBi_2Te_{2.85}Se_{0.15}$ (x=0.01) with a larger magnification, where the small grains belongs to Cu phase. It seems that Cu is distributed around $Bi_2Te_{2.85}Se_{0.15}$ grain boundaries. Thus, the elongated grain shapes may be because that Cu inhibits the migration of grain boundaries via pinning effect during hot extrusion process. The corresponding (0 0 0 1) pole figures are shown in Fig. 5.18. The results indicated that the (0 0 0 1) orientation is still parallel to the extrusion direction in the Cu-doped samples.
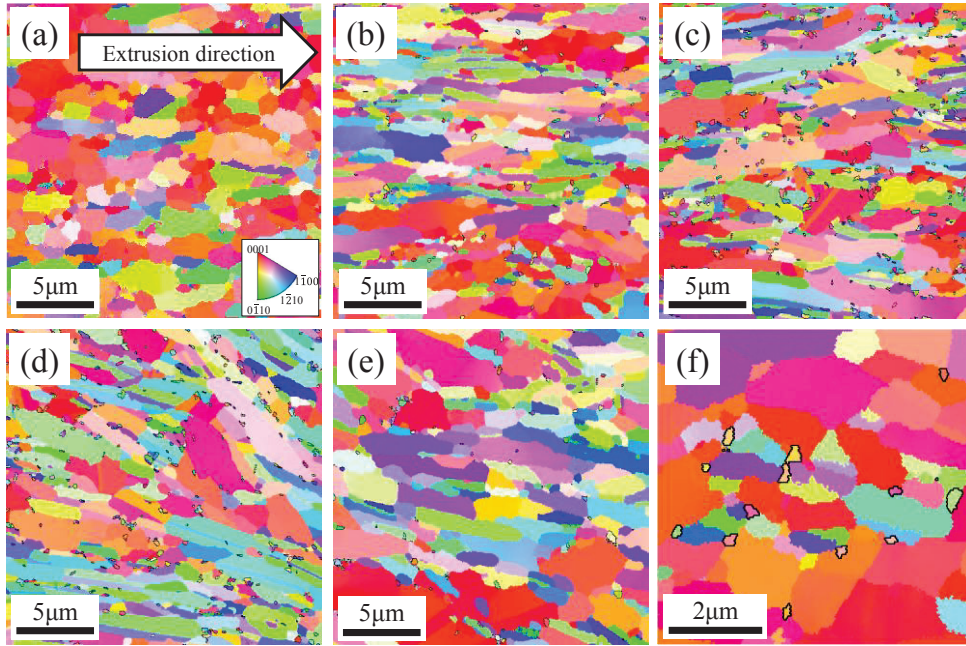
Fig. 5.17 OIM maps of the extruded samples with different Cu contents of (a) x=0, (b) x=0.01, (c) x=0.015, (d) x=0.03, (e) x=0.05, and a higher magnification of (f) x=0.01.
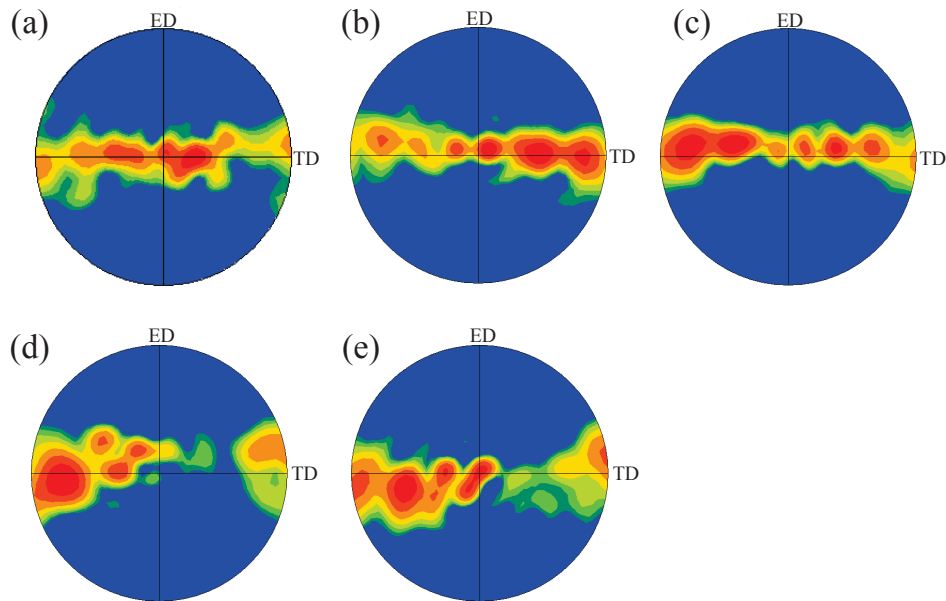


Fig. 5.18 Pole figures of the extruded samples with different Cu contents of (a) x=0, (b) x=0.01, (c) x=0.015, (d) x=0.03, and (e) x=0.05.

Fig. 5.19 shows the dependence of carrier concentration on Cu content. The carrier concentration significantly decreased with increasing the Cu content. The reduction is also attributed to limitation of [$V_{Te}$] by Cu, as described in Fig. 5.7.
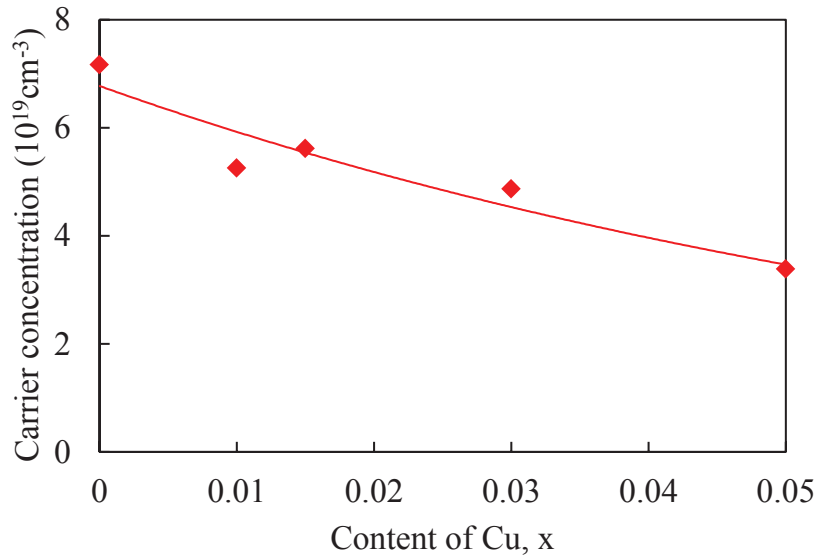
Fig. 5.19 Dependence of carrier concentration on content of Cu.

The mobility of the extruded samples showed a small variation with the increase in Cu content, as shown in Fig. 5.20, which is different with the result of SPSed samples (Fig. 5.8). It has been demonstrated that the intercalation of Cu into Te(1)-Te(1) layers caused increase of mobility for the SPSed samples. However, it is not suitable for hot-extruded samples. Note that, the mobility used for extruded samples is in the directions along the basal planes, because of its anisotropy as described in Chapters 3. Thus, it can be concluded that the effect of Cu on the mobility along the basal planes is weaker than that along *c*-axis.

Fig. 5.20 Dependence of mobility on content of Cu.

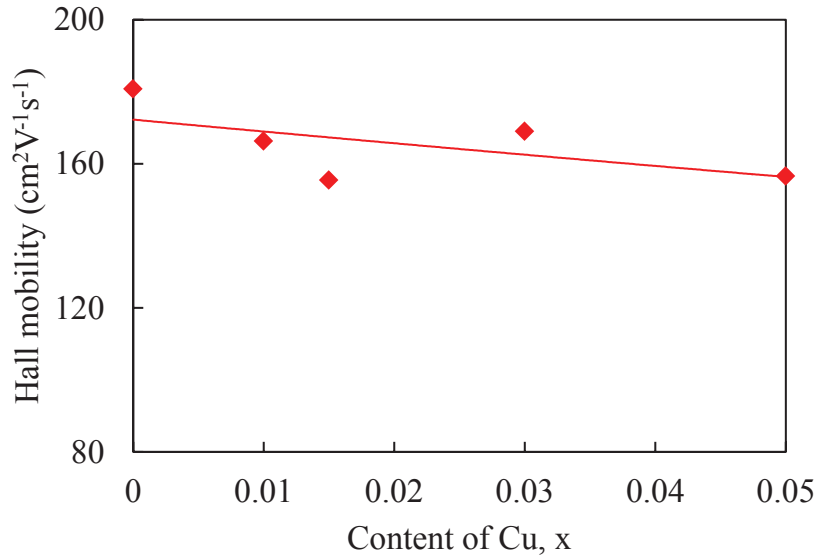Fig. 5.21 shows the dependence of the Seebeck coefficient on Cu content. Due to the reduction of carrier concentration, the corresponding Seebeck coefficient showed a significantly increased tendency with increasing Cu content, while the electrical resistivity increased significantly, as shown in Fig. 5.22.
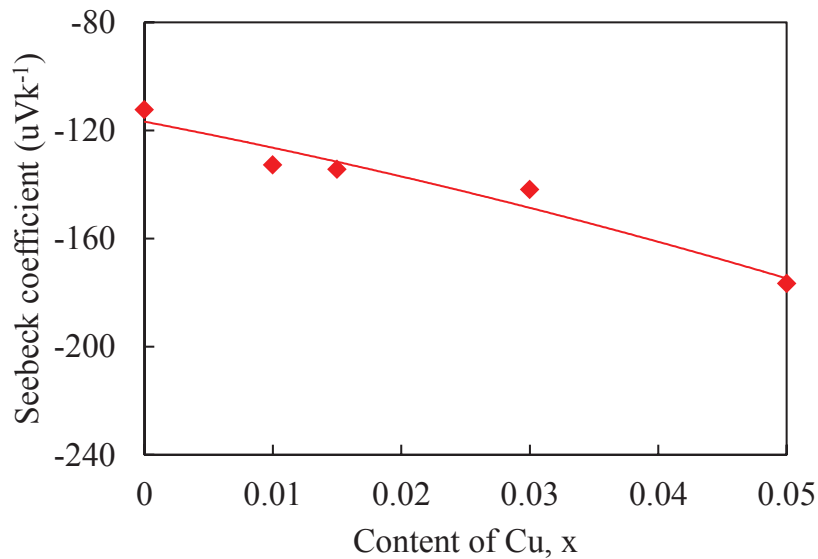


Fig. 5.21 Dependence of the Seebeck coefficient on content of Cu.
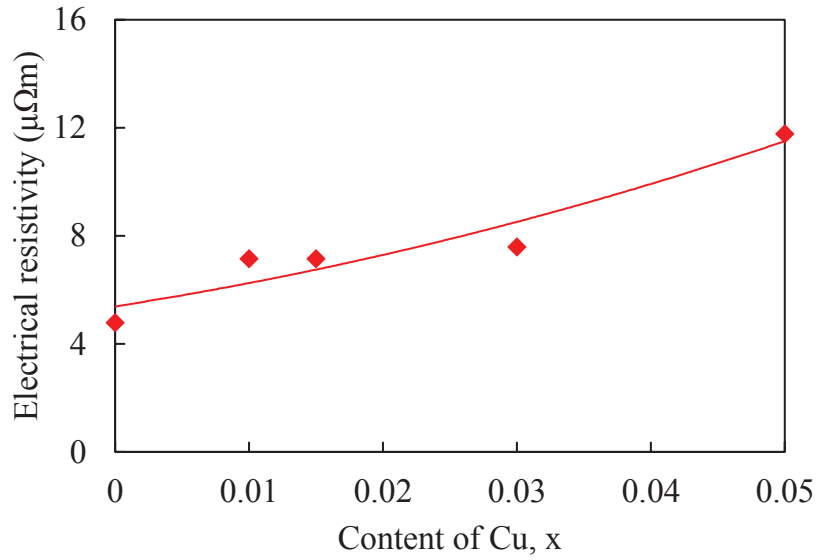
Fig. 5.22 Dependence of the electrical resistivity on content of Cu.

Fig. 5.23 shows the dependence of thermal conductivity on Cu content. Significant decrease in thermal conductivity of the extruded samples was found with increasing Cu content. The reduction is mainly related to the increased carrier concentration. As a result, the calculated *ZT* value exhibited increased tendency as Cu content increased, where the highest *ZT* value of 0.86 was obtained for the sample of $Cu_{0.05}Bi_2Te_{2.85}Se_{0.15}$, as shown in Fig. 5.24.



Fig. 5.23 Dependence of thermal conductivity on Cu content.

Fig. 5.24 Dependence of figure of merit *ZT* on Cu content.

## 5.4 Conclusions

$Cu_xBi_2Te_{2.85}Se_{0.15}$ bulk thermoelectric materials were fabricated by MA/SPS and MA/hot-extrusion techniques. The effect of Cu on microstructure and thermoelectric properties has been studied. Some conclusions of this chapter are summarized as follows.

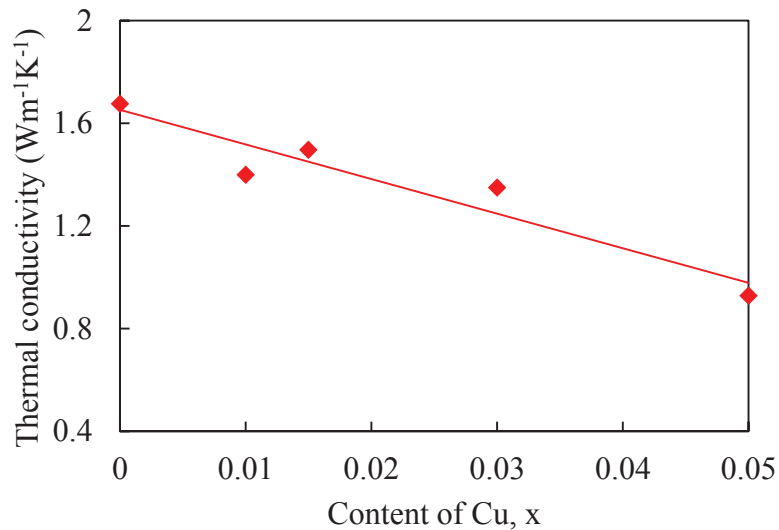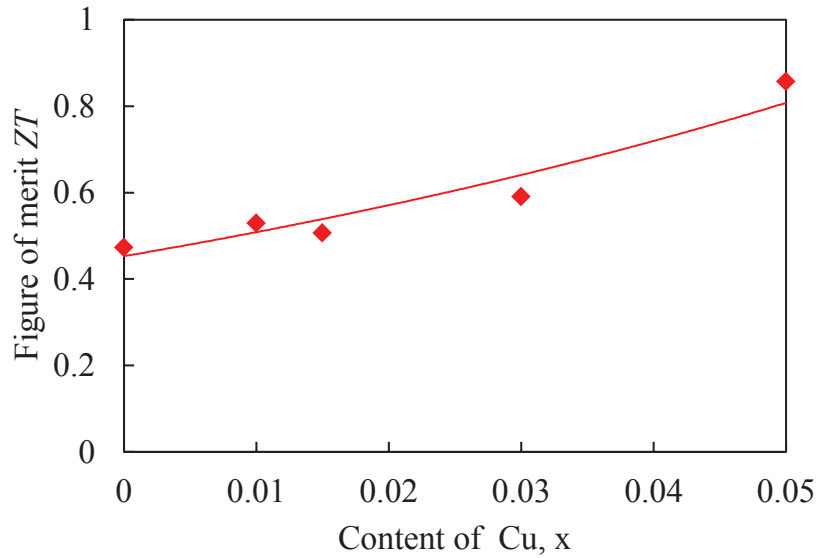(1) All the SPSed samples exhibited high relative density values of >98%. Cu was distributed homogeneously and no severe segregation of Cu was observed. In addition, fine-grained microstructures were observed in the SPSed samples.

(2) At a lower SPS temperature of 300$^o$C, the effect of Cu doping on thermoelectric properties was not evident. At 400$^o$C, the carrier concentration was reduced significantly with increasing Cu content, and thus resulting in a significant increase in the absolute value of the Seebeck coefficient. However, the effect of Cu doping on electrical resistivity and thermal conductivity was not significant. An increase in dimensionless figure of merit *ZT* was found with increasing Cu content. A largest *ZT* value of 0.87 was achieved at room temperature for the $Cu_{0.05}Bi_2Te_{2.85}Se_{0.15}$ sample SPSed at 400°C.

(3) Cu phase was mainly distributed around the grain boundaries of the extruded samples resulting in elongated grain shapes via pinning effect.

(4) The effect of Cu on the mobility along the basal planes is not significant. With increasing Cu contents, the carrier concentration of the extruded samples decreased, resulting in increase of the corresponding Seebeck coefficient and electrical resistivity, but decrease of thermal conductivity. The resultant $ZT$ values of the extruded samples exhibited significant increasing tendency. A largest $ZT$ value of 0.86 was achieved at room temperature for the $Cu_{0.05}Bi_2Te_{2.85}Se_{0.15}$ sample extruded at $400^oC$.

**References**

[1] O. Beckman, P. Bergvall, Arkiv For Fysik, 24(2-3) (1963) 113-122.

[2] T. E. Svechnikova, P. P. Konstatinov, G. T. Alekseeva, Inorg. Mater. 36 (2000) 556.

[3] T. A. McCarthy, H. J. Goldsmid, J. Phys. D Appl. Phys. 3 (1970) 697.

[4] J. Bludska, S. Karamazov, J. Navratil, I. Navratil, I. Jakubec, J. Horak, Solid State Ion. 171 (2004) 251.

[5] J. L. Cui, L. D. Mao, W. Yang, X. B. Xu, D. Y. Chen, W. J. Xiu, J. Solid State Chem. 180 (2007) 3583.

[6] J. L. Cui, J. Alloy. Compd. 415 (2006) 216.

[7] S. Fujimoto, S. Sano, T. Kajitami, J. Alloy. Compd. 443 (2007) 182.

[8] W. S. Liu, Q. Y. Zhang, Y. C. Lan, S. Chen, X. Yan, Q. Zhang, H. Wang, D. Z. Wang, G. Chen, Z. F. Ren, Adv. Energy Mater. 1 (2011) 577.

[9] J. L. Cui, L. D. Mao, et al., J. Solid State Chem. 180(12) (2007) 3583-3587.

[10] W. S. Liu, Q. Zhang, et al., Adv. Energy Mater. 1 (2011) 577.

[11] F. K. Lotgering, J. Inorg. Chem. 9 (1959) 113-123.

[12] J. Navrátil, Z. Starý, et al., Mater. Res. Bull. 31 (1996)1559–1566.

[13] L. D. Zhao, B. P. Zhang, et al., J. Alloys Compd. 467 (2009) 91-97.

[15] J. M. Schultz, J. P. Mchugh, et al., J. Appl. Phys. 33 (1962) 2443.

[16] T. E. Svechnikova, P. P. Konstantinov, et al., Inorg. Mater. 36(6) (2000) 556-560.

[17] X. D. Liu, Y. H. Park, Mater. Trans. 43 (2003) 681.

[18] T. S. Kim, I. S. Kim, et al. Mater. Sci. Eng., B 90 (2002) 42–46.

# Chapter 6: Effect of annealing on microstructure and thermoelectric properties of hot-extruded Bi-Sb-Te bulk materials

## 6.1 Introduction

$P$-type and $n$-type $Bi_2Te_3$-based bulk materials have been successfully fabricated by MA and hot-extrusion technique as described in Chapters 2 and 3, respectively. The extruded samples exhibit excellent mechanical performance, while the corresponding thermoelectric properties still need further improvement. We found that the thermoelectric properties of extruded samples are sensitive to the lattice defects induced by mechanical-deformation during MA and hot-extrusion processes. Recently, there are several investigations on the effects of these defects on thermoelectric properties of $Bi_2Te_3$-based compounds [1-3]. It is found that the lattice defects act as donors, evenly change the semiconductor type. The carrier concentration is highly sensitive to these donor-like defects as demonstrated in Chapters 3 and 4. It is well known that both the Seebeck coefficient and electrical resistivity are related to carrier concentration [4], and the best transport properties can be obtained by optimizing carrier concentration [5]. It has been confirmed that the donor-like defects can be reduced by annealing treatment [6, 7]. Therefore, in this chapter, annealing was conducted to control the lattice defects and thus to optimize the transport properties. The purpose of this chapter is to investigate the effect of annealing on microstructure, thermoelectric and mechanical properties of the extruded $Bi_{0.4}Sb_{1.6}Te_3$ bulk materials.

## 6.2 Experimental procedure

### 6.2.1 Preparation of $Bi_{0.4}Sb_{1.6}Te_3$ extrudates

High purity Bi (99.99%, 63~106 μm), Sb (99.9%, 10 μm), and Te (99.99%, 45μm) powders were used as the starting materials. Firstly, the starting powders with a nominal composition of $Bi_{0.4}Sb_{1.6}Te_3$ were subjected to MA. Then, the MAed powders were uniaxially pressed into a cylindrical green compact used as a billet for hot extrusion. The hot extrusion was performed at 340°C and 400°C with an extrusion

ratio of 25:1 at a punch speed of 1 mm/min. Details of the MA and hot-extrusion are referred as the description in sections 2.2.2. and 2.2.3.

## 6.2.2 Annealing

The extruded samples were subjected to annealing in a super-mini vacuum furnace (MARUSHO SPS100-16V). The conditions of annealing are listed in Table 6.1.

Table 6.1 Conditions of annealing

| | |
|---|---|
| Temperature ($^{o}$C) | 260~400 |
| Atmosphere | 95%Ar-5%H$_2$ |
| Heating speed | 5$^{o}$C/min |
| Holding time | 1 h |
| Cooling speed | Furnace cooling |

## 6.2.3 Characterization

The density of the extruded samples was determined by the Archimedes method. Phase identification was performed by X-ray diffraction (XRD) with Cu Kα radiation. The orientation degree was determined using the Lotgering method [8]. Microstructural observation was conducted by scanning electron microscopy (SEM). Compositional analyses were carried out by energy dispersive X-ray spectroscopy (EDS) and electron probe micro-analyzer (EPMA). Orientation imaging microscopy (OIM) analysis was performed using an SEM equipped with an electron backscattered diffraction (EBSD) system (JEOL, JSM-7001FA).

The Seebeck coefficient ($\alpha$) and electrical resistivity ($\rho$) of the samples were simultaneously measured by static DC method and four-probe method, respectively, using a thermoelectric property test apparatus (ULVAC-RIKO, ZEM-3). The thermal conductivity ($\kappa$) was measured by laser flash method (NETZSCH, LFA457 Micro Flash). In the thermal conductivity measurements, the direction of the heat flux was

set to the extrusion direction. The dimensionless figure of merit *ZT* of the samples was calculated by the equation of $ZT=\alpha^2 T/(\rho\kappa)$.

The mechanical properties at room temperature were evaluated by the Vickers hardness tests at a load of 1.96 N (Shimadzu, HMV-2000). Details of the evaluation methods have been described in section 2.2.4.

**6.3 Results and discussion**

6.3.1 Density, microstructure and texture

Fig. 6.1 shows the dependence of relative density on annealing temperature. The extruded samples have high relative density. After annealing, the relative density slightly decreased in an annealing temperature range of 260~340$^{\circ}$C for the samples extruded at both 340$^{\circ}$C and 400$^{\circ}$C. However, the relative density significantly decreased at ≥380$^{\circ}$C, especially for the samples annealed at 400$^{\circ}$C, as illustrated in Fig. 6.1.
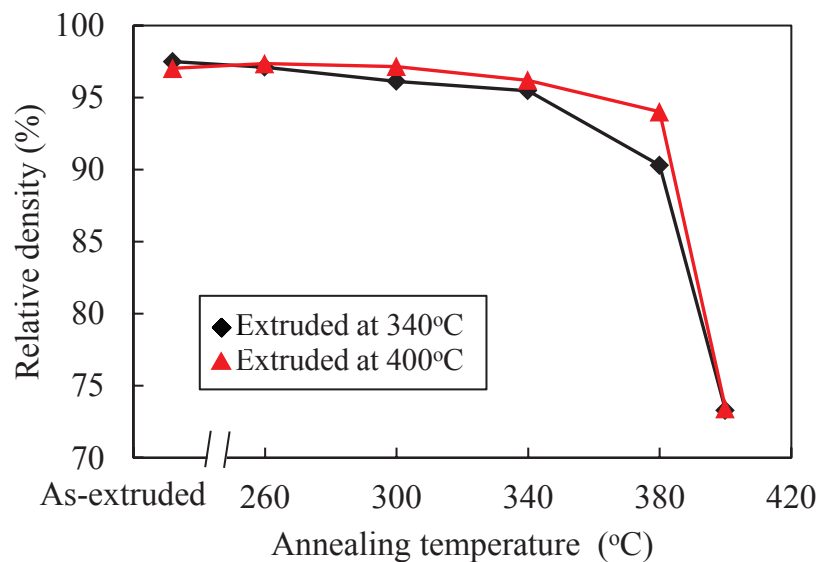


Fig. 6.1 Dependence of relative density on annealing temperature.

In order to clarify the mechanism for the density reduction, microstructural observation was conducted using SEM for the annealed samples. Figs. 6.2 and 6.3 show the SEM images (backscattered electron (BE) mode) of the extruded samples

and their corresponding annealed samples. For all the samples, the images consist of three different contrasts: dark, gray and white regions. With increase in annealing temperature, similar microstructures were observed for the extruded samples and their corresponding annealed samples at $\leq 380^{\circ}$C. However, in the samples annealed at $400^{\circ}$C, large-sized dark regions were found.
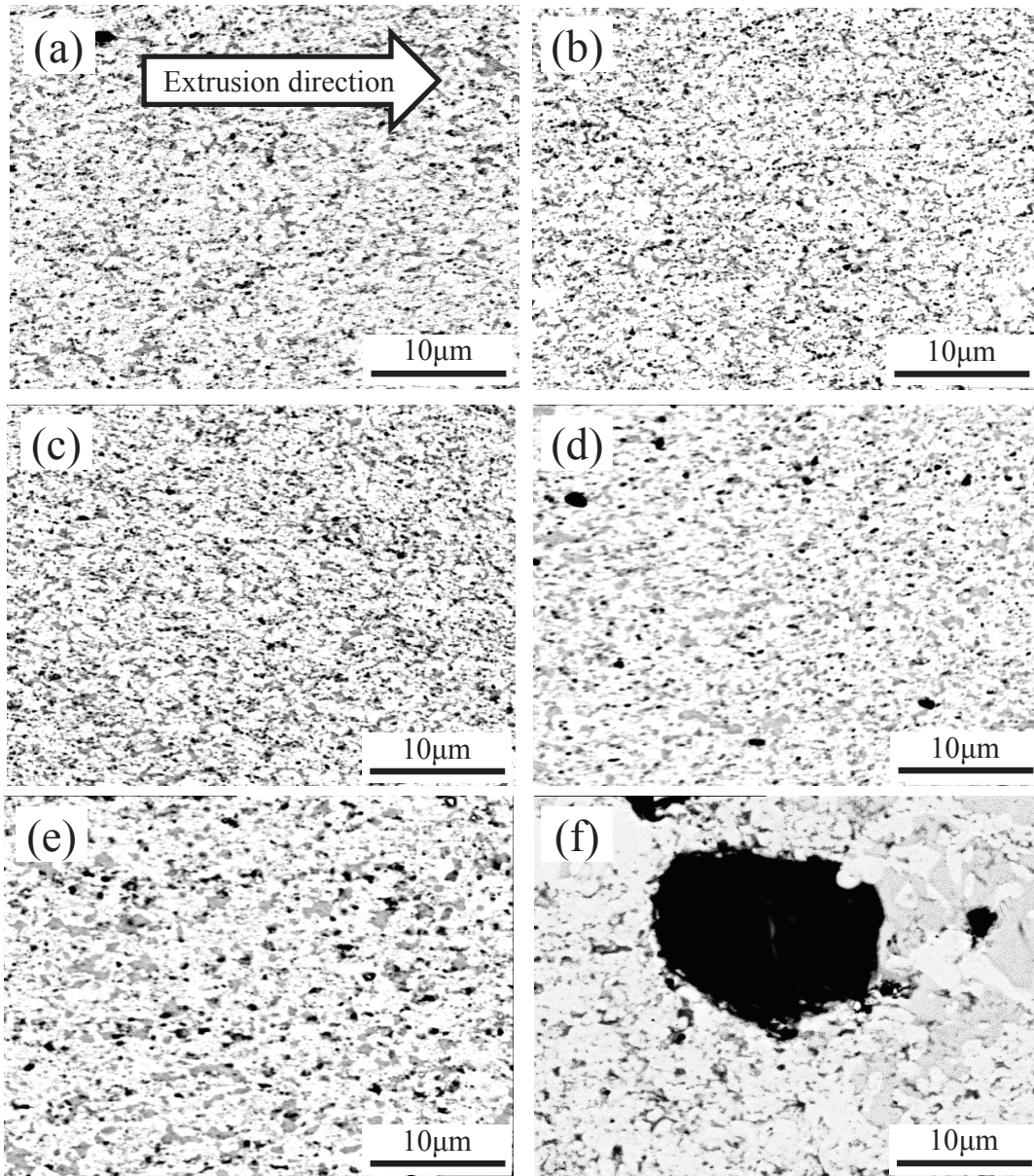


Fig. 6.2 SEM images of (a) the sample extruded at $340^{\circ}$C, and samples annealed at (b) $260^{\circ}$C, (c) $300^{\circ}$C, (d) $340^{\circ}$C, (e) $380^{\circ}$C, and $400^{\circ}$C.
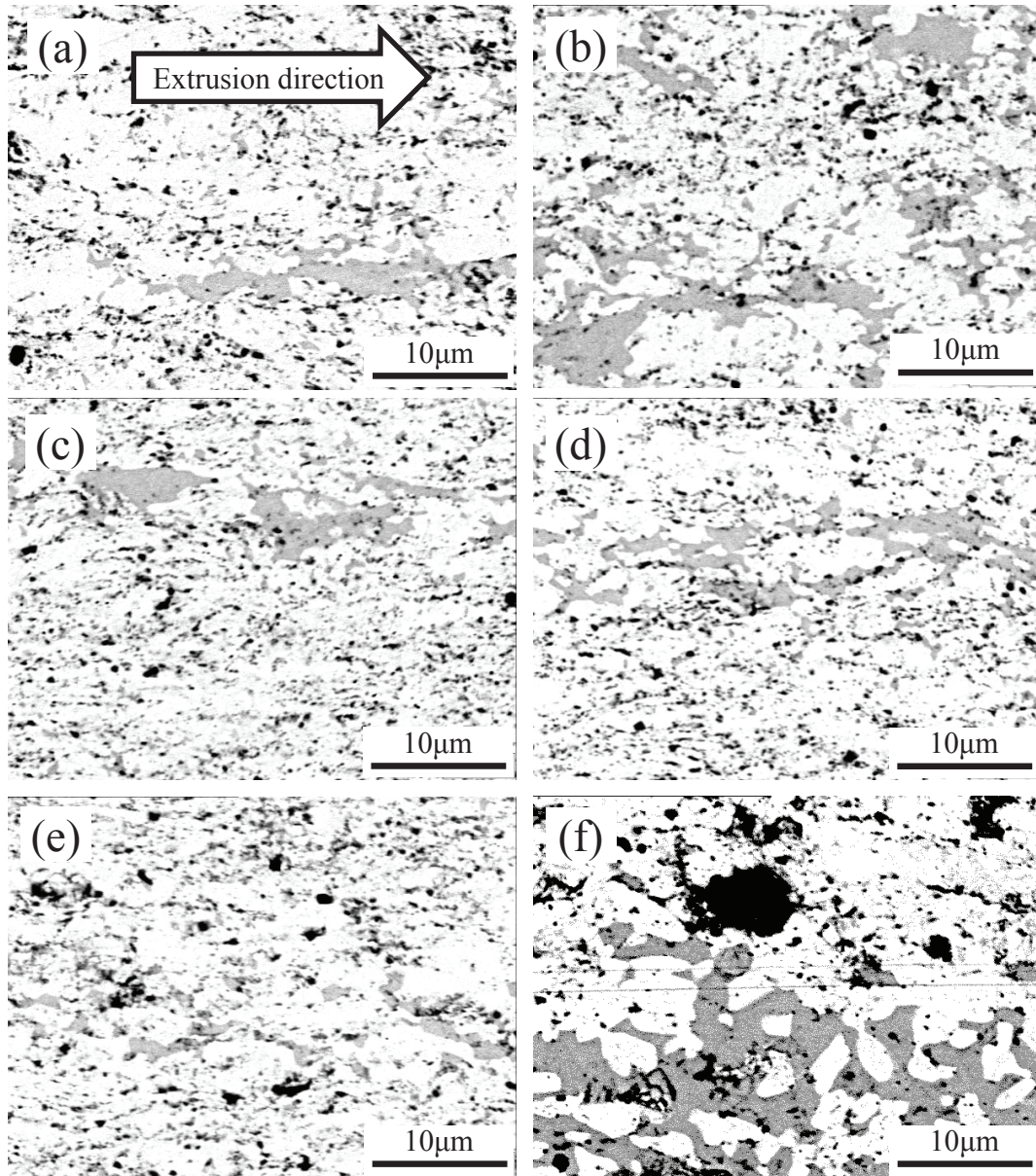
Fig. 6.3 SEM images of (a) the sample extruded at 400$^{\circ}$C, and samples annealed at (b) 260$^{\circ}$C, (c) 300$^{\circ}$C, (d) 340$^{\circ}$C, (e) 380$^{\circ}$C, and 400$^{\circ}$C.

The compositional analysis was performed using EPMA to further clarify the microstructure. Fig. 6.4 shows the EPMA maps of the extruded samples and their corresponding samples annealed at 400$^{\circ}$C. From the maps of the extruded samples and their corresponding annealed samples, it is clearly concluded that the white, gray, and small-sized dark regions correspond to nominal composition (Bi$_{0.4}$Sb$_{1.6}$Te$_3$), Te-rich phase, and Sb-rich phase, respectively. However, the large-sized dark regions observed in the samples annealed at 400$^{\circ}$C (Figs. 6.4(b) and (d)) exhibit low

composition level of Bi, Te, and Sb, which suggests that the large-sized dark regions correspond to pores resulting from the significant sublimation of Te.
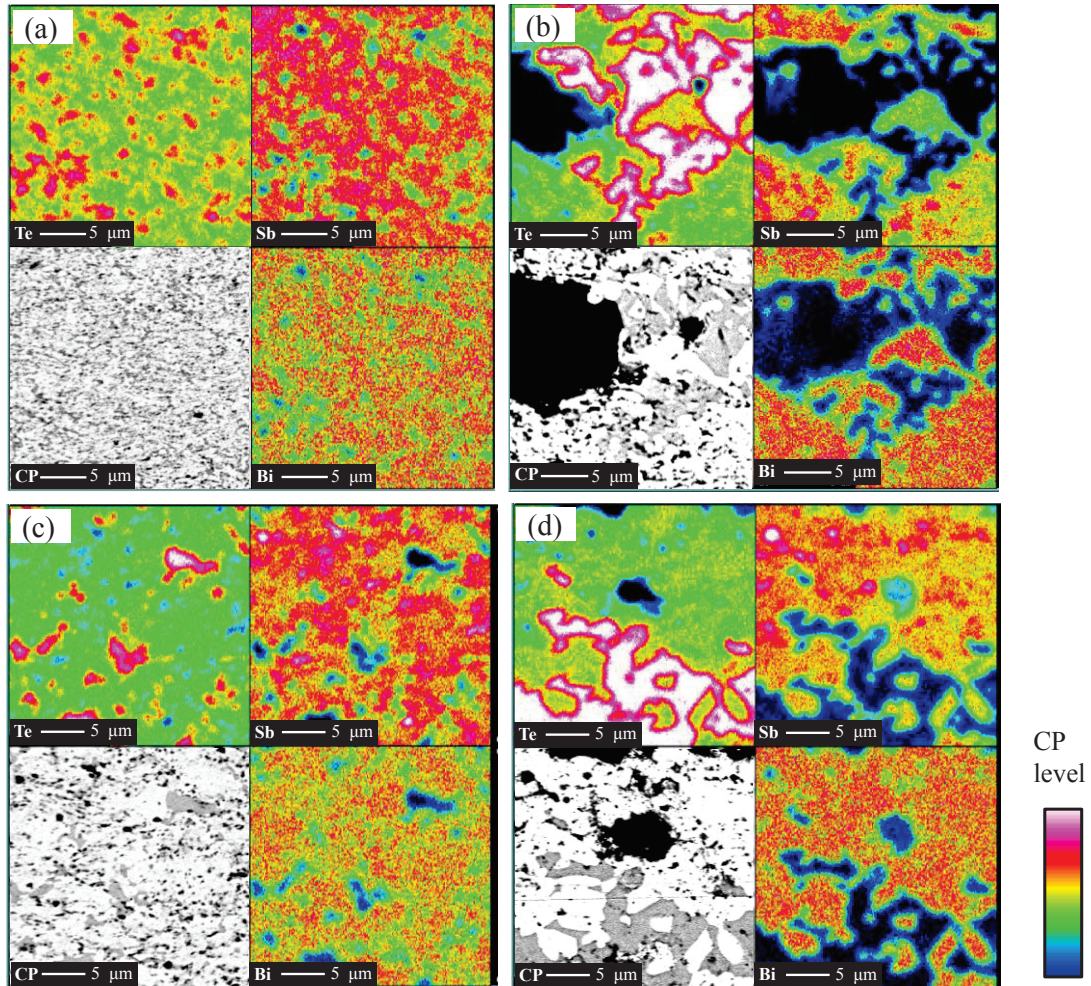


Fig. 6.4 EPMA maps of the samples (a) extruded at 340$^{\circ}$C, and (b) annealed at 400$^{\circ}$C; (c) extruded at 400$^{\circ}$C, and (d) annealed at 400$^{\circ}$C.

Quantitative compositional analysis was also conducted via EDS for the extruded samples, and the results are shown in Fig. 6.5. For the sample extruded at 340$^{\circ}$C, the Te content in the Te-rich phase (point (2) in Fig.6.5(a)) is much lower than that for the sample extruded at 400$^{\circ}$C (point (2) in Fig.6.5(b)), which agrees well with that for the Bi$_2$Te$_{2.85}$Se$_{0.15}$ compounds in Chapter 4. This suggests that the formation of Te-rich phase in $p$-type Bi$_{0.4}$Sb$_{1.6}$Te$_3$ hot-extruded samples is also attributed to two different mechanisms: sublimation of Te and eutectic reaction, as indicated in Chapter 4. In

addition, Sb content is slightly higher (points (3)) than that in the matrix (points (1)). As for the formation of small-sized Sb-rich phase, because the evaporation energy of Sb is higher than that of Bi and Te, it can be concluded that the sublimation of Sb is difficult to occur in this work. Thus, the formation of small-sized Sb-rich phase is likely to be attributed to the remained Sb after sublimation of Te.
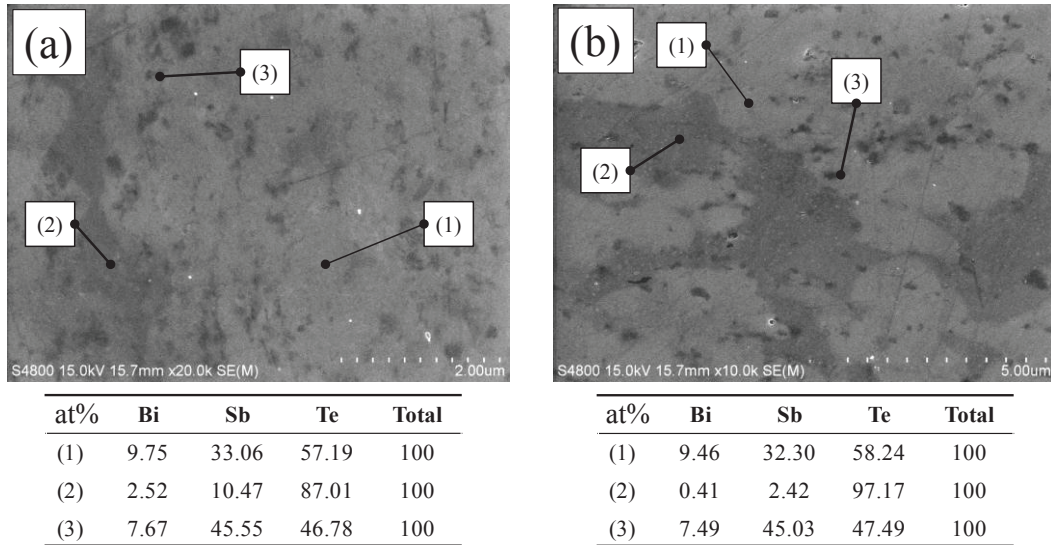


| at% | Bi | Sb | Te | Total |
|-----|------|-------|-------|-------|
| (1) | 9.75 | 33.06 | 57.19 | 100 |
| (2) | 2.52 | 10.47 | 87.01 | 100 |
| (3) | 7.67 | 45.55 | 46.78 | 100 |

| at% | Bi | Sb | Te | Total |
|-----|------|-------|-------|-------|
| (1) | 9.46 | 32.30 | 58.24 | 100 |
| (2) | 0.41 | 2.42 | 97.17 | 100 |
| (3) | 7.49 | 45.03 | 47.49 | 100 |

Fig. 6.5 EDS compositional analysis of the samples extruded at (a) 340$^{\mathrm{o}}$C and (b) 400$^{\mathrm{o}}$C.

The surfaces of the annealed samples were also observed by SEM. It should be noted that the extruded samples were polished firstly, and then subjected to annealing. The annealed samples were observed directly without further polish. Fig. 6.6 shows the SEM images (secondary electron (SE) mode) of the extruded samples and their annealed samples. The results indicate that the annealed samples exhibit similar surface morphologies with the extruded samples at annealing temperature of ≤340$^{\mathrm{o}}$C. However, many large particles were observed on the surfaces of the samples annealed at 380$^{\mathrm{o}}$C. Moreover, it seems that much more particles are formed in the annealed sample extruded at 400$^{\mathrm{o}}$C (Fig. 6.6(f)) compared to the annealed sample extruded 340$^{\mathrm{o}}$C (Fig. 6.6(c)). In addition to the sample surfaces, some particles were also found on the heat treatment container.
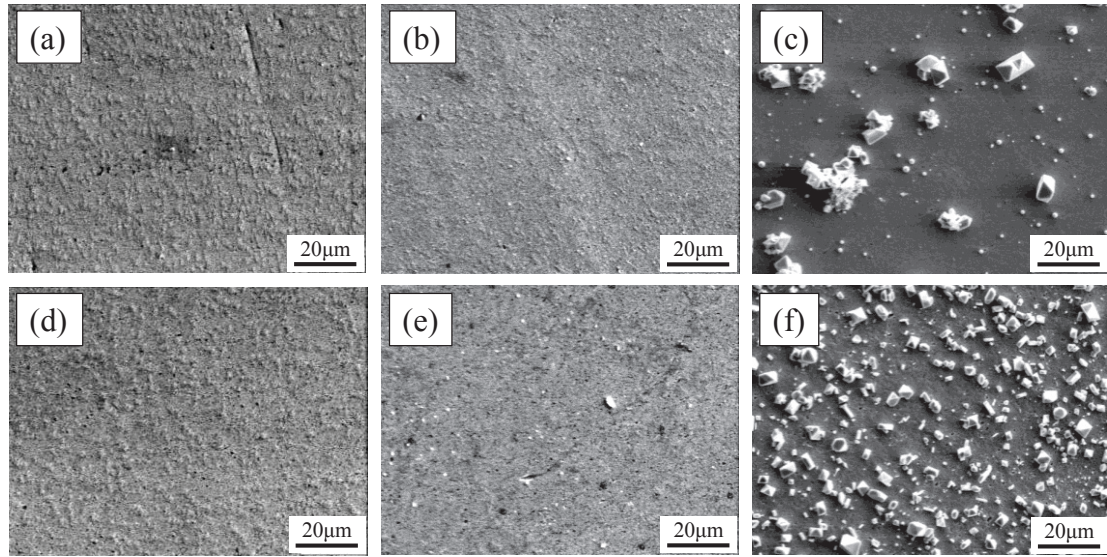
Fig. 6.6 SEM images of the sample (a) extruded at 340$^{\text{o}}$C, and corresponding samples annealed at (b) 260$^{\text{o}}$C and (c) 380$^{\text{o}}$C; (d) extruded at 400$^{\text{o}}$C, annealed at (e) 260$^{\text{o}}$C and (f) 380$^{\text{o}}$C.

The compositional analyses of those particles attached on the heat treatment container and sample surface are conducted by EDS, and the results are shown in Fig. 6.7. The compositional analyses results indicate that the particles attached on the heat treatment container correspond to pure Te, which is due to the significant sublimation of Te as mentioned above. However, the particles attached on the sample surface are related to an antimony oxide. The formation of this antimony oxide is also associated with the oxidation of extra Sb after Te is sublimated. The increased amount of antimony oxide particles (Fig. 6.6(f)) is associated with the larger amount of Te-rich phase before annealing, which results in more significant sublimation of Te, and thus more extra Sb.
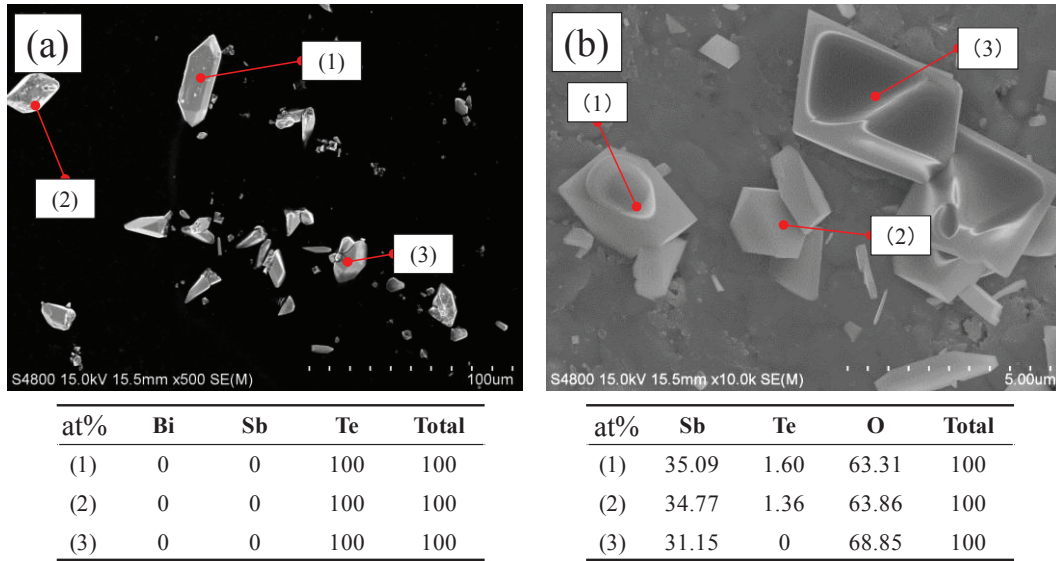
| at% | Bi | Sb | Te | Total |
|-----|-----|-----|-----|-------|
| (1) | 0 | 0 | 100 | 100 |
| (2) | 0 | 0 | 100 | 100 |
| (3) | 0 | 0 | 100 | 100 |

| at% | Sb | Te | O | Total |
|-----|-------|------|-------|-------|
| (1) | 35.09 | 1.60 | 63.31 | 100 |
| (2) | 34.77 | 1.36 | 63.86 | 100 |
| (3) | 31.15 | 0 | 68.85 | 100 |

Fig. 6.7 EDS compositional analyses for the particles (a) attached on the heat treatment container and (b) the surface of sample annealed at 380$^o$C.

The above results indicate that the Sb-rich phase is associated with the remained Sb after sublimation of Te. With the increase in annealing temperature, the sublimation of Te become significant, which leads to the formation of many large-sized pores (Figs. 6.2(f) and 6.3(f)) and reduction of relative density.

Fig. 6.8 shows the XRD patterns of the samples extruded at 340$^o$C and their annealed samples at different temperatures. Although Te-rich phase and Sb-rich phase are found as demonstrated by microstructural and compositional analyses (Figs. 6.2-6.5), all the peaks are attributed to $Bi_{0.4}Sb_{1.6}Te_3$ single phase due to small amounts of those impure phases. In addition, similar results have been confirmed for the samples extruded at 400$^o$C.
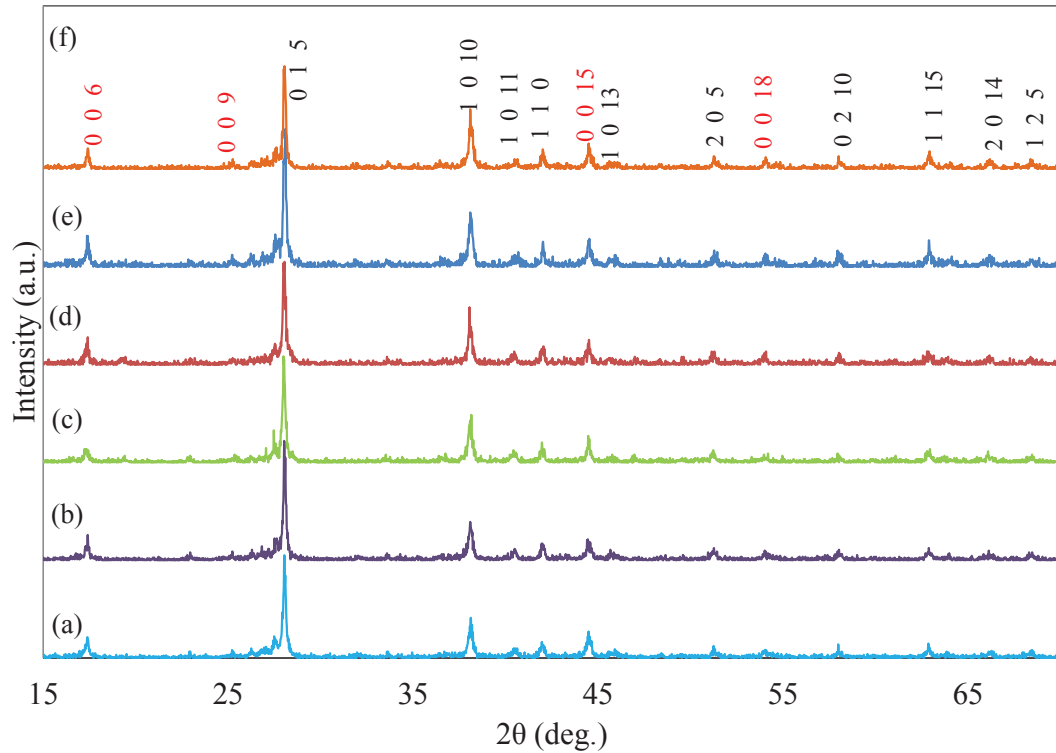
Fig. 6.8 XRD patterns of the samples (a) extruded at 340$^{\circ}$C, and annealed at (b) 260$^{\circ}$C, (c) 300$^{\circ}$C, (d) 340$^{\circ}$C, (e) 380$^{\circ}$C, and (f) 400$^{\circ}$C.

Chapters 2 and 3 have demonstrated that hot-extrusion is an effective way to enhance the preferred orientation. In order to further understand the effect of annealing on grain orientation, quantified orientation degree was calculated from the XRD patterns using the Lotgering method [8]. Fig. 6.9 shows the dependence of orientation factor $f_{(00l)}$ on annealing temperature. From these results, it seems that the orientation degree is independent on the annealing temperature.
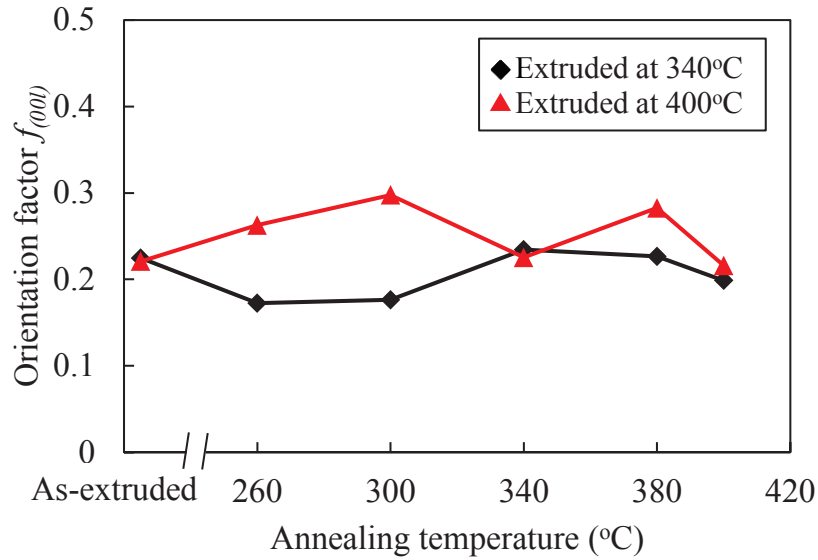
Fig. 6.9 Dependence of orientation factor $f_{(00l)}$ on annealing temperature.

Fig. 6.10 shows the OIM maps of the sample extruded at 340°C and annealed at temperatures ranging from 260°C to 380°C. It is easily found that fine microstructures with equixed grains are obtained for all the samples. Fig. 6.11 shows the OIM maps of the sample extruded at 400°C and its annealed samples. All the samples have a larger average grain size compared to the samples extruded at 340°C (Fig. 6.10) due to the recrystallization and grain growth. Note that, it seems that annealing twin becomes significant in the annealed samples extruded at 400°C. Moreover, all the samples exhibit preferred orientation of (0 0 0 1).
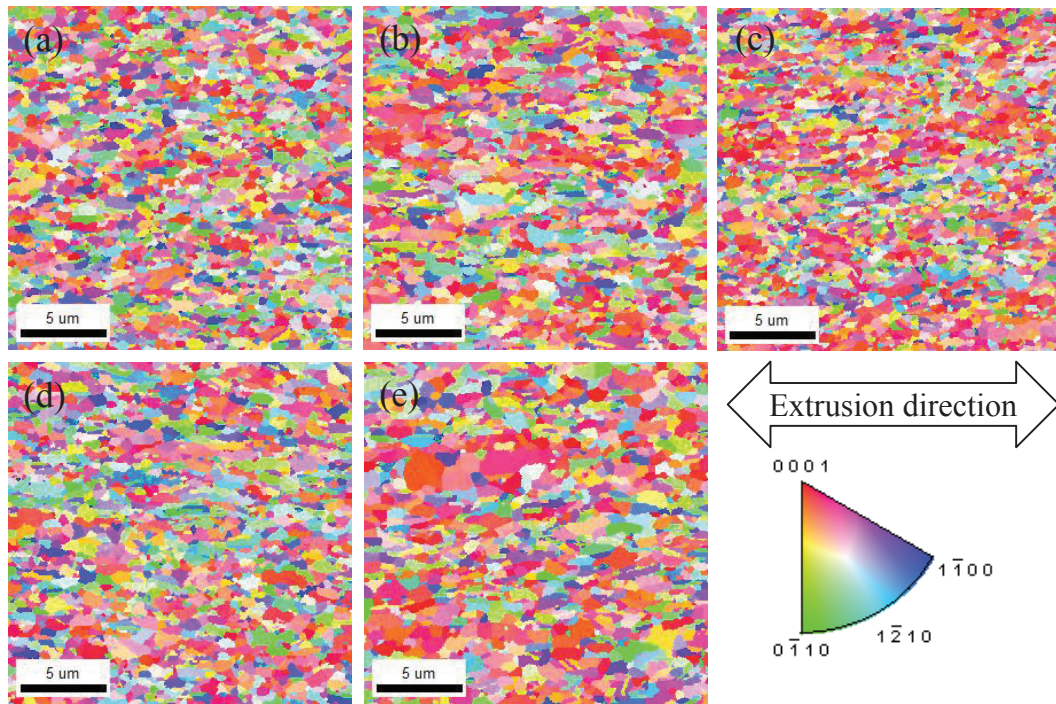
Fig. 6.10 OIM maps of the samples (a) extruded at 340$^o$C, and annealed at (b) 260$^o$C, (c) 300$^o$C, (d) 340$^o$C, and (e) 380$^o$C.
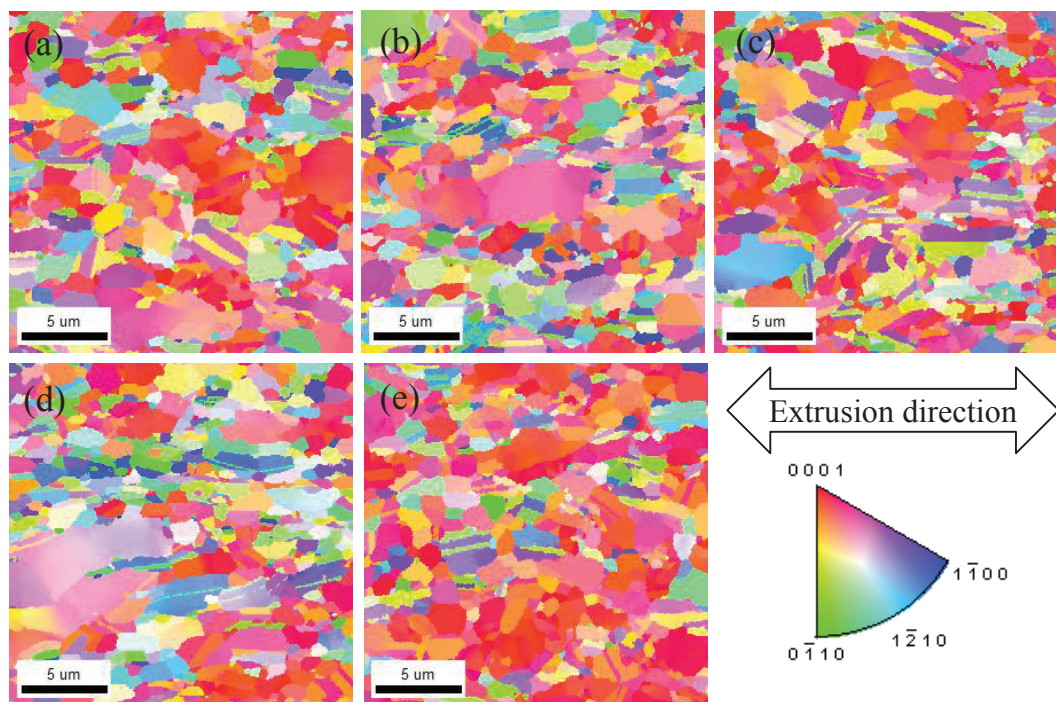


Fig. 6.11 OIM maps of the samples (a) extruded at 400$^o$C, and annealed at (b) 260$^o$C, (c) 300$^o$C, (d) 340$^o$C, and (e) 380$^o$C.

Fig. 6.12 shows the dependence of average grain size on annealing temperature.

As mentioned above, the samples extruded at 400$^{\circ}$C exhibit larger grain size level than that extruded at 340$^{\circ}$C. With the increase in annealing temperature, the average grain size slightly increases at ≥340$^{\circ}$C for the samples extruded at 340$^{\circ}$C, while it seems that the average grain size is independent on annealing temperature in the temperature range of 340~400$^{\circ}$C for the samples extruded at 400$^{\circ}$C.
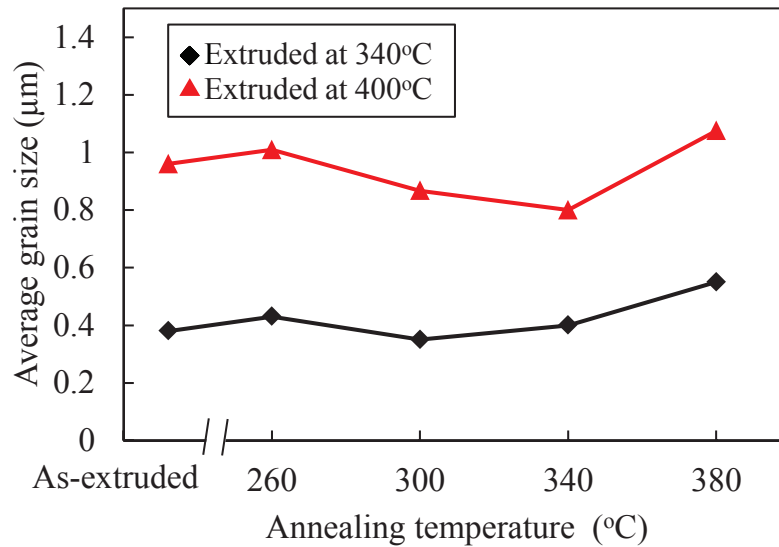


Fig. 6.12 Dependence of the average grain size on annealing temperature.

## 6.3.2 Thermoelectric properties

Fig. 6.13 shows the dependence of the Seebeck coefficient on annealing temperature. The results indicate that the change of the Seebeck coefficient of the samples extruded at 400$^{\circ}$C is small in the whole annealing temperature range, while the Seebeck coefficient significantly increases with annealing temperature below 300$^{\circ}$C, followed by a small change.

As mentioned in the "Introduction" section, the electrical transport properties, such as the Seebeck coefficient and electrical resistivity, are sensitive to the donor-like defects. Liu et al. [2] pointed out that antisite defects, such as [Bi$_{Te}$] or [Sb$_{Te}$], are the dominant donor-like defects for $p$-type Bi$_2$Te$_3$ compounds. The increase in the concentration of antisite defects at Te-sites results in more holes, and thus the Seebeck coefficient is reduced. Therefore, a higher level of the Seebeck coefficient of the

samples extruded at $400^{\circ}C$ and annealed at $\leq300^{\circ}C$ is due to the less remained donor-like defects. The increase for the samples extruded at $340^{\circ}C$ and annealed at $\leq300^{\circ}C$ is attributed to reduction of the donor-like defects.
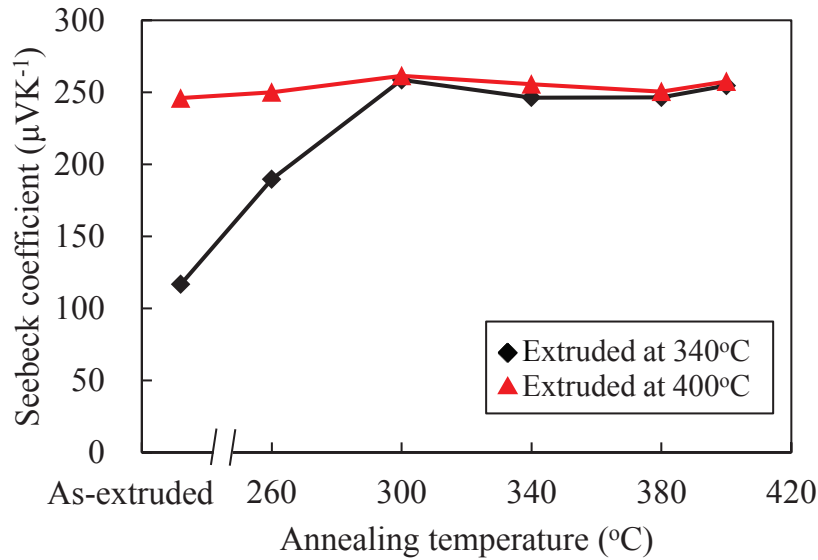


Fig. 6.13 Dependence of the Seebeck coefficient on annealing temperature.

Fig. 6.14 shows the dependence of the electrical resistivity on annealing temperature. Although similar variation tendencies are found for the both batch samples, the variation of the samples extruded at $340^{\circ}C$ is much more significant. The significant decrease in electrical resistivity at annealing temperatures of $\leq340^{\circ}C$ is mainly due to the reduction of donor-like defects. In addition, the decreases in electrical resistivity are also associated with the gradually increased grain size. Note that, the electrical resistivity increases suddenly at annealing temperature of $400^{\circ}C$, as a result of formation of pores, just as mentioned before.
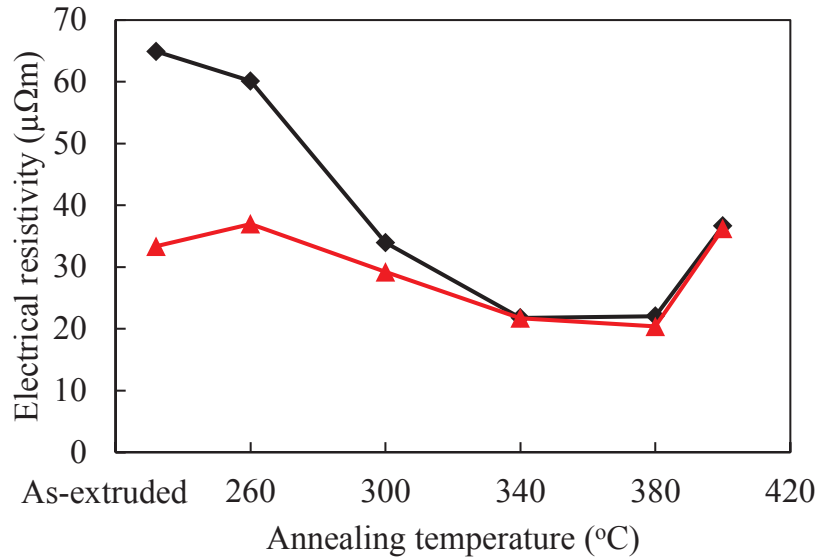
Fig. 6.14 Dependence of the electrical resistivity on annealing temperature.

Fig. 6.15 shows the dependence of the thermal conductivity on annealing temperature. It seems that the effect of annealing temperature on the thermal conductivity is not significant, although the thermal conductivity decreases at the $400^{o}C$ due to the reduced relative density. As a result, significant improvements in figure of merit *ZT* are obtained, as shown in Fig. 6.16, especially for the samples extruded at $340^{o}C$.
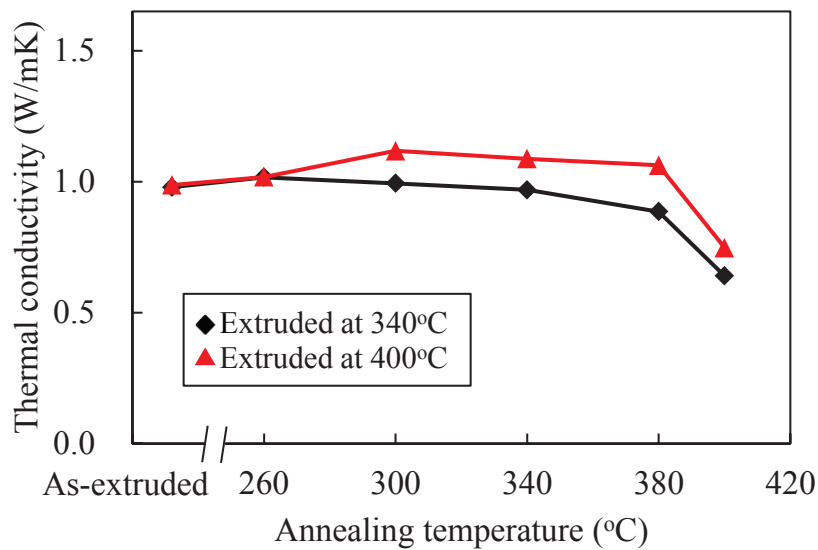


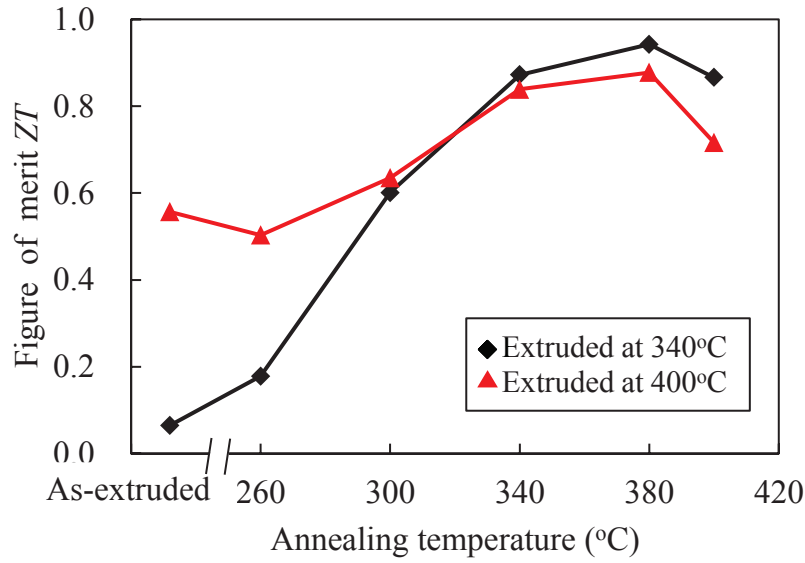Fig. 6.15 Dependence of the thermal conductivity on annealing temperature.

Fig. 6.16 Dependence of figure of merit *ZT* on annealing temperature.

## 6.3.3 Mechanical properties

Fig. 6.17 shows the dependence of the Vickers hardness on annealing temperature. The hardness decreases with increasing annealing temperature due to the increased grain size and decreased relative density. Although the Vickers hardness exhibits a decreased tendency with increasing annealing temperature, the hardness values of the samples annealed at ≤380°C are still much larger than that of zone-melted samples [9].
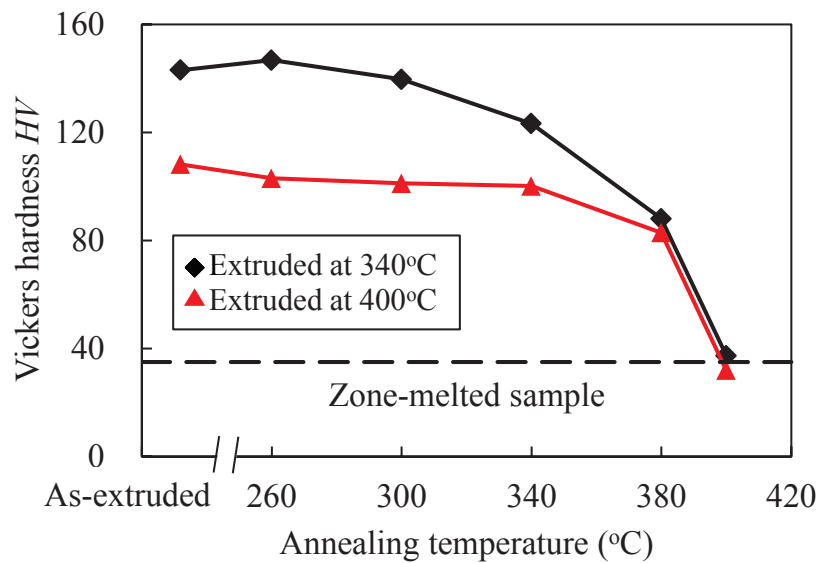


Fig. 6.17 Dependence of the Vickers hardness on annealing temperature.

## 6.4 Conclusions

The effect of annealing temperature on microstructure, thermoelectric and mechanical properties was investigated in this chapter. Some main findings of this chapter are summarized as follows.

(1) The Sb-rich phase is associated with the remained Sb after sublimation of Te. With the increase in annealing temperature, the sublimation of Te becomes significant, which leads to the formation of many large-sized pores and reduction of relative density.

(2) The samples extruded at $340^{\circ}$C and annealed in the temperature range of $260{\sim}400^{\circ}$C exhibit fine microstructures with equixed grains, as well as slight increase of average grain size with increasing annealing temperature. As for the samples extruded at $400^{\circ}$C, the average grain size is independent on annealing temperature at $\leq 400^{\circ}$C. In addition, annealing twin becomes significant.

(3) The effect of annealing on the Seebeck coefficient of the samples extruded at $400^{\circ}$C is not obvious, while the Seebeck coefficient is increased significantly at annealing temperature of $\leq 300^{\circ}$C for the samples extruded at $340^{\circ}$C. The electrical resistivity is decreased with increasing annealing temperature.

(4) The effect of annealing on the thermal conductivity is not significant. As a result, significant improvement in figure of *ZT* is obtained for the hot-extruded samples, especially for the samples extruded at $340^{\circ}$C.

(5) Although the Vickers hardness exhibits a decreased tendency as temperature increases, the hardness values of the samples annealed at $\leq 380^{\circ}$C are still much larger than that of zone-melted sample.

## References

[1] W. S. Liu, Q. Zhang, Y. Lan, S. Chen, X. Yan, Q. Zhang, H. Wang, D. Z. Wang, G. Chen, Z. F. Ren, Adv. Energy Mater. 1(4) (2011) 577-587.

[2] L. Hu, T. Zhu, X. Liu, X. Zhao, Adv. Funct. Mater. 24(33) (2014) 5211-5218.

[3] Y. Pan, T. R. Wei, C. F. Wu, J. F. Li, J. Mater. Chem. C 3(40) (2015), 10583-10589.

[4] X. D. Liu, Y. H. Park, Mater. Trans. 43 (2003) 681.

[5] C.W. Bhandari, D. M. Rowe, D. M. Rowe (Ed.), CRC Handbook of Thermoelectrics, CRC Press, New York, 1995, 43–44.

[6] L. D. Zhao, B. P. Zhang, W. S. Liu, H. L. Zhang, J. F. Li, J. Alloys Compd. 467 (2009) 91-97.

[7] J. M. Schultz, J. P. Mchugh, W. A. Tiller, J. Appl. Phys. 33 (1962) 2443.

[8] P. Scherrer, Math-Phys Klasse 2 (1918) 98-100.

[9] Z. J. Xu et al., Acta Mater. 84 (2015) 385-392

# Chapter 7 Fabrication of Bi-Sb-Te thermoelectric materials from rapidly solidified powders

## 7.1 Introduction

As described in Chapters 2 and 3, $Bi_2Te_3$-based bulk thermoelectric materials have been successfully fabricated by MA and hot-extrusion technique. The extruded samples had better comprehensive performance than directionally solidified ingots and hot-pressed samples due to the oriented fine-grained microstructure. Further performance improvement was obtained via doping (Chapter 5) and heat treatment (Chapter 6). However, it is difficult to realize mass production due to the small scale production process of MA. In this chapter, an exploratory study has been carried out, where a potential rapid solidification (RS) method was proposed to prepare the alloy powders with small crystalline sizes. The purpose of this study was to explore the feasibility of combination of RS and hot extrusion to fabricate $p$-type $Bi_{0.4}Sb_{1.6}Te_3$ bulk materials, and clarify the relationships among processing conditions, microstructure, as well as thermoelectric and mechanical properties.

## 7.2 Experimental procedure

### 7.2.1 Powder preparation by RS

High purity Bi (99.99%, 150 µm), Sb (99.99%, 150 µm), and Te (99.99%, 150 µm) powders were used as the starting materials. The master alloy with a composition of $Bi_{0.4}Sb_{1.6}Te_3$ was prepared, and then it was filled into a quartz tube in mini-type gas atomization equipment (VF-RQP200). The alloy was induction-melted under vacuum atmosphere and rapidly solidified by gas atomization method using Ar with an ejection pressure of 5 MPa. The schematic drawing of gas atomization device is shown in Fig. 7.1.
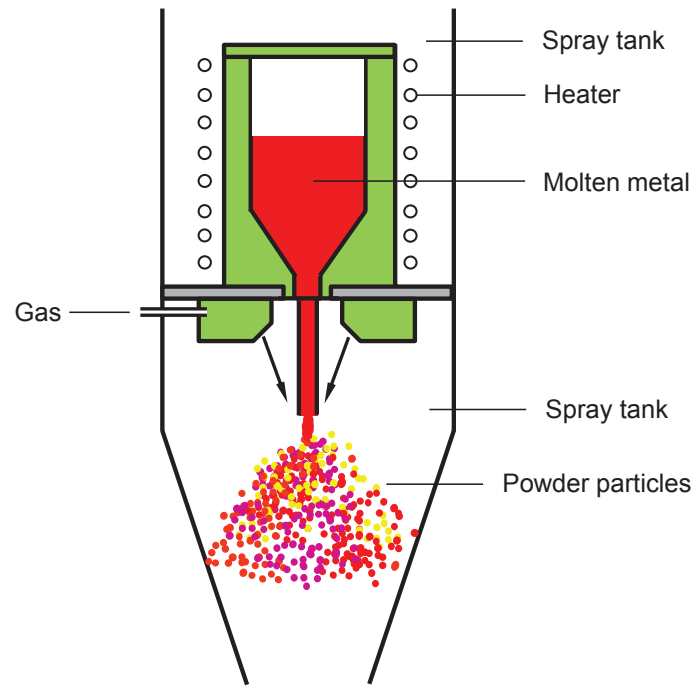
Fig. 7.1 Schematic drawing of gas atomization device.

### 7.2.2 Consolidation by SPS

The RSed alloy powder was consolidated by SPS. The SPS was conducted in a temperature range of $340 \sim 450^{o}C$ under an axial compressive stress of 50 MPa and sintering time of 5 min. The schematic drawing of SPS device is shown in Fig. 7.2.
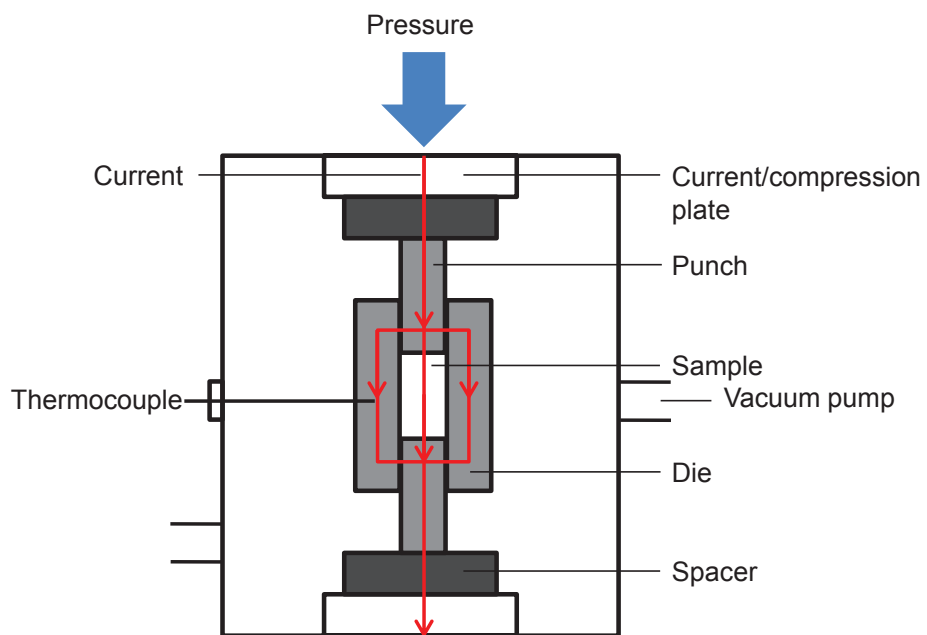


Fig. 7.2 Schematic drawing of SPS device.

7.2.3 Consolidation by hot extrusion

The RSed alloy powder was also consolidated by hot extrusion method. Firstly, the powder was pressed into a cylindrical green compact at room temperature by uniaxial pressing under 200 MPa, which was used as a hot-extrusion billet. Hot extrusion was performed in a temperature range of 340-450$^{\circ}$C with an extrusion ratio of 25:1 at a punch speed of 1 mm/min.

7.2.4 Characterization

The density of the extruded samples was determined by the Archimedes method. Phase identification was performed by X-ray diffraction (XRD) with Cu Kα radiation. Microstructural observations were conducted by scanning electron microscopy (SEM). Orientation imaging microscopy (OIM) analysis was performed using an SEM equipped with an electron backscattered diffraction (EBSD) system (JEOL-7001FA).

The electron transport properties were evaluated by a Hall effect measurement system (TOYO Corp., Resi Test 8300). The Seebeck coefficient ($\alpha$) and electrical resistivity ($\rho$) of the samples were simultaneously measured by static DC method and four-probe method, respectively, using a thermoelectric property test apparatus (ULVAC-RIKO, ZEM-3). The thermal conductivity ($\kappa$) was measured by laser flash method (NETZSCH, LFA457 Micro Flash). The dimensionless figure of merit of the samples was calculated by the equation of $ZT=\alpha^2 T/(\rho\kappa)$.

The mechanical properties at room temperature were evaluated by the Vickers hardness tests at a load of 1.96 N (Shimadzu, HMV-2000). Details of the evaluation methods have been described in Section 2.2.4.

**7.3 Results and discussion**

7.3.1 Preparation of alloy powders

Fig. 7.3 shows the SEM image of the RSed alloy powder. Most of the powder particles exhibited a spherical shape with particle sizes of <10μm in diameter as well as smooth surfaces.
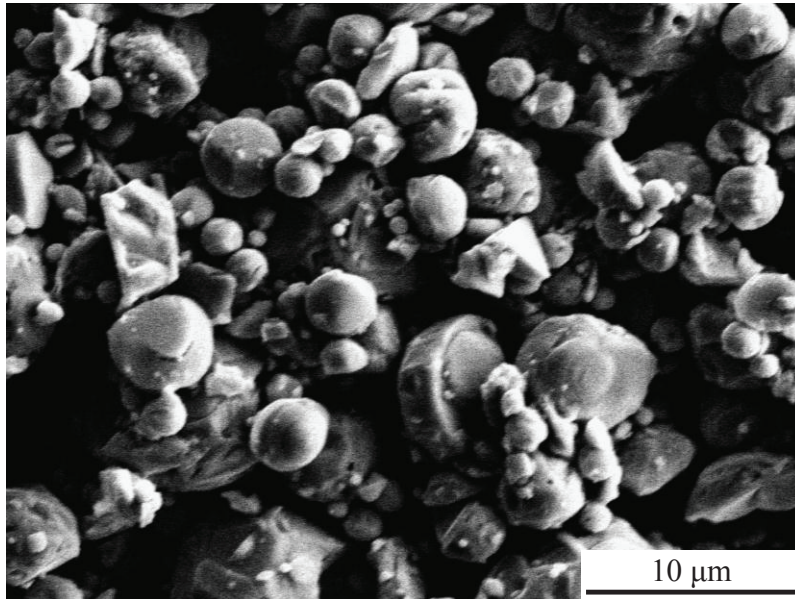
Fig. 7.3 SEM image of the rapidly solidified powder.

Fig. 7.4 shows the XRD pattern of the RSed powder. As a reference, the standard JCPDS data of $Bi_{0.4}Sb_{1.6}Te_3$ compound were included. The result indicated that the RSed powder was attributed to $Bi_{0.4}Sb_{1.6}Te_3$ single phase with average crystallite size of 52.41 nm calculated by the Scherrer equation [1]. The above results indicate that the Bi-Sb-Te alloy powders with small crystallite size can be prepared by RS method.
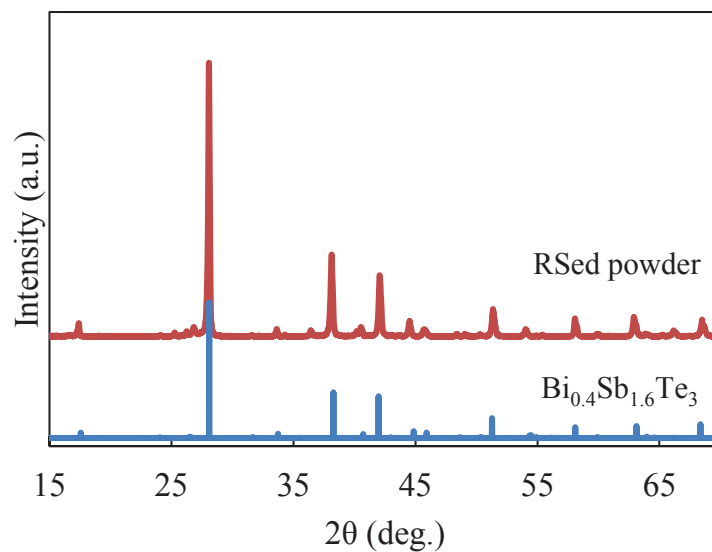


Fig. 7.4 XRD pattern of the RSed powder.

7.3.2 Density, phase, and microstructure of SPSed samples

Fig. 7.5 shows the relative density of the samples sintered at different temperatures. All the SPSed samples had high relative densities of >99%.
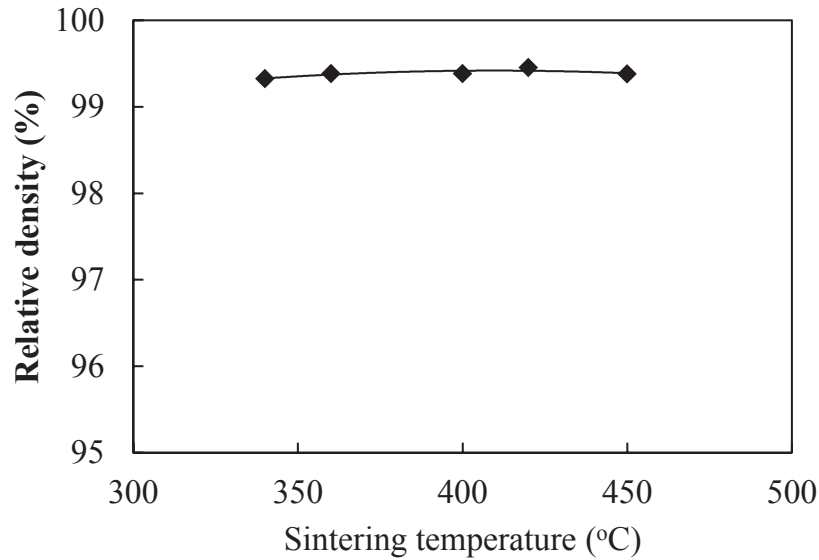


Fig. 7.5 Relative density of the samples sintered at different temperatures.

Fig. 7.6 shows the XRD patterns of the samples sintered at different temperatures. All the samples are attributed to $Bi_{0.4}Sb_{1.6}Te_3$ single phase. It seems that there is almost no change for all these patterns at different sintering temperatures, including relative intensities and diffraction angles of the peaks.
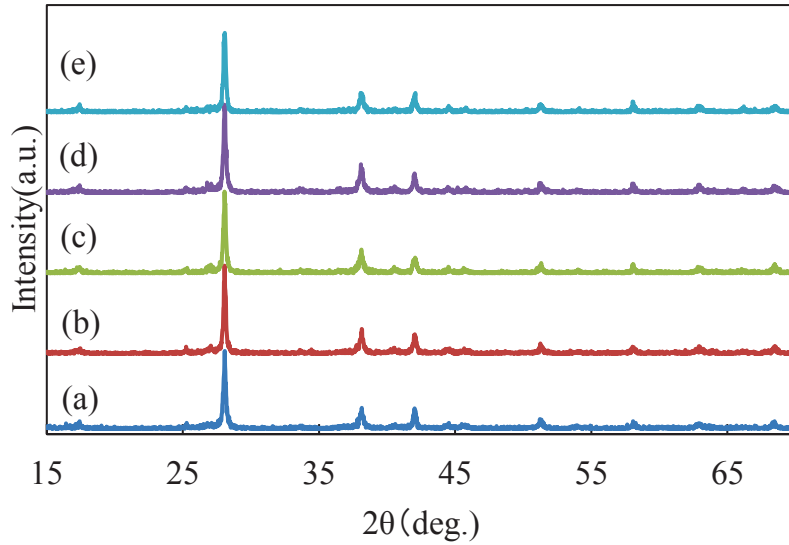
Fig. 7.6 XRD patterns of the samples sintered at (a) 340$^{\circ}$C, (b) 360$^{\circ}$C, (c) 400$^{\circ}$C, (d) 420$^{\circ}$C, and (e) 450$^{\circ}$C.

Fig. 7.7 shows the OIM maps on the transverse sections (perpendicular to loading direction) of the samples sintered at different temperatures. It was easily found that the grains grew up gradually with the increase in sintering temperature. The average grain sizes were measured as 1.19 μm, 1.62 μm, and 1.87 μm at 340$^{\circ}$C, 400$^{\circ}$C, and 450$^{\circ}$C, respectively. The dependence of average grain size on sintering temperature is shown in Fig. 7.8. It is seen that the average grain size increases almost linearly with sintering temperature.
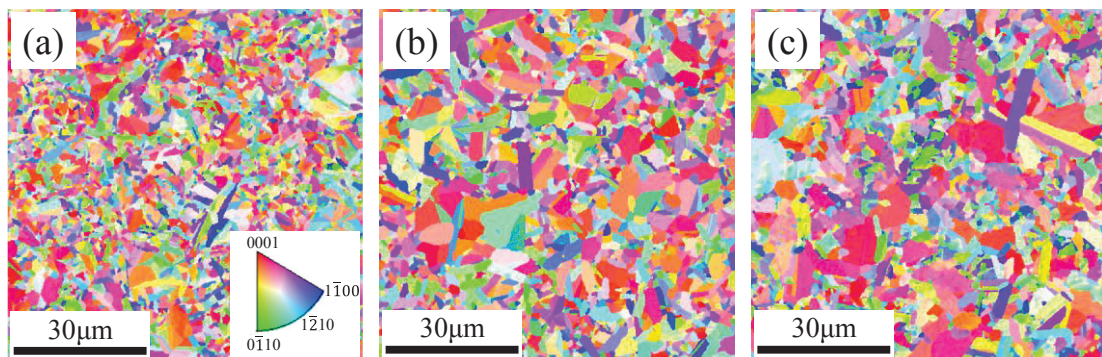


Fig. 7.7 OIM maps of the samples sintered at (a) 340$^{\circ}$C, (b) 400$^{\circ}$C, and (c) 450$^{\circ}$C.
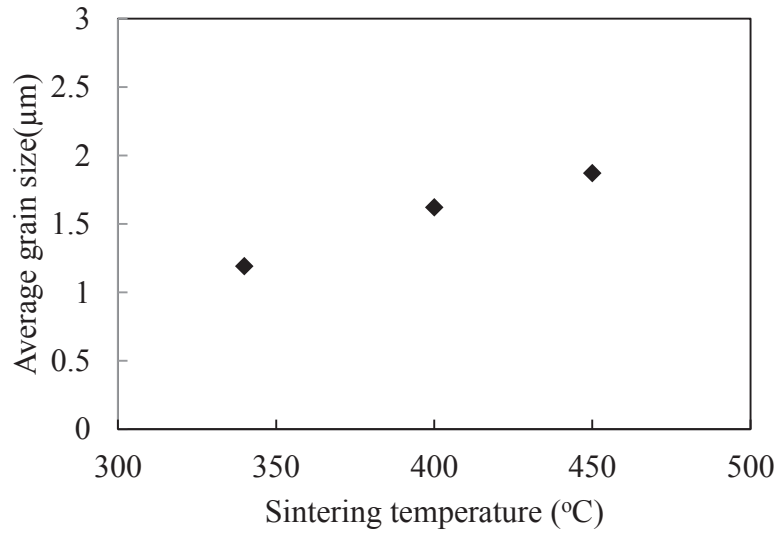
Fig. 7.8 Dependence of average grain size on sintering temperature.

Fig. 7.9 shows the corresponding (0 0 0 1) pole figures of the SPSed samples. From these pole figures, no obvious preferred orientations were found on the transverse sections.
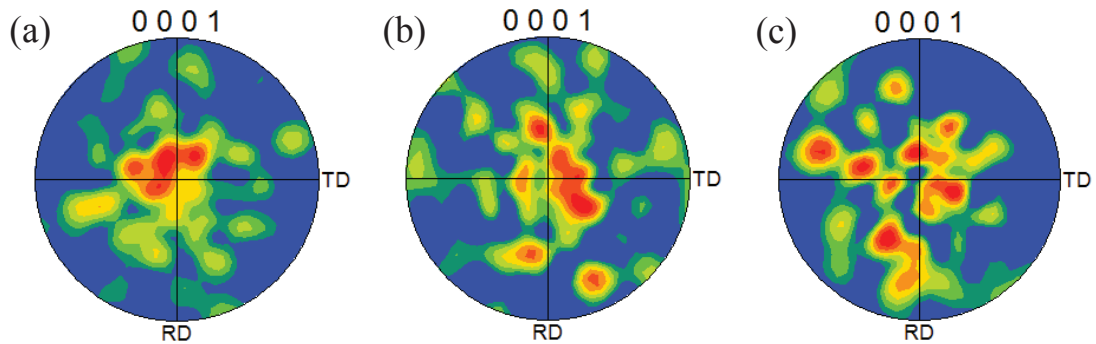


Fig. 7.9 (0 0 0 1) pole figures of the samples sintered at (a) 340°C, (b) 400°C, and (c) 450°C.

The above results indicate that highly dense $Bi_{0.4}Sb_{1.6}Te_3$ bulk materials with fine-grained microstructure can be fabricated by RS and SPS technique.

7.3.3 Thermoelectric properties of SPSed samples

Fig. 7.10 shows the dependence of the carrier concentration on sintering temperature. It seems that the effect of sintering temperature on carrier concentration

is not significant, although it appears that there is a minimum value at 400$^{\text{o}}$C. This is likely to be due to less residual lattice defects resulting from RS and SPS processes, because the carrier concentration is highly sensitive to the lattice defects [2-4]. Nevertheless, the carrier concentration in the entire sintering temperature range exhibited a low level, which is beneficial to the related Seebeck coefficient, as will be described later.
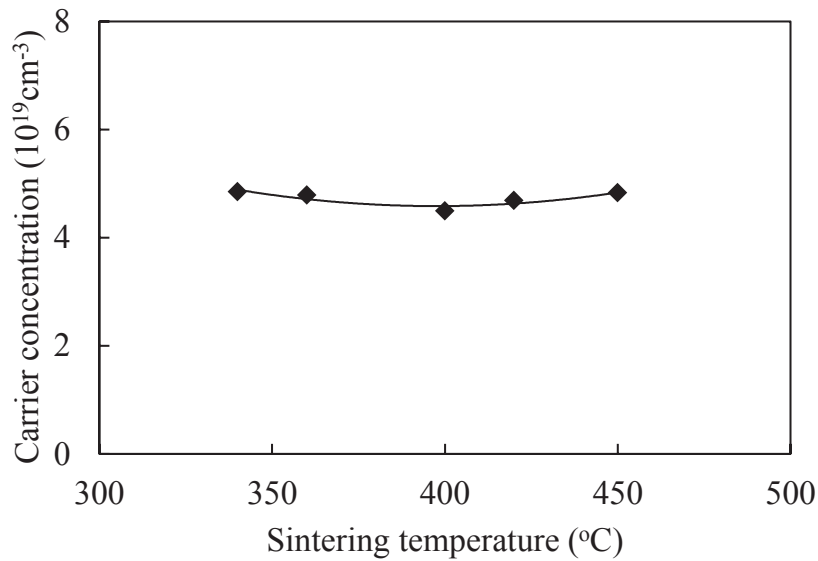
Fig. 7.10 Dependence of the carrier concentration on sintering temperature.

Fig. 7.11 shows the dependence of the mobility on sintering temperature. The mobility showed an increased tendency as sintering temperature increased. This is mainly due to the grain growth, because fine grains promote carriers scattering at grain boundaries and thus decrease the mobility.
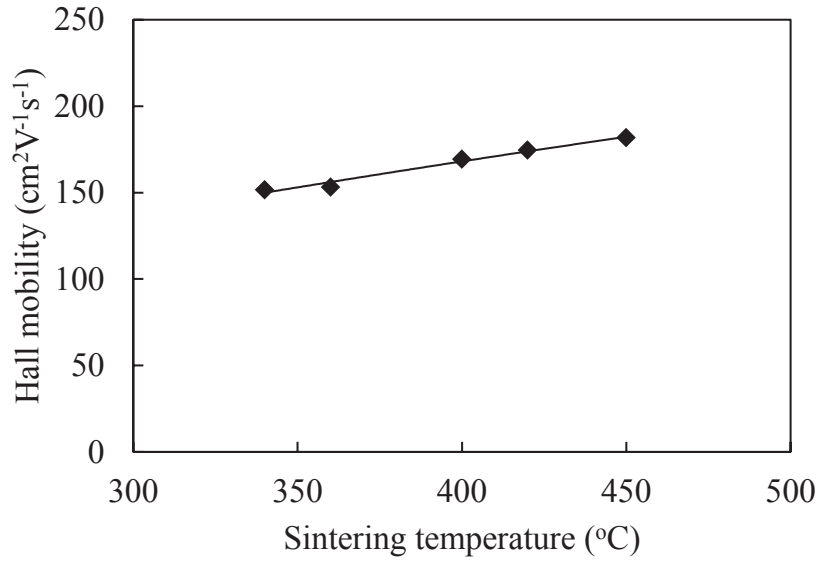
Fig. 7.11 Dependence of the mobility on sintering temperature.

Fig. 7.12 shows the dependence of the Seebeck coefficient on sintering temperature. The change of the Seebeck coefficient was not obvious with increasing sintering temperature. This is understandable because the Seebeck coefficient highly depends on the carrier concentration, and it is determined by $\alpha \approx \gamma - ln\ n$ [5], where $\alpha$, $\gamma$ and $n$ are the Seebeck coefficient, scattering factor, and carrier concentration, respectively.
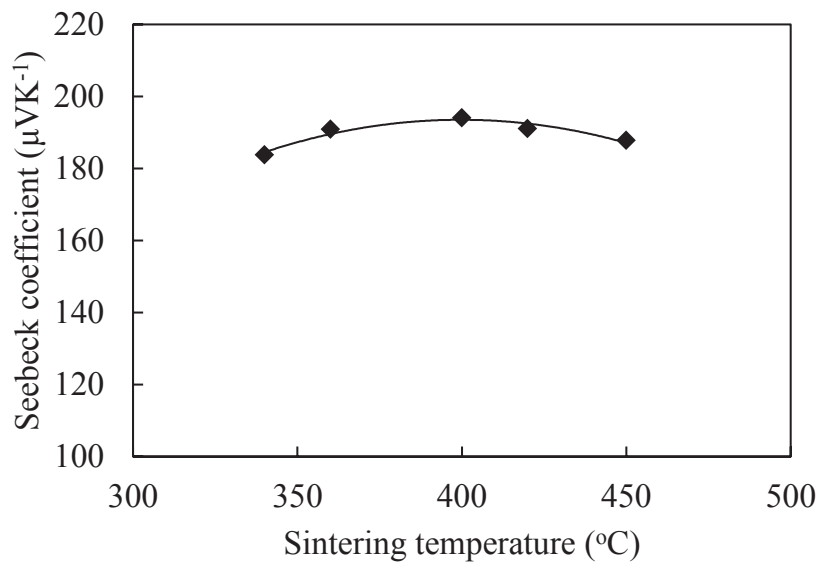


Fig. 7.12 Dependence of the Seebeck coefficient on sintering temperature.

Fig. 7.13 shows the dependence of the electrical resistivity on sintering temperature. The electrical resistivity showed a slightly decreasing tendency with increasing sintering temperature. The relation among electrical resistivity, carrier concentration, and mobility can be expressed as $\rho=1/ne\mu$ [5], where $\rho$, $e$, and $\mu$ are the electrical resistivity, the electron charge, and the carrier mobility, respectively. Therefore, the reduction of electrical resistivity results from the interaction of carrier concentration and mobility. In addition, the decreased electrical resistivity is also attributed to grain growth, which causes decrease in scattering of carriers and thus electrical resistivity.
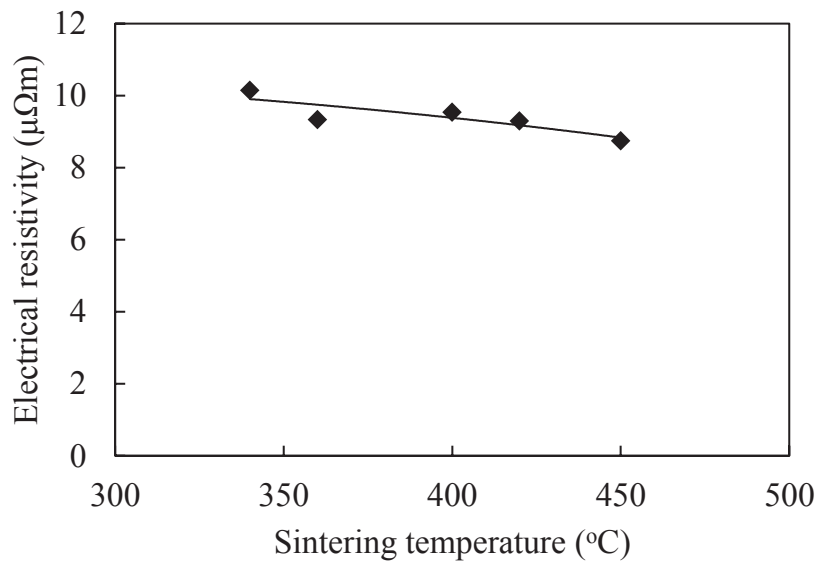


Fig. 7.13 Dependence of the electrical resistivity on sintering temperature.

Fig. 7.14 shows the dependence of the thermal conductivity on sintering temperature. The thermal conductivity remained almost unchanged until $400^{o}C$, followed by a rapid rise with sintering temperature. The thermal conductivity, $\kappa$, is determined by lattice thermal conductivity ($\kappa_{ph}$) and electron thermal conductivity ($\kappa_{el}$) [6] via $\kappa = \kappa_{ph} + \kappa_{el}$. The increased tendency of the thermal conductivity at above $400^{o}C$ is mainly due to grain growth, which leads to the decrease in phonon scattering from grain boundaries and thus increase in thermal conductivity. The small change in thermal conductivity at sintering temperatures of $\leq 400^{o}C$ is likely to be due to the

small reduction of carrier concentration (Fig. 6.9) resulting in decrease of $\kappa_{el}$, which counteracts the increase of $\kappa_{ph}$.
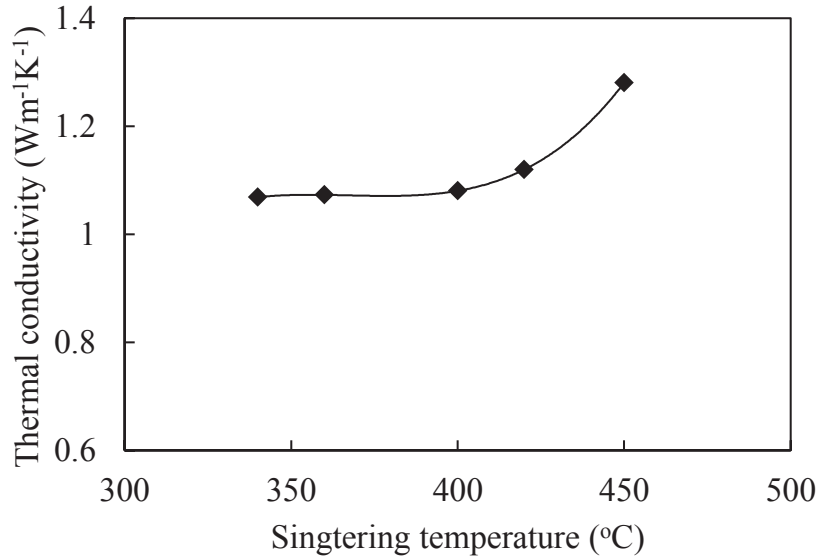


Fig. 7.14 Dependence of the thermal conductivity on sintering temperature.

The dependence of figure of merit $ZT$ on sintering temperature is shown Fig. 7.15. The figure of merit $ZT$ exhibited a high level with values close to 1 for all the samples sintered at different temperatures. A largest $ZT$ value of 1.1 was achieved for the sample sintered at $400^{\circ}C$.
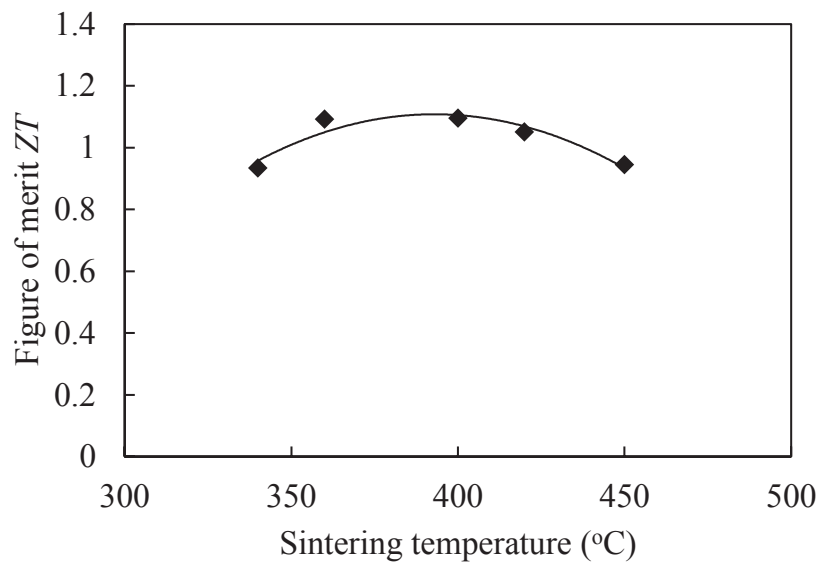


Fig. 7.15 Dependence of figure of merit $ZT$ on sintering temperature.

## 7.3.4 Mechanical properties of SPSed samples

The mechanical properties of the SPSed samples were evaluated by Vickers hardness. Fig. 7.16 shows the dependence of Vickers hardness on sintering temperature. Although the hardness decreased with increasing the extrusion temperature due to the grain growth, the minimum value of 63 is still almost 2 times larger than that of zone-melted sample [7].
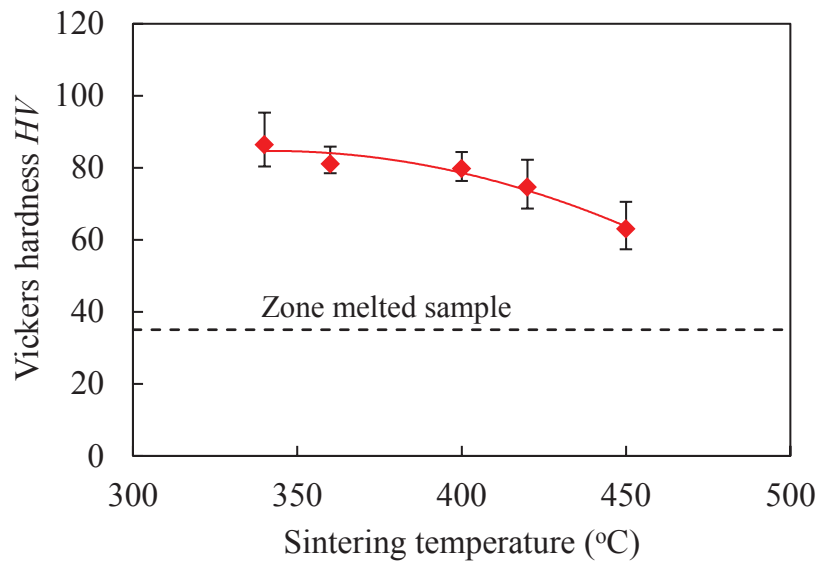


Fig. 7.16 Dependence of Vickers hardness on sintering temperature.

## 7.3.5 Extrusion behavior and texture of hot-extruded samples

The SPS results proved that RS was an effective powder preparation method. Therefore, RS and hot-extrusion was combined to try to fabricate $Bi_{0.4}Sb_{1.6}Te_3$ bulk materials in an extrusion temperature range of 340~450$^o$C.

The results indicated that all the extruded samples had high relative density and sound appearances, as shown in Fig. 7.17. Typical extrusion pressure-stroke curves are given in Fig. 7.18 for the RS/hot-extruded samples.
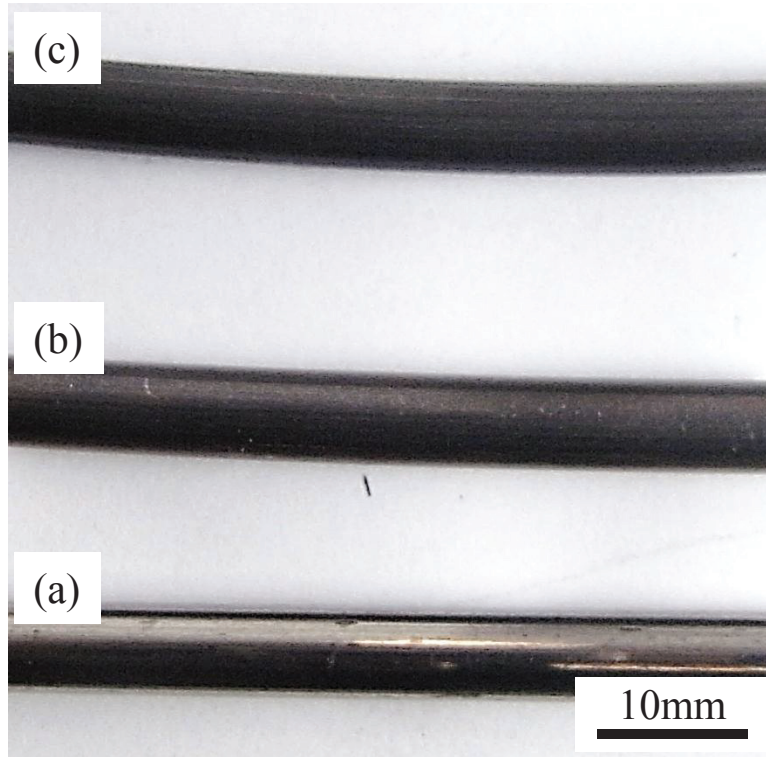
Fig. 7.17 Appearances of the samples extruded at (a) 340$^{\circ}$C, (b) 400$^{\circ}$C, and (c) 450$^{\circ}$C)
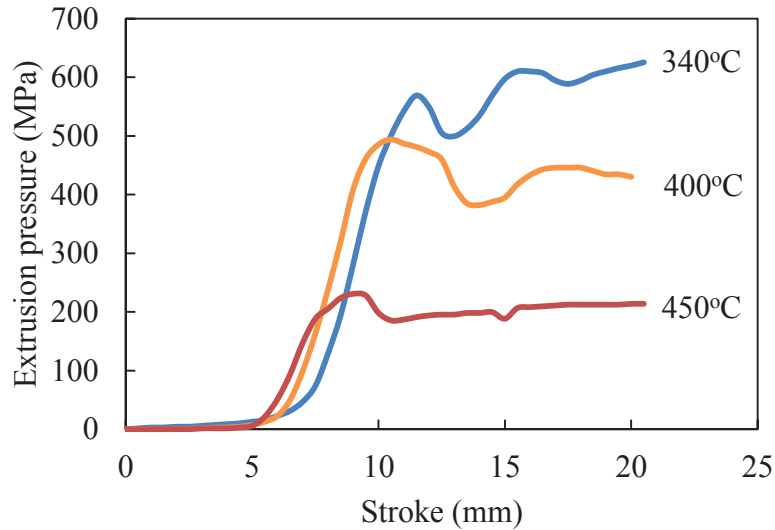


Fig. 7.18 Extrusion pressure–stroke curves of the extruded samples.

The texture of the extruded samples was studied using XRD measurement. Take the sample extruded at 400$^{\circ}$C as an example, as shown in Fig. 7.19, the textures attributed to basal planes such as (0 0 6), (0 0 9), (0 0 15), and (0 0 18) were enhanced and oriented parallel to the extrusion direction on the longitudinal section compared

with those on the transverse section. This result agrees well with that of the MA/hot-extruded sample (Fig. 2.9).



Fig. 7.19 XRD patterns on the longitudinal and transverse sections.

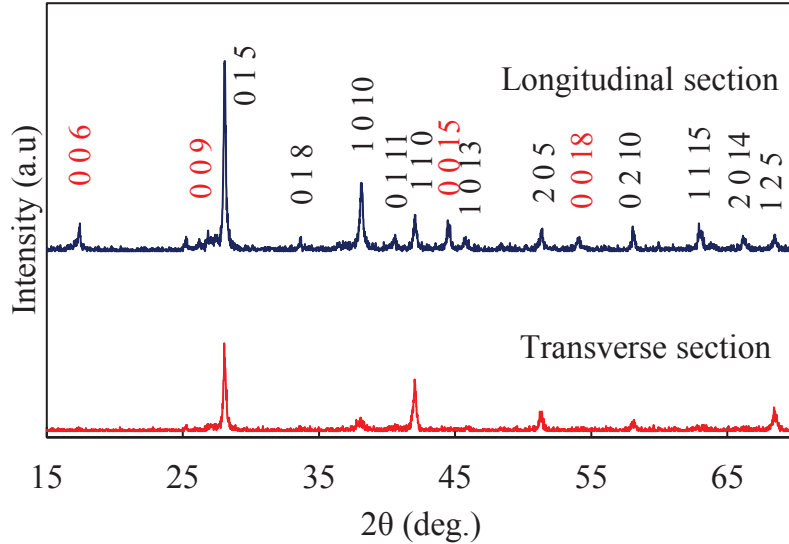The above results indicate that fabrication of dense $Bi_{0.4}Sb_{1.6}Te_3$ bulk thermoelectric materials with preferred orientation by RS and hot-extrusion technique is feasible.

### 7.3.6 Thermoelectric properties of hot-extruded samples

Fig. 7.20 shows the dependences of the Seebeck coefficient and electrical resistivity on extrusion temperature. As the extrusion temperature increased, the Seebeck coefficient was increased, while the electrical resistivity was decreased significantly. It can be deduced that these variations are associated with the carrier concentration and mobility, as demonstrated in Figs. 7.12 and 7.13. The reduction of electrical resistivity is also believed to be due to the larger grain size at higher extrusion temperature. The transport properties and microstructure of the extruded samples will be measured and observed via Hall effect and EBSD measurements, respectively, to confirm the changes in the Seebeck coefficient and electrical resistivity.
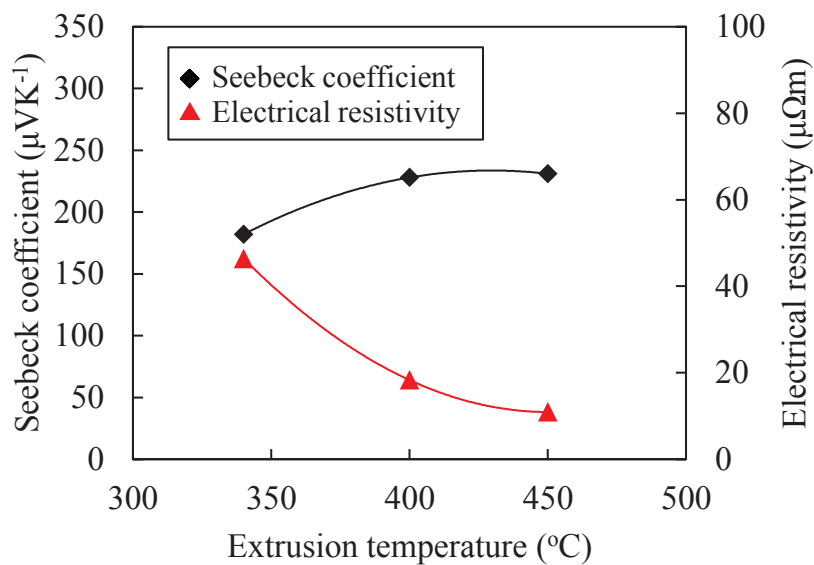
Fig. 7.20 Dependences of the Seebeck coefficient and electrical resistivity on extrusion temperature.

Fig. 7.21 shows the dependences of the thermal conductivity and figure of merit *ZT* on extrusion temperature. With increasing extrusion temperature, a slight increase of the thermal conductivity was found, which is also believed to be due to the grain growth. As a result, the resultant *ZT* value exhibited a linear increase in the extrusion temperature range of 340-400$^{o}$C. The highest *ZT* surprisedly reached to 1.5 for the sample extruded at 450$^{o}$C.
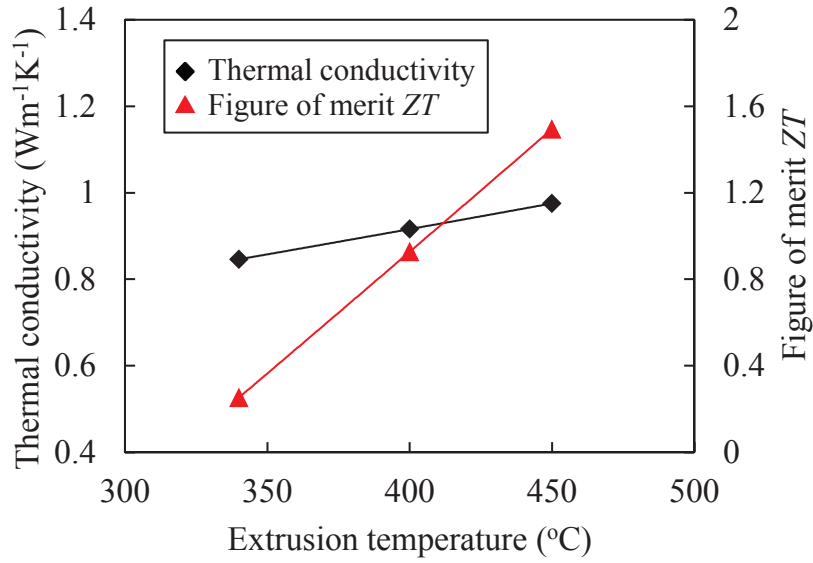
Fig. 7.21 Dependences of the thermal conductivity and figure of merit ZT on extrusion temperature.

### 7.3.7 Mechanical properties of hot-extruded samples

Fig. 7.22 shows the dependence of Vickers hardness on extrusion temperature. Although the hardness of the extruded samples shows a decreasing tendency as extrusion temperature increases, it is still much higher than that of zone-melted sample.
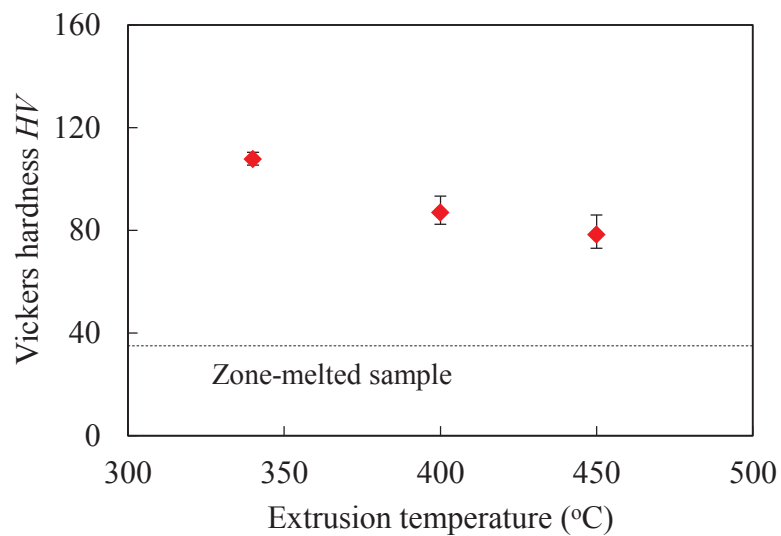


Fig. 7.22 Dependence of Vickers hardness on extrusion temperature.

## 7.4 Conclusions

This chapter was attempted to fabricate $Bi_2Te_3$-based bulk materials by using rapidly solidified powders. The feasibility of fabrication of high performance $Bi_2Te_3$-based bulk thermoelectric materials by RS and hot-extrusion technique has been investigated. Some conclusions are summarized as follows.

(1) All the SPSed samples showed high relative density and fine-grained microstructures.

(2) As sintering temperature increased, the change of carrier concentration was small, while the mobility increased, which resulted in a small variation of the Seebeck coefficient and a decrease in electrical resistivity.

(3) The thermal conductivi$ty$ remained almost unchanged until $400^o$C, followed by a rapid rise with sintering temperature. A $ZT$ value of 1.1 was achieved for the sample SPSed at $400^o$C. In addition, the samples had high hardness values.

(4) Dense $Bi_{0.4}Sb_{1.6}Te_3$ bulk thermoelectric materials were successfully fabricated by RS and hot-extrusion technique. The extruded sample showed preferred orientation of (0 0 0 1), and the basal planes were preferentially oriented parallel to the extrusion direction.

(5) With the increase in extrusion temperature, the Seebeck coefficient and thermal conductivity increased, while the electrical resistivity decreased significantly. As a result, a higher $ZT$ value of 1.5 was obtained for the sample extruded at $450^o$C. In addition, the extruded samples still keep a high level of Vickers hardness.

(6) Fabrication of high performance $Bi_2Te_3$-based bulk thermoelectric materials with oriented fine-grained microstructure by RS and hot-extrusion technique is feasible.

**References**

[1] P. Scherrer, Math-Phys Klasse 2 (1918) 98-100.

[2] T. S. Oh, D. B. Hyum, N.V. Kolomoets, Scripta Mater. 42 (2000) 849-854.

[3] D. M. Lee, C. H. Lim, D. C. Cho, Y. S. Lee, C. H. Lee, J. Electron. Mater. 35 (2006) 360-365.

[4] J. M. Schultz, J. P. Mchugh, W.A. Tiller, J. Appl. Phys. 33 (1962) 2443-2450.

[5] X. D. Liu, Y. H. Park, Mater. Trans. 43 (2003) 681-687.

[6] T. S. Kim, I. S. Kim, T. K. Kim, S. J. Hong, B. S. Chun, Mater. Sci. Eng., B 90 (2002) 42-46.

[7] Z. J. Xu, L. P. Hu, P. J. Ying, X. B. Zhao, T. J. Zhu, Acta Mater. 84 (2015) 385-392.

**Chapter 8 Summary**

Bi$_2$Te$_3$-based compounds have been widely used in various electronic cooling devices because of their good thermoelectric properties near room temperature. However, conventional fabrication techniques, such as unidirectional solidification and powder metallurgy, are difficult to simultaneously meet the needs of thermoelectric and mechanical properties. In the present work, from the viewpoints of grain refinement and preferred orientation, a mechanical alloying (MA) and hot-extrusion technique was proposed to fabricate Bi$_2$Te$_3$-based bulk materials, with emphasis on systematically investigating the effect of processing conditions on microstructure, texture, and thermoelectric and mechanical properties of the extruded materials. The main results obtained in the present research can be summarized as follows.

Chapter 1 described background of the present research. In order to face the impending energy shortage and environmental pollution issues, thermoelectric conversion attracts much attention in the recent decades. However, the achievements on the enhancement of heat-electricity conversion efficiency are not satisfied. Therefore, a combination of MA and hot-extrusion was proposed to fabricate Bi$_2$Te$_3$-based bulk materials to enhance the thermoelectric and mechanical properties simultaneously. The purpose of present research was to understand the relationships among processing conditions, microstructure, texture, thermoelectric and mechanical properties, thus to promote their industrial applications and contribute to improvement of energy shortage and environmental pollution issues. Information of thermoelectric effect, thermoelectric performance, current thermoelectric materials and fabrication methods were also described in Chapter 1.

In chapters 2 and 3, sound and dense $p$-type (Bi$_{0.2}$Sb$_{0.8}$)$_2$Te$_3$ and $n$-type Bi$_2$(Se$_{0.05}$Te$_{0.95}$)$_3$ bulk materials were successfully fabricated by MA and hot-extrusion technique in a temperature range of 340~450$^o$C. The combination of MA and hot extrusion resulted in significant grain refinement and preferential orientation. The (00 01) basal plane in the extrudates was preferentially oriented parallel to the extrusion direction. The electrical resistivity and thermal conductivity decreased with increasing

121

extrusion temperature due to grain growth. Small change of the Seebeck coefficient for $p$-type extruded samples measured at room temperature was found, while $n$-type extruded samples showed significant decrease as the extrusion temperature increased. As a result, a maximum value of $ZT = 1.2$ for $p$-type sample extruded at $400^{\circ}$C was obtained, while a lower $ZT_{max}$ value of 0.47 was found for $n$-type sample extruded at $400^{\circ}$C. In addition, all the extruded samples exhibited high hardness values.

A Te-rich phase was observed in the extruded samples, as described in Chapter 3. Therefore, Chapter 4 investigated the formation mechanism of the Te-rich phase and its effect on microstructure and thermoelectric properties. The formation and distribution of the Te-rich phase are mainly attributed to two different mechanisms: sublimation and eutectic reaction. The former occurs at any extrusion temperature and leads to formation of small-sized Te-rich phase, while the latter occurs at $\geq 400^{\circ}$C and the resultant Te-rich phase possesses large sizes. The small-sized Te-rich phase was distributed discretely around the grain boundaries in extruded samples. The distribution of the Te-rich phase in hot-extruded samples is also related to extrusion temperature. For example, at an extrusion temperature of $400^{\circ}$C, the large-sized Te-rich phase was distributed along the extrusion direction due to shear deformation during the extrusion. At $450^{\circ}$C, however, the Te-rich phase exhibited a massively agglomerated morphology because the eutectic reaction occurs during the cooling stage after the extrusion and, of course, no shear deformation exists. The incorporation of excessive amount of Te did not compensate the loss of Te content due to sublimation and/or eutectic reaction. On the contrary, much more Te-rich phase was formed, which resulted in decreases in grain size and orientation degree. Furthermore, the addition of excessive Te led to increase of carrier concentration and decrease of the mobility, which resulted in significant decrease of the Seebeck coefficient and slight increase of electrical resistivity. In addition, the addition of excessive Te caused an increase of thermal conductivity. As a result, a significant reduction in $ZT$ value was found.

In Chapter 5, in order to further improve the thermoelectric performance of $Bi_2Te_3$-based compounds, Cu was incorporated into $Bi_2Te_{2.85}Se_{0.15}$ compounds as a

dopant. The effect of Cu-doping on microstructure and thermoelectric properties of Bi-Te-Se bulk materials prepared via SPS or hot-extrusion technique was studied. Cu was distributed homogeneously in the matrix, and no severe segregation was observed. Fine-grained microstructures with a submicron order were observed in hot-extruded $Cu_xBi_2Te_{2.85}Se_{0.15}$ (x=0-0.05) samples, although there was a variation with increasing Cu contents. Significant Cu-doping effects were found in both the SPSed and hot-extruded samples. For example, at a lower sintering temperature of $300^oC$, the effect of Cu doping on thermoelectric properties was not evident. At $400^oC$, the carrier concentration was reduced significantly with increasing Cu content, and thus resulting in a significant increase in the absolute value of the Seebeck coefficient. However, the effect of Cu doping on electrical resistivity and thermal conductivity was not significant. An increase in $ZT$ was found with increasing Cu content. A largest $ZT$ value of 0.87 was achieved at room temperature for the $Cu_{0.05}Bi_2Te_{2.85}Se_{0.15}$ sample sintered at 400°C. As for the samples extruded at $400^oC$, a similar tendency of decrease in carrier concentration was found, which resulted in increases of the Seebeck coefficient and electrical resistivity, as well as decrease of thermal conductivity. The resultant $ZT_{max}$ of 0.86 was achieved at room temperature for the extruded $Cu_{0.05}Bi_2Te_{2.85}Se_{0.15}$ sample.

In Chapters 2 and 3, it was found that the thermoelectric properties of hot-extruded samples were sensitive to the lattice defects induced by mechanical-deformation during MA and hot-extrusion processes. Therefore, in order to reduce these lattice defects and thus to improve thermoelectric properties, in Chapter 6, heat treatment was carried out for extruded $(Bi_{0.2}Sb_{0.8})_2Te_3$ samples. The effect of annealing on microstructure, thermoelectric and mechanical properties was investigated. With the increase in annealing temperature, the sublimation of Te becomes significant, which leads to the formation of many large-sized pores and reduction of relative density. All the annealed samples exhibited fine-grained microstructures. The average grain size slightly increased for the samples extruded at $340^oC$ and annealed in the annealing temperature range of $260-400^oC$, while it was independent on annealing temperature at $\leq400^oC$.

The effect of annealing on thermoelectric properties was much more significant for the samples extruded at $340^{\circ}C$ than those extruded at $400^{\circ}C$. For example, the Seebeck coefficient increased significantly at lower annealing temperatures of $\leq 300^{\circ}C$, and the electrical resistivity decreased in the annealing temperature range of $260 \sim 380^{\circ}C$. As a result, evident improvement in $ZT$ value was obtained for the hot-extruded samples. Moreover, although the Vickers hardness exhibited a decreased tendency with increasing annealing temperature, the hardness values still showed a higher level than that of zone-melted sample.

In Chapter 7, from a viewpoint of mass production, rapid solidification (RS) such as gas atomization was tried to prepare $p$-type $(Bi_{0.2}Sb_{0.8})_2Te_3$ powder to replace MA, followed by consolidation using either spark plasma sintering (SPS) or hot-extrusion method. All the SPSed samples showed high relative density and fine-grained microstructures. Furthermore, the extruded samples exhibited preferred orientation, and the basal plane was preferentially oriented parallel to the extrusion direction. As sintering temperature increased, the change of carrier concentration was small, while the mobility increased, which resulted in a small variation of the Seebeck coefficient and a decrease in electrical resistivity. A $ZT$ value of 1.1 was achieved for the sample SPSed at $400^{\circ}C$. In addition, the samples had high hardness values, although there was a reduction with increasing sintering temperature due to grain growth. Subsequently, hot extrusion was conducted to try to fabricate $(Bi_{0.2}Sb_{0.8})_2Te_3$ bulk materials. The results indicated that all the extruded samples had sound appearances and high relative density. The basal planes were oriented parallel to the extrusion direction. Moreover, with the increase in extrusion temperature, the Seebeck coefficient and thermal conductivity increased, while the electrical resistivity decreased significantly. As a result, a higher $ZT$ value of 1.5 was obtained for the sample extruded at $450^{\circ}C$. In addition, the extruded samples still keep a high level of Vickers hardness. Therefore, the combination of RS and hot extrusion is feasible to fabricate high performance $Bi_2Te_3$-based thermoelectric materials in a large scale.

Base on the exploratory study in Chapter 7, in the future work, the $Bi_2Te_3$-based bulk thermoelectric materials will be fabricated by RS and hot-extrusion technique.

The understanding of the relationships among processing conditions, microstructure, texture, as well as thermoelectric and mechanical properties will help to promote industrial applications of $Bi_2Te_3$-based materials and thus contribute to improvement of energy shortage and environmental pollution issues.

# Achievements

Journal publications

1. <u>Zhi-Lei Wang</u>, Kenji Matsuoka, Takehiro Araki, Takahiro Akao, Tetsuhiko Onda, Zhong-Chun Chen, Extrusion behavior and thermoelectric properties of $Bi_2Te_{2.85}Se_{0.15}$ thermoelectric materials. *Procedia Engineering*, Vol. 81, pp. 616 - 621, 2014.

2. <u>Zhi-Lei Wang</u>, Takahiro Akao, Tetsuhiko Onda, Zhong-Chun Chen, Microstructure and thermoelectric properties of hot-extruded Bi-Te-Se bulk materials, *Journal of Alloys and Compounds*, Vol. 663, pp. 134 - 139, 2016.

3. <u>Zhi-Lei Wang</u>, Yuki Yokoyama, Takahiro Akao, Tetsuhiko Onda, Zhong-Chun Chen, Fabrication and thermoelectric properties of Cu-doped Bi-Te-Se bulk materials. *Journal of Japan Society of Powder and Powder Metallurgy*, Vol. 63, pp. 613-617, 2016.

4. <u>Zhi-Lei Wang</u>, Takahiro Akao, Tetsuhiko Onda, Zhong-Chun Chen, Formation of Te-rich phase and its effect on microstructure and thermoelectric properties of hot-extruded Bi-Te-Se bulk materials. *Journal of Alloys and Compounds*, Vol. 684, pp. 516-523, 2016.

International conferences

1. <u>Zhi-Lei Wang</u>, Takahiro Akao, Tetsuhiko Onda, Zhong-Chun Chen, Microstructure and thermoelectric properties of hot-extruded Bi-Te-Se bulk materials. *The 5$^{th}$ Joint Symposium on Materials and Mechanical Engineering between Northeastern University and Tottori University*, Shenyang, China, Sept. 2014.

2. <u>Zhi-Lei Wang</u>, Kenji Matsuoka, Takehiro Araki, Takahiro Akao, Tetsuhiko Onda, Zhong-Chun Chen, Extrusion behavior and thermoelectric properties of $Bi_2Te_{2.85}Se_{0.15}$ thermoelectric materials. *The 11$^{th}$ International Conference on Technology of Plasticity*, Nagoya, Japan, Oct. 2014.

3. <u>Zhi-Lei Wang</u>, Yuki Yokoyama, Takahiro Akao, Tetsuhiko Onda, Zhong-Chun

Chen, Fabrication and thermoelectric properties of Cu-doped Bi-Te-Se bulk materials. *The 3$^{rd}$ International Conference on Powder Metallurgy in Asia*, Kyoto, Japan, Nov. 2015.

4. <u>Zhi-Lei Wang</u>, Naoki Takeda, Yuki Yokoyama, Takahiro Akao, Tetsuhiko Onda, Zhong-Chun Chen, Microstructure and thermoelectric properties of high performance Bi-Te-Sb bulk materials fabricated from rapidly solidified powders. *The 35$^{th}$ International Conference and the 1$^{st}$ Asian Conference on Thermoelectrics*, Wuhan, P. R. China, May 2016.

5. <u>Zhi-Lei Wang</u>, Yuki Yokoyama, Kouya Miura, Takahiro Akao, Tetsuhiko Onda, Zhong-Chun Chen, Microstructure and thermoelectric properties of Bi-Te-Sb bulk materials fabricated from rapidly solidified powders. *The 6$^{th}$ Joint Symposium on Materials and Mechanical Engineering between Northeastern University and Tottori University*, Tottori, Japan, Sept. 2016.

Domestic conferences

1. <u>Zhi-Lei Wang</u>, Takahiro Akao, Tetsuhiko Onda, Zhong-Chun Chen, Fabrication of n-type $Bi_2Te_{2.85}Se_{0.15}$ bulk thermoelectric materials by mechanical alloying and hot-extrusion techniques. The 65$^{th}$ Japanese Joint Conference for the Technology of Plasticity, Oct. 2014.

2. <u>Zhi-Lei Wang</u>, Takahiro Akao, Tetsuhiko Onda, Zhong-Chun Chen, Effect of Te content on microstructure and thermoelectric properties of hot-extruded Bi-Te-Se bulk materials. The 114$^{th}$ Autumn Meeting for Powder and Powder Metallurgy, Oct. 2014.

3. Takehiro Araki, <u>Zhi-Lei Wang</u>, Takahiro Akao, Tetsuhiko Onda, Zhong-Chun Chen, Effect of annealing on thermoelectric properties of p-type $Bi_2Te_3$-based materials fabricated by hot extrusion. The 55$^{th}$ Chugoku Shikoku Branch Meeting of the Japan Institute of Metals and Materials, Aug. 2015.

4. Yuki Yokoyama, <u>Zhi-Lei Wang</u>, Takahiro Akao, Tetsuhiko Onda, Zhong-Chun Chen, Influence of Cu-doping on the thermoelectric properties of n-type $Bi_2Te_3$-based materials. The 55$^{th}$ Chugoku Shikoku Branch Meeting of the Japan

Institute of Metals and Materials, Aug. 2015.

5. <u>Zhi-Lei Wang</u>, Takahiro Akao, Tetsuhiko Onda, Zhong-Chun Chen, Effect of Te-rich phase on microstructure and thermoelectric properties of hot-extruded Bi-Te-Se bulk materials. The 157th Fall Annual Meeting of the Japan Institute of Metals and Materials, Sept. 2015.

6. <u>Zhi-Lei Wang</u>, Takahiro Akao, Tetsuhiko Onda, Zhong-Chun Chen, Formation of Te-rich phase and its effect on thermoelectric properties of hot-extruded Bi-Te-Se bulk materials. The 66th Japanese Joint Conference for the Technology of Plasticity, Oct. 2015.

7. Takehiro Araki, <u>Zhi-Lei Wang</u>, Takahiro Akao, Tetsuhiko Onda, Zhong-Chun Chen, Effect of annealing on the thermoelectric properties of hot-extruded $Bi_{0.4}Sb_{1.6}Te_3$ bulk materials. H27 Chugoku Shikoku Branch Meeting of the Japan Society for the Technology of Plasticity, Nov. 2015.

8. Takehiro Araki, <u>Zhi-Lei Wang</u>, Takahiro Akao, Tetsuhiko Onda, Zhong-Chun Chen, Effect of heat treatment on the thermoelectric properties of hot-extruded $Bi_{0.4}Sb_{1.6}Te_3$ bulk materials. The 158th Spring Annual Meeting of the Japan Institute of Metals and Materials, Mar. 2016.

# Acknowledgements